Efficient Repeat-Modelling of Time-Lapse Seismograms for Reservoir Monitoring

---

Effiziente Modellierung der Änderung von Seismogrammen bei der Überwachung von Erdöllagerstätten

Zur Erlangung des akademischen Grades eines

DOKTORS DER NATURWISSENSCHAFTEN

bei der Fakultät für Physik
der Universität Karlsruhe (TH)
genehmigte

DISSERTATION

von

Dipl.-Phys. Andreas Kirchner
aus Heilbronn

Tag der mündlichen Prüfung:	3. November 2000
Referent:	Prof. Dr. Peter Hubral
Korreferent	Prof. Dr. Serge Shapiro

30. November 2000

Zusammenfassung

Englische Fachbegriffe

Die vorliegende Dissertation ist mit Ausnahme dieser Zusammenfassung in englischer Sprache geschrieben. Da Veröffentlichungen in der angewandten Geophysik praktisch ausschließlich in Englisch verfasst werden, sind viele aus dem Englischen kommende Fachtermini auch in der deutschen Sprache gebräuchlich. Bei neueren Fachbegriffen – wie „time-lapse seismics“ – existiert oft kein angemessenes deutsches Äquivalent. In solchen Fällen wurde deshalb bewusst auf die Übersetzung verzichtet.

Einordnung in die Geophysik

Der Gegenstand der Geophysik ist die Erforschung der Struktur der Erde und ihrer physikalischen Prozesse. Der größte Teil unseres Planeten ist der direkten Beobachtung nicht zugänglich. Um Informationen über Bereiche zu erhalten, die sich unter der Erdoberfläche befinden, muss man deshalb meist auf indirekte Verfahren zurückgreifen.

Vor allem die Erforschung der Erde mit seismischen Wellen (der Gegenstand der Seismik) hat sich dabei als sehr erfolgreich erwiesen. Aufgrund ihrer geringen Dämpfung können Schallwellen in der Erde sehr weite Strecken zurücklegen und bieten – je nach Frequenzgehalt – eine gute Auflösung der Struktur des Untergrundes.

In der Seismik benutzt man künstliche Quellen zur Erzeugung elastischer Wellen in der Erde, und dichte Auslagen seismischer Empfänger registrieren die Ankunft der Wellen, die von Heterogenitäten im Untergrund reflektiert oder gestreut werden. Messdaten werden üblicherweise digitalisiert und mit dem Rechner weiterverarbeitet. Dabei verstärkt man die signifikante Information gegenüber dem Rauschen und erzeugt Abbilder des Untergrundes, die eine geologische Interpretation erlauben (siehe, z.B., Sheriff and Geldart, 1995; Yilmaz, 1987; Scales, 1994).

Durch ihren Einsatz zur Erkundung von Erdöl- und Erdgaslagerstätten sind seismische Methoden von erheblicher wirtschaftlicher Bedeutung. Die Erdöl produzierende Industrie nimmt täglich riesige Mengen seismischer Daten auf, einen großen Teil davon auf See.

„Time-lapse–Seismik“ – Seismische Überwachung der Erdölproduktion

Erdöl wird durch Bohrlöcher aus Reservoiren in porösen Gesteinsschichten gefördert. Zusätzliche Bohrungen liefern Erkenntnisse über die Geologie in der Umgebung einer Lagerstätte oder dienen zum Einpressen von Wasser, Dampf oder Chemikalien, die das Öl zur Produktionsbohrung treiben sollen. Weil die geologische Struktur der Lagerstätten in der Regel sehr heterogen ist, reichen die so gewonnenen Daten meist nicht aus, um die Verteilung der Permeabilität (und damit den Fluss des Erdöls) im Bereich zwischen den Bohrungen genau genug zu charakterisieren. Deshalb kommt es häufig vor, dass große Mengen von Erdöl nicht zur Produktionsbohrung gelangen.

Seismische Verfahren wurden ursprünglich nur zur *Erkundung* neuer Erdölvorkommen eingesetzt. Eher selten bei der darauf folgenden Erschließung und Ausbeutung. Die Genauigkeit und Reproduzierbarkeit seismischer Experimente ist inzwischen so hoch, dass sie den quantitativen Vergleich zweier Messungen erlaubt, die zu verschiedenen Zeitpunkten im gleichen Gebiet durchgeführt wurden. Diese neue Technologie nennt man “*Time-lapse–Seismik*”.

Die Industrie setzt derartige Untersuchungen immer häufiger über Erdölreservoiren ein, um in differenziellen Seismogrammen produktionsbedingte Änderungen sichtbar zu machen. Auf diese Weise kann man auf die räumliche Verteilung der Durchlässigkeit des Reservoirgesteins oder auf den Erfolg bzw. Misserfolg produktionsfördernder Maßnahmen schließen. Mögliche Schwierigkeiten können somit frühzeitig erkannt und gegebenenfalls notwendige Anpassungen vorgenommen werden. Dies gewinnt zunehmend an Bedeutung, weil ökonomische Zwänge eine immer intensivere Ausbeutung von Rohstoffvorkommen verlangen, die oft unter immer komplexeren geologischen Formationen liegen (Justice, 1991; Robertson, 1991).

In den vergangenen Jahren hat die Zahl der Veröffentlichungen über die erfolgreiche Anwendung von *Time-lapse*–Verfahren stetig zugenommen. Beispielsweise beschreiben Jenkins et al. (1997) ein Pilotprojekt zur seismischen Überwachung der Dampfinjektion in ein indonesisches Erdölfeld. Weitere interessante Fallstudien zu diesem Thema finden sich bei Greaves and Fulp (1991), Lumley (1995), Koster et al. (2000), Matthews (1991), Waite and Sigit (1997), Talley et al. (1998), Johnston et al. (1998, 2000), und Burkhart et al. (2000).

Ein *Time-lapse*–Projekt umfasst mindestens zwei seismische Messungen, die in verschiedenen Stadien der Erdölproduktion über einem Ölfeld durchgeführt werden. Große seismische Experimente sind sehr teuer, deshalb muss ihr Nutzen im Vorfeld möglichst genau geprüft werden. Lumley et al. (1997) und Wang (1997) stellen einige allgemeine Kriterien zur Beurteilung von *Time-lapse*–Projekten bereit. Wenn jedoch die geologische Struktur der Erdschichten oberhalb der Lagerstätte sehr komplex ist oder man nur kleine Änderungen der elastischen Parameter erwartet, dann ist oftmals eine detailierte Machbarkeitsstudie notwendig, die untersucht, ob die vermutete Änderung der Flüssigkeitsverteilung im vorgesehenen Experiment tatsächlich nachgewiesen werden kann (Hoffmann and Rekdal, 1999; Packwood, 1996; Al-Fares, 1995).

Bei solchen Machbarkeitsstudien spielt die numerische Simulation der seismischen Datenakquisition oft eine wesentliche Rolle (Biondi et al., 1998; Key et al., 1998; Lumley et al., 1994; Jenkins et al., 1997; Simm et al., 1997). Die so erhaltenen synthetischen Seismogramme geben die Änderung der elastischen Eigenschaften eines Modells der Lagerstätte wieder, welche ihrerseits mit petrophysikalischen Relationen aus einer Simulation der Flüssigkeitsverteilung im Reservoir berechnet werden. Überdies verwendet man synthetische Seismogramme, um die Konsistenz vorhandener Modelle einer Lagerstätte mit seismischen Messdaten zu überprüfen (Anderson et al., 1998) oder als Teil von Inversionsverfahren (z.B., Huang et al., 1998; Lo and Inderwiesen, 1994; Lazaratos and Marion, 1997).

Modellierung seismischer Experimente

Um eine hinreichende Genauigkeit der synthetischen Seismogramme sicherzustellen, erfordert die geologische Komplexität eines Erdölreservoirs und der darüber liegenden Erdschichten in vielen Fällen eine sehr genaue Modellierung des gesamten elastischen Wellenfeldes im Untergrund. Hierfür bietet sich besonders die Finite-Differenzen-Methode (*FD*) an, ein Standardverfahren, das die elastodynamische Wellengleichung (Gl. 2.9) durch eine Differenzengleichung annähert und eine Lösung für das Wellenfeld auf einem Gitter berechnet (siehe auch Kapitel 3 im Hauptteil, Virieux (1986) oder Kelly et al. (1976)).

Durch die geeignete Wahl des Gitterabstandes kann die Genauigkeit an die Anforderungen des Problems angepasst werden. Auch bei optimierten *FD*-Algorithmen erfordert die Simulation ganzer seismischer Experimente leider sehr viel Rechenzeit. Das gilt sowohl für zweidimensionale als auch für dreidimensionale Erdmodelle. Es wird daher intensiv nach zeitsparenden Alternativen gesucht, die eine vergleichbare Genauigkeit bieten (siehe z.B. Abschnitt 3.3 im Hauptteil, Lecomte (1996) oder Robertsson and Chapman (2000)).

Born Repeat-Modelling

Das Verfahren

In dieser Arbeit stelle ich das neue Modellierungsverfahren „*Born Repeat-Modelling*“ (BRM) vor, das ich speziell zur Lösung des oben geschilderten Problems entwickelt habe. Dabei verwende ich eine Kombination des *FD*-Verfahrens mit Elementen der Streutheorie, um die Änderung der Seismogramme zu berechnen, die durch produktionsbedingte Änderungen der elastischen Eigenschaften in einem Erdölreservoir verursacht wird (Kirchner and Shapiro, 1998, 1999, 2000). Die Wellenausbreitung in den Erdschichten oberhalb des Reservoirs wird mit der Genauigkeit des *FD*-Verfahrens berücksichtigt.

Die produktionsbedingten Änderungen in der Lagerstätte betrachte ich als kleine Störung des ursprünglichen Mediums und berechne die dadurch hervorgerufene Änderung der Seismogramme mit der Bornschen Näherung. Auf diese Weise wird ein großer Teil der sonst benötigten Rechenzeit eingespart. BRM erlaubt das Vorhandensein feiner geologischer Strukturen in allen Teilen des Erdmodells. Aufgrund des Störungsansatzes ist die Anwendbarkeit dieser Methode jedoch auf kleine Änderungen der elastischen Eigenschaften des Erdölreservoirs beschränkt.

Das *BRM*-Verfahren gliedert sich in die zwei nachfolgend beschriebenen Teile:

Stufe 1: Erzeugung des Datensatzes für die Green-Funktion. Für das Erdmodell, das die Verteilungen der Elastizitätsmoduln und der Dichte vor dem Beginn der Erdölproduktion beschreibt, wird zunächst mit dem Finite-Differenzen-Verfahren eine vollständige seismische Messung simuliert. Zusätzlich zu den Seismogrammen, die man mit seismischen Empfängern an der Erdoberfläche messen würde, wird das gesamte Wellenfeld auf einem Gitter innerhalb der Lagerstätte registriert. Dieses Gitter muss natürlich alle Orte umfassen, an denen sich die elastischen Parameter ändern. In der zweiten Stufe wird der so erhaltene Datensatz zur Berechnung der Seismogramme benötigt, denn diese Daten entsprechen der Green-Funktion für die verwendete Quellkonfiguration. Auf diese Weise berücksichtigt *BRM* die Streuung der elastischen Wellen in den Erdschichten oberhalb des Reservoirs mit der Genauigkeit des *FD*-Verfahrens.

Stufe 2: Modellierung (Berechnung der Seismogramme). Auf der Grundlage von Simulationen der Erdölförderung wird eine Folge von elastischen Modellen des Reservoirs erstellt, die jeweils die Verhältnisse zu einem bestimmten Zeitpunkt wiedergeben. Unter Verwendung des Ergebnisses der ersten Stufe wird in Bornscher Näherung die produktionsbedingte Änderung der gemessenen Seismogramme berechnet.

Das vorgeschlagene Verfahren wird in Kapitel 4 des Hauptteils dieser Arbeit ausführlich diskutiert. In Abbildung 4.1 auf Seite 40 ist der Algorithmus grafisch dargestellt.

Die Erzeugung des Green-Funktions-Datensatzes in Stufe 1 ist bei weitem der aufwendigste Teil von *BRM*. Dieser Rechenschritt muss jedoch nur einmal ausgeführt werden. Für jede weitere Konfiguration des Reservoirs wird nur die zweite Stufe (Modellierung) wiederholt.

Diese Vorgehensweise bringt den größten Nutzen, wenn Seismogramme für sehr viele verschiedene Konfigurationen des Reservoirs zu berechnen sind. Dann kann *BRM* im Vergleich mit bisher verwendeten Verfahren einen großen Teil der erforderlichen Rechenzeit einsparen. Auf diese Weise wird es möglich, mit vergleichbarer Genauigkeit größere *Time-lapse*–Experimente zu modellieren oder bei gleichbleibendem Aufwand eine größere Anzahl möglicher Reservoirmodelle zu testen. Die Ersparnis an Rechenzeit nimmt zu, wenn das Verhältnis der Anzahl der Gitterpunkte im Reservoir zur Gesamtzahl der Gitterpunkte im Erdmodell abnimmt. Deshalb werden für *BRM* in der Regel nur wenige Prozent der Rechenzeit einer reinen *FD*-Simulation benötigt. Ich erwarte, dass sich dieser Effekt in drei Dimensionen noch viel stärker auswirken wird als in 2-D.

Der theoretische Hintergrund

Die Erzeugung synthetischer *Time-lapse*–Seismogramme erfordert üblicherweise die numerische Lösung der elastodynamischen Wellengleichung für eine Folge von mindestens zwei vorgegebenen Modellen der Verteilung der elastischen Moduln λ und μ und der Dichte $\rho(\mathbf{r})$ im Untergrund. Die Fourier-Transformierte der Wellengleichung für ein isotropes Medium lautet (siehe auch Abschnitt 2.3 im Hauptteil):

$$\omega^2 \rho(\mathbf{r})\, u_i(\mathbf{r};\omega) + \left[\lambda(\mathbf{r})\, u_{k,k}(\mathbf{r};\omega)\right]_{,i} + \left[\mu(\mathbf{r})\left(u_{i,j}(\mathbf{r};\omega) + u_{j,i}(\mathbf{r};\omega)\right)\right]_{,j} + f_i(\mathbf{r};\omega) = 0\ . \tag{1}$$

Dabei ist $u_\mathrm{i}(\mathbf{r};\omega)$ die i-te Komponente der Auslenkung aus der Ruhelage. $\lambda(\mathbf{r})$ und $\mu(\mathbf{r})$ sind die Lamé-Parameter, mit denen man die Elastizität eines isotropen Materials charakterisiert (siehe Abschnitt 2.3.2 im Hauptteil). ω ist die Kreisfrequenz und $f_i(\mathbf{r};\omega)$ ist die i-te Komponente der Dichte einer äußeren Kraft. In drei Dimensionen nehmen die Indizes die Werte 1, 2 und 3 an, und die Werte 1 und 3 in 2-D. Über wiederholt auftretende Indizes wird summiert, und „$q_{,j}$“ steht für die partielle Ableitung von q nach der j-ten Koordinate eines kartesischen Koordinatensystems.

Nach einer gewissen Zeit der Erdölförderung haben sich die elastischen Eigenschaften des Reservoirs geändert. Dann gilt eine ähnliche Differentialgleichung mit modifizierten Koeffizienten:

$$\begin{aligned} \lambda^{\mathrm{P}}(\mathbf{r}) &= \lambda(\mathbf{r}) + \delta\lambda(\mathbf{r}) \\ \mu^{\mathrm{P}}(\mathbf{r}) &= \mu(\mathbf{r}) + \delta\mu(\mathbf{r}) \\ \rho^{\mathrm{P}}(\mathbf{r}) &= \rho(\mathbf{r}) + \delta\rho(\mathbf{r}) \ . \end{aligned} \tag{2}$$

Die Lösung für das gestörte Erdmodell kann man in Form einer Integralgleichung darstellen. Vernachlässigt man die Mehrfach-Streueffekte, die durch $\delta\lambda$, $\delta\mu$ und $\delta\rho$ hervorgerufen werden (Bornsche Näherung), so ergibt sich ein Ausdruck für das gesuchte Wellenfeld (z.B. Gubernatis et al., 1977a):

$$\begin{aligned} u_i^{\mathrm{P}}(\mathbf{r};\omega) \approx\ & u_i(\mathbf{r};\omega) + \int_{\mathrm{res}} d^3r'\, G_{mi,m}\left(\mathbf{r}',\mathbf{r};\omega\right)\, \delta\lambda\left(\mathbf{r}'\right) u_{k,k}\left(\mathbf{r}';\omega\right) \\ & + \int_{\mathrm{res}} d^3r'\, G_{mi,j}\left(\mathbf{r}',\mathbf{r};\omega\right)\, \delta\mu\left(\mathbf{r}'\right) \left[u_{m,j}\left(\mathbf{r}';\omega\right) + u_{j,m}\left(\mathbf{r}';\omega\right)\right] \\ & + \omega^2 \int_{\mathrm{res}} d^3r'\, G_{mi}\left(\mathbf{r}',\mathbf{r};\omega\right)\, \delta\rho\left(\mathbf{r}'\right) u_m\left(\mathbf{r}';\omega\right) \ , \end{aligned} \tag{3}$$

In Gleichung 3 kommt die Green-Funktion $G_{im}\left(\mathbf{r},\mathbf{r}';\omega\right)$ vor, die als Lösung von Gleichung 1 für eine Punktquelle $f_{im}(\mathbf{r};\omega) = f(\omega)\delta(\mathbf{r}-\mathbf{r}')\delta_{im}$ am Ort $\mathbf{r}'$ definiert ist. Die Integrationsbereiche müssen mindestens alle Punkte $\mathbf{r}'$ enthalten, an denen sich die relevanten Eigenschaften der Lagerstätte ändern.

Dies ist die zentrale Gleichung von *BRM* für isotrope Medien. Wenn das Wellenfeld innerhalb des Reservoirs aus vorhergegangenen *FD*-Simulationen bekannt ist, kann man mit Gleichung 3 zu einer gegebenen Störung der elastischen Eigenschaften der Lagerstätte schnell die Änderung $\boldsymbol{\delta}\mathbf{u} = \mathbf{u}^{\mathrm{P}} - \mathbf{u}$ der Seismogramme berechnen.

Im Zusammenhang mit der seismischen Überwachung der Erdölproduktion ergibt sich folgende Interpretation: Die gesamte Auslenkung $u_i^{\mathrm{P}}(\mathbf{r};\omega)$ am Ort $\mathbf{r}$ des Empfängers setzt sich zusammen aus dem Wellenfeld, das von der ursprünglichen Form des Reservoirs und von den dazwischen liegenden Erdschichten zurückgestreut wurde, und aus dem Beitrag der neu hinzugekommenen Heterogenitäten. Unter den Integralen ist $u_i^{\mathrm{P}}(\mathbf{r};\omega)$ das Feld der auf das Reservoir einfallenden Welle. Am Ort $\mathbf{r}'$ erzeugen die produktionsbedingten Störungen $\delta\lambda\left(\mathbf{r}'\right)$, $\delta\mu\left(\mathbf{r}'\right)$ und $\delta\rho\left(\mathbf{r}'\right)$ das zusätzlich gestreute Feld, welches mit der Green-Funktion $G_{im}\left(\mathbf{r},\mathbf{r}';\omega\right)$ zum Empfänger am Ort $\mathbf{r}$ übertragen wird. Wechselwirkungen höherer Ordnung des Wellenfeldes mit der Änderung des Reservoirs werden vernachlässigt. Multiple Reflexionen des ungestörten Reservoirs und der oberhalb liegenden Schichten sind jedoch vollständig enthalten.

Die Struktur von Gleichung 3 ist die Ursache der Zeitersparnis durch *BRM* im Vergleich mit einer reinen *FD*-Modellierung: Da beide Verfahren beliebig heterogene Medien unterstützen, benutzen sie eine diskrete Darstellung des Wellenfeldes

auf einem Gitter. Bei einer *FD*-Simulation erfordert der Übergang von einer Zeit t nach $t + \Delta t$ jeweils Rechenoperationen für jeden einzelnen Gitterpunkt (siehe Abschnitt 3.2.4 im Hauptteil). Die Integrationsbereiche in Gleichung 3 beschränken sich auf einen kleinen Teil des Gitters. Demzufolge muss die Ersparnis linear mit dem Verhältnis der Gitterpunkte, die von beiden Verfahren verwendet werden, anwachsen.

Die Gleichungen dieses Abschnittes habe ich für dreidimensionale Medien geschrieben. Bei entsprechender Anpassung der Integrationsbereiche und der Einschränkung der Indizes auf die Werte 1 und 3 gelten sie ebenso für zweidimensionale Medien.

Erzeugung der Green-Funktion

Seismische Quellen werden in der Regel als Punktquellen mit einem frequenzabhängigen Quellsignal beschrieben. Insbesondere, wenn sich die Quelle und ein Empfänger am selben Ort befinden (Zero-offset–Konfiguration) ist die Green-Funktion $G_{im}\left(\mathbf{r}, \mathbf{r}'; \omega\right)$ dem Feld $\mathbf{u}\left(\mathbf{r}; \omega\right)$ der einfallenden Welle sehr ähnlich. Dann gilt:

$$G_{im}\left(\mathbf{r}, \mathbf{r}'; \omega\right) \cdot f\left(\omega\right) = u_i\left(\mathbf{r}; \omega\right) \ . \tag{4}$$

Hierbei ist $\mathbf{r}$ ein Punkt innerhalb des Reservoirs, und der Index m beschreibt die Ausrichtung der Quelle. Aufgrund des Reziprozitätstheorems (Gl. 2.24 auf Seite 17) kann man bei der Green-Funktion die Koordinaten von Quelle und Empfänger vertauschen:

$$G_{im}(\mathbf{r}', \mathbf{r}) = G_{mi}(\mathbf{r}, \mathbf{r}') \tag{5}$$

Auf diese Weise berechnet man den benötigten Teil der Green-Funktion sehr einfach mit einer *FD*-Simulation und anschließender Dekonvolution des Wellenfeldes mit dem bekannten Quellsignal $f\left(\omega\right)$.

Die Green-Funktion für endliche Abstände zwischen Quelle und Empfänger ergibt sich aus einer *FD*-Simulation mit einer Punktquelle am Ort des Empfängers. Bei der Simulation umfangreicher seismischer Messungen empfiehlt es sich, durch die mehrfache Verwendung von Green-Funktionen für Quellen und Empfänger den Gesamtaufwand zu optimieren.

Anwendung von Born Repeat-Modelling

Die Leistungsfähigkeit von BRM untersuche ich in mehreren Studien, die jeweils einen bestimmten Aspekt der Modellierung bzw. des zugrunde liegenden Erdmodells genauer beleuchten.

Simulation seismischer Experimente an Land

Für ein ansonsten homogenes Erdmodell habe ich untersucht wie sich die Änderung der elastischen Eigenschaften eines rechteckigen Einschlusses auf die Seismogramme auswirkt, die an der Erdoberfläche gemessen werden. Die Änderung solcher Seismogramme wurde jeweils mit *BRM* und mit reinen Finite-Differenzen-Modellierungen für alle möglichen Typen isotroper Änderungen der elastischen Moduln und der Dichte des Einschlusses berechnet. Durch Vergleich der auf diese Weise erhaltenen Ergebnisse konnte die prinzipielle Anwendbarkeit des vorgeschlagenen Ansatzes – also die Verknüpfung der Störungstheorie mit dem Finite-Differenzen-Verfahren – nachgewiesen werden (siehe Abschnitt 4.4 im Hauptteil). Generell sollte die Güte der erhaltenen Resultate mit zunehmender Änderung der Eigenschaften des Reservoirs abnehmen. Diese Eigenschaft der Bornschen Näherung wurde in den numerischen Tests untersucht und bestätigt.

Test von BRM für ein sehr komplexes Erdmodell

Die Struktur der oberen Erdkruste kann sehr heterogen sein, was besondere Anforderungen an die Genauigkeit der Modellierungsverfahren stellt. Grundsätzlich gibt es aus theoretischer Sicht für *BRM* keine Einschränkungen bezüglich der Komplexität des verwendeten Erdmodells. In den Erdschichten oberhalb der Lagerstätte berücksichtigt *BRM* alle Einzelheiten mit der Genauigkeit des *FD*-Verfahrens. Dies habe ich am Beispiel des Marmousi-Modells überprüft, das in Abbildung 4.9 auf Seite 55 zu sehen ist. Die Art der Änderung des Reservoirs habe ich so gewählt wie sie beispielsweise bei der Ersetzung des vorhandenen Erdöls durch Wasser auftreten könnte. Einzelheiten hierzu sind in Abschnitt 4.6.1 im Hauptteil zu finden.

Für verschiedene Positionen der seismischen Quelle und für verschiedene Abstände der seismischen Empfänger von der Quelle wurden synthetische Seismogramme berechnet (siehe Abbildungen 4.11 auf Seite 57 und Abbildung 4.12 auf Seite 58). Das Reservoir des Marmousi-Modells liegt unterhalb einer sehr komplexen geologischen Formation mit mehreren Verwerfungen. Bedingt durch die Komplexität dieses Modells variiert die maximale Amplitude der simulierten Änderung der Seismogramme um zwei Größenordnungen mit dem Ort der seismischen Quelle bzw. des seismischen Empfängers. Mit derartigen Informationen lassen sich seismische Messungen so optimieren, dass die beobachteten Änderungen möglichst groß werden.

Die Modellierungsergebnisse von *BRM* werden mit den Resultaten reiner *FD*-Simulationen verglichen. Die jeweils erhaltenen Seismogramme sind einander sehr ähnlich. Generell reproduziert *BRM* die Laufzeiten der seismischen Wellen sehr genau. Bei den Wellenformen und den Amplituden beobachte ich geringe Ab-

weichungen, die mit ansteigender Frequenz zunehmen. Dies stimmt mit theoretischen Überlegungen zu Gültigkeit der Bornschen Näherung (Hudson and Heritage, 1981) überein.

Ein Vergleich der von beiden Verfahren benötigten Rechenzeiten ergab eine Ersparnis von mehr als 99% bei Verwendung von *BRM*. Im Fall von *BRM* wirkt sich das Einlesen der Green-Funktion spürbar auf die insgesamt benötigte Zeit aus.

Modellierung mariner Experimente

Theorie

Die Industrie führt einen großen Teil ihrer seismischen Messungen auf See durch. Da sich die seismischen Empfänger dabei im Wasser befinden, misst man hier den Druck. Es wäre sehr ineffizient, zunächst mit *BRM* an mehreren benachbarten Punkten die Auslenkung zu berechnen und diese anschließend zu differenzieren, um den Druck zu erhalten. Ich führe deshalb die Funktion $g_m(\mathbf{r},\mathbf{r}';\omega)$ ein, die mit der Green-Funktion $G_{nm}(\mathbf{r},\mathbf{r}';\omega)$ folgendermaßen zusammenhängt:

$$g_m(\mathbf{r},\mathbf{r}';\omega) \quad = \quad -\lambda(\mathbf{r})\,\frac{\partial G_{nm}(\mathbf{r},\mathbf{r}';\omega)}{\partial r_n}\,. \tag{6}$$

Die Funktion $g_m(\mathbf{r},\mathbf{r}';\omega)$ ist die Lösung der folgenden partiellen Differentialgleichung:

$$\left[\delta_{ik}\,\omega^2\rho(\mathbf{r}) + \frac{\partial}{\partial r_j}\,c_{ijkl}(\mathbf{r})\frac{\partial}{\partial r_l}\right]\,g_k(\mathbf{r},\mathbf{r}';\omega) \quad = \quad \lambda(\mathbf{r}')\frac{\partial}{\partial r_i}\delta(\mathbf{r}-\mathbf{r}')\,. \tag{7}$$

Mittels *FD*-Simulationen sind die Werte der Komponenten von $g_m(\mathbf{r},\mathbf{r}';\omega)$ an allen Punkten $\mathbf{r}'$ eines Gitters innerhalb des Reservoirs zu berechnen und anstelle der Green-Funktion $G_{nm}(\mathbf{r},\mathbf{r}';\omega)$ an die zweite Stufe von *BRM* zu übergeben.

Auf diese Weise können mit *BRM* auch Druck-Seismogramme effizient modelliert werden. Beide Formen von *BRM* nutzen dieselbe Implementation der zweiten Stufe von *BRM* (siehe Seite iv). Der Rechenaufwand zur Modellierung von Druck-Seismogrammen mit *BRM* ist demnach nahezu gleich groß wie der zur Erzeugung von Seismogrammen der Auslenkung $\mathbf{u}$, denn die jeweils durchzuführenden Rechenschritte sind für beide Fälle sehr ähnlich.

Beispiel für die Berechnung von Druck-Seismogrammen

Zur Erzeugung von Druck-Seismogrammen habe ich ein einfaches, geschichtetes Erdmodell erstellt, dessen oberste Schicht die elastischen Eigenschaften von Was-

ser hat. Entsprechend meiner Vorgehensweise im Abschnitt „Simulation seismischer Experimente an Land“ habe ich auch hier alle möglichen Typen von Änderungen des Reservoirs getestet. Druck-Seismogramme wurden für je zwei Positionen an der Oberseite des Modells berechnet.

Meine Ergebnisse sind in den Abbildungen 5.2 - 5.4 auf Seite 66ff dargestellt. Zum Vergleich habe ich die entsprechenden Resultate des *FD*-Verfahrens in dieselben Schaubilder eingezeichnet. In allen Fällen stimmen Laufzeiten, Wellenformen und Amplituden einander entsprechender Registrierungen sehr genau überein.

In der Praxis weist man Änderungen in einer Lagerstätte oft indirekt nach. Dazu untersucht man Laufzeitverschiebungen von Wellen, die an Schichtgrenzen unterhalb des Reservoirs reflektiert werden und auf ihrem Weg dorthin das Reservoir durchlaufen. Hierbei wird die einfallende Welle am Reservoir unter einem kleinen Winkel gestreut. Aufgrund der Schwäche der Bornschen Näherung bei Vorwärtsstreuung (Gubernatis et al., 1977b), ist diese Situation besonders kritisch für *BRM*. In den oben beschriebenen Seismogrammen sind solche Reflexionsereignisse enthalten. Auch in diesen Fällen stimmen die Resultate von *BRM* sehr genau mit denen des *FD*-Verfahrens überein.

BRM für anisotrope Änderungen von Erdölreservoiren

Anisotropie von Reservoirgesteinen

Wenn wir mittels seismischer Wellen den Aufbau der Erde erforschen, beschreiben wir diese meist als isotropes Medium. In der Natur kommen jedoch sehr viele Stoffe vor, bei denen die Geschwindigkeit einer Welle von deren Ausbreitungsrichtung abhängt. Der Begriff „anisotrop“ beschreibt hierbei Materialien, die auf einer Längenskala unterhalb der seismischen Wellenlänge eine heterogene Struktur aufweisen. Bei anisotropen Mineralien ist dies die atomare Längenskala. Eine seismische Welle kann die Einzelheiten eines solchen Mediums nicht auflösen und verhält sich deshalb wie in einem homogenen Medium mit bestimmten effektiven Eigenschaften. Die Symmetrie des inhomogenen Materials überträgt sich auf das effektive Medium. Ist die Verteilung dieser kleinskaligen Heterogenitäten richtungsabhängig, dann kann das effektive Medium anisotrop sein.

Auf der seismischen Längenskala beobachtet man in der Natur drei Symmetrieklassen: Dies sind die transversale Isotropie (hier gleichbedeutend mit hexagonaler Symmetrie), orthorhombische Symmetrie und monokline Symmetrie. Die einfachste und am häufigsten auftretende Art ist die transversale Isotropie. Sie wird durch dünn geschichtete Medien erzeugt, wie beispielsweise durch dünne Gesteinsschichten oder eine groß Zahl parallel ausgerichteter Risse. Transversal isotrope Medien besitzen eine Symmetrieachse, die senkrecht auf den Schichten

steht. Je nach der Ausrichtung dieser Achse unterscheidet man zwischen vertikaler transversaler Symmetrie (vertikale Symmetrieachse) und horizontaler transversaler Symmetrie (horizontal ausgerichtete Symmetrieachse). Dies Formen der Anisotropie sind in Abbildung 6.1 im Hauptteil veranschaulicht. Die orthorhombische Symmetrie ergibt sich durch die Superposition von horizontaler und vertikaler transversaler Isotropie. Monokline Symmetrie entsteht durch das Einbringen geneigter Risse in ein dünn geschichtetes Material (Ebrom and Sheriff, 1991; Schoenberg and Muir, 1989).

Die Größe und Anordnung von Rissen im Gestein bestimmt den Fluss des Erdöls in vielen Reservoiren. Mit geeigneten Auswerteverfahren kann man aus seismischen Messdaten Informationen über die Anisotropie, und damit über die Dichte und Anzahl der Risse gewinnen. In (dreidimensionalen) anisotropen Medien gibt es im Allgemeinen zwei unabhängige Scherwellen, die sich mit verschiedenen Geschwindigkeiten ausbreiten (Doppelbrechung). Der Grad der Doppelbrechung und die Polarisation der beiden Moden geben Aufschluss über die Dichte und die Ausrichtung der Risse. Deshalb ist die Simulation der Wellenausbreitung in anisotropen Medien sehr wichtig für die Planung seismischer Messungen.

Produktionsbedingte Änderungen der Anisotropie

Mit den Methoden der Time-lapse–Seismik kann man produktionsbedingte *Änderungen* der inneren Symmetrie des Gesteins in Lagerstätten untersuchen (Winterstein et al., 1998). Als mögliche Ursache solche Effekte kommt zum Beispiel das Einpressen von Flüssigkeiten durch ein Bohrloch unter hohem Druck in Frage. Dadurch erzeugt man neue oder erweitert bereits vorhandene Risse, um so die Durchlässigkeit des Gesteins in der Nähe des Bohrloches zu erhöhen (Meadows and Winterstein, 1994; Groenenboom and van Dam, 2000).

Auch die (produktionsbedingte) Änderung der Druckverhältnisse in einem Reservoir kann eine Änderung der Anisotropie zur Folge haben, die sich mit Time-lapse–Verfahren nachweisen lässt. Das Öffnen und Schließen von Rissen aufgrund einer Änderung des effektiven Spannungszustands des Reservoirgesteins beeinflusst die effektiven elastischen Moduln. Dabei sind diejenigen Risse am stärksten betroffen, deren Rissfläche senkrecht auf der von außen einwirkenden Spannung steht. Je nach der Verteilung der Risse im spannungsfreien Zustand und der Symmetrie der äußeren Spannung können sich verschiedene Typen von elastischer Anisotropie ergeben (Nur, 1971).

Theoretische Grundlage von BRM für anisotrope Änderungen

Mit Born Repeat-Modelling (*BRM*) kann man die Änderung von Seismogrammen berechnen, die sich durch anisotrope Änderungen der elastischen Eigenschaften

einer Lagerstätte ergeben. Die allgemeinste Form von Gleichung 3 berücksichtigt anstelle der Lamé Parameter eine allgemeine, anisotrope Änderung δc_{mjkl} des Elastizitätstensors:

$$\begin{aligned} u_i^{\mathrm{P}}(\mathbf{r};\omega) \;\approx\; & u_i(\mathbf{r};\omega) + \omega^2 \int_{\mathrm{res}} dV'\, G_{mi}\left(\mathbf{r}',\mathbf{r};\omega\right)\, \delta\rho\left(\mathbf{r}'\right) u_m\left(\mathbf{r}';\omega\right) \\ & + \int_{\mathrm{res}} dV'\, G_{mi,j}\left(\mathbf{r}',\mathbf{r};\omega\right)\, \delta c_{mjkl}\left(\mathbf{r}'\right) u_{k,l}\left(\mathbf{r}';\omega\right) \;. \end{aligned} \tag{8}$$

Mit dieser Formel kann man die Änderung der Seismogramme für beliebige, anisotrope Änderungen der elastischen Moduln in einer Lagerstätte berechnen.

Numerische Analyse der Auswirkungen anisotroper Änderungen

Transversal isotrope Medien sind in zwei Dimensionen durch die vier elastischen Moduln c_{11}, c_{13}, c_{33} und c_{55} vollständig charakterisiert. Für diesen Fall habe ich eine ausführliche Untersuchung der Leistungsfähigkeit von *BRM* durchgeführt (siehe Abschnitt 6.3).

In einem ersten Schritt habe ich mit dem verallgemeinerten Verfahren die Auswirkung einer isotropen Änderung von c_{33} berechnet, um die Konsistenz mit der isotropen Modellierung zu überprüfen. Eine isotrope Perturbation erhält man für

$$\delta c_{11} \;=\; \delta c_{13} \;=\; \delta c_{33} \tag{9}$$

und

$$\delta c_{55} \;=\; 0\;. \tag{10}$$

Die Laufzeiten, Wellenformen und Amplituden der so berechneten Seismogramme stimmen bis auf wenige Einsätze gut mit den Ergebnissen des *FD*-Verfahrens überein. Es werden einige Einsätze gestreuter Scherwellen vorhergesagt, die im isotropen Fall nicht auftreten können. Die Amplituden dieser abweichenden Ereignisse sind jedoch gering. Die Unterschiede zwischen den isotropen und anisotropen Formen von *BRM* ergeben sich durch die Art und Weise wie die einzelnen Beiträge berechnet werden: Aufgrund der Allgemeinheit des anisotropen Falls müssen die Beiträge von c_{11}, c_{13} und c_{33} getrennt berechnet und anschließend addiert werden. Bei der isotropen Form von *BRM* ist dies umgekehrt. Dadurch werden numerische Ungenauigkeiten vermieden, die bei der Subtraktion gleich großer Zahlen zwangsläufig entstehen.

Für Änderungen der verschiedenen elastischen Moduln eines vertikal transversal isotropen Mediums wurden getrennte Untersuchungen durchgeführt. Im Vergleich mit entsprechenden Ergebnissen des *FD*-Verfahrens ergab sich immer eine gute Übereinstimmung der Wellenformen und Laufzeiten. Änderungen von c_{13}

und c_{33} liefern auch sehr gute Ergebnisse für die Amplituden der berechneten Seismogramme. c_{13} und c_{33} spielen ein sehr wichtige Rolle für die Reflexionsseismik, denn sie bestimmen die Geschwindigkeit der Druckwelle für nahezu vertikale Ausbreitungsrichtung. Im Fall von c_{11}, und in geringerem Maß für c_{55}, beobachte ich allerdings Abweichungen der Amplituden, was das Verhalten von *BRM* im Fall einer isotropen Störung erklärt.

Mit dieser Untersuchung wurde gezeigt, dass *BRM* auch für anisotrope Medien verallgemeinert werden kann. Obwohl die anisotrope Form von *BRM* auf numerische Ungenauigkeiten etwas empfindlicher reagiert, erhalte ich in den meisten Fällen sehr gute Ergebnisse. Ein detaillierter Vergleich der benötigten Rechenzeiten ergab eine Ersparnis von mehr als 99% für *BRM* im Vergleich mit einer Finite-Differenzen–Modellierung.

Schlussbemerkung

Zur effizienten Planung seismischer Time-lapse–Experimente müssen oft vollständige seismische Messungen für mehrere mögliche Reservoirkonfigurationen simuliert werden.

Das hier vorgestellte Verfahren „Born Repeat-Modelling“ (*BRM*) verknüpft die sehr genaue Finite-Differenzen-Methode mit einem störungstheoretischen Ansatz für das Reservoir. Auf diese Weise werden Änderungen von Seismogrammen berechnet, die durch produktionsbedingte Änderungen der elastischen Eigenschaften einer Erdöl- oder Erdgaslagerstätte hervorgerufen werden. Die Anwendbarkeit dieser Kombination wurde numerisch für alle möglichen Typen von Perturbationen der elastischen Eigenschaften des Reservoirs und für ein Erdmodell mit sehr komplexer geologischer Struktur überprüft.

Ich beschreibe eine Möglichkeit zur effizienten Erweiterung von *BRM* auf die Modellierung von Druck-Seismogramme. Dies wird zur Simulation mariner seismischer Experimente beötigt. Überdies wurde *BRM* für anisotrope Änderungen der Eigenschaften der Lagerstätte verallgemeinert. Diese beiden Fälle habe ich ebenfalls an Beispielen eingehend untersucht. Insbesondere wurden als Test von *BRM* die Auswirkungen verschiedener transversal isotroper Modifikationen einer Lagerstätte im Seismogramm mit großer Genauigkeit modelliert. Dabei war die Dicke des modifizierten Bereiches in der Größenordnung der dominanten seismischen Wellenlänge. Meines Wissens existiert eine derartige Studie in der Literatur bisher noch nicht.

In allen numerischen Untersuchungen wurden die Ergebnisse von *BRM* mit Resultaten reiner Finite-Differenzen–Modellierungen verglichen. Dabei ergab sich, dass die Genauigkeit von *BRM* für hinreichend kleine Änderungen der Eigenschaften

der Lagerstätte der Genauigkeit des Finite-Differenzen-Verfahrens nahe kommt. Da *BRM* gezielt die Redundanzen dieses Standardverfahrens beseitigt, konnte in allen untersuchten Fällen ein großer Teil der Rechenzeit – oft mehr als 99% – eingespart werden.

Die Anregung, sich mit dem Problem der Modellierung von Time-lapse–Seismogrammen zu befassen, kommt ursprünglich von einem Unternehmen, das die Erforschung von *BRM* über einen längeren Zeitraum gefördert hat. Da *BRM* in vielen Fällen die gestellten Anforderungen bezüglich Schnelligkeit und Genauigkeit erfüllen kann und der Bedarf zur effizienten Modellierung von Time-lapse–Experimenten in Zukunft vermutlich eher zunehmen wird, halte ich den Einsatz von *BRM* in der Industrie für denkbar.

Contents

Zusammenfassung **i**

Abstract **xix**

1 Introduction **1**
1.1 Seismic reservoir monitoring 1
1.2 Modelling time-lapse seismograms 2
1.3 Overview of this thesis 3
1.4 Basic concepts of exploration seismics 4
1.4.1 The reflection seismic experiment 4
1.4.2 Time-lapse seismics 6

2 Fundamentals of elastic wave propagation **9**
2.1 Introductory remarks 9
2.2 Description of elastic bodies 9
2.2.1 The elastic continuum 9
2.2.2 Stress and strain 10
2.2.3 Linear elasticity and the stiffness tensor 11
2.2.4 Symmetry properties and abbreviated notation 11
2.3 Theory of wave propagation 12
2.3.1 The elastodynamic wave equation 12
2.3.2 Elastic parameters for isotropic media 12
2.3.3 P-waves and S-waves 13
2.3.4 Wave propagation in fluids 14
2.3.5 Elastic properties of fluid-saturated porous solids 14
2.4 Green's function and related theorems 15
2.4.1 Green's function 15
2.4.2 The representation theorem 16
2.4.3 Reciprocity 17
2.5 Scattering at small heterogeneities 17
2.5.1 Waves in inhomogeneous media 17
2.5.2 The perturbation method 18
2.6 Discrete representation of continuous functions 21

3 Modelling time-lapse seismograms **23**
3.1 Introduction . . . 23
3.1.1 Numerical seismic modelling . . . 23
3.1.2 Modelling reservoir changes . . . 24
3.2 Finite-Difference modelling . . . 25
3.2.1 Importance of the finite-difference method . . . 25
3.2.2 Example of FD seismograms . . . 26
3.2.3 Discretisation of derivatives . . . 26
3.2.4 The time update . . . 31
3.2.5 Restrictions of finite-difference modelling . . . 32
3.3 Optimised approaches to time-lapse modelling . . . 33
3.3.1 Special features of time-lapse models . . . 33
3.3.2 The hybrid modelling technique by Lecomte et al. . . . 34
3.3.3 FD-injection . . . 35
3.3.4 Discussion . . . 37

4 Born Repeat-Modelling **39**
4.1 The BRM algorithm . . . 39
4.2 Theoretical background . . . 41
4.2.1 Records of displacement or particle velocity . . . 41
4.2.2 Generation of Green's functions . . . 43
4.3 Applicability of BRM . . . 44
4.3.1 Estimate of computational efficiency . . . 44
4.3.2 Validity . . . 45
4.4 Application to a model with homogeneous overburden . . . 46
4.4.1 Description of the model . . . 46
4.4.2 Modelling results . . . 46
4.4.3 Behaviour for large perturbations . . . 49
4.5 3-D modelling with BRM . . . 51
4.5.1 Importance of 3-D modelling . . . 51
4.5.2 Example . . . 51
4.5.3 Computational aspects . . . 54
4.6 Test of BRM with an extremely complex overburden . . . 54
4.6.1 Numerical setup for the Marmousi model. . . . 54
4.6.2 Modelling results and discussion . . . 56
4.6.3 Computing time . . . 60

5 Modelling marine surveys **61**
5.1 Importance of pressure seismograms . . . 61
5.2 Derivation of the pressure modelling equation . . . 62
5.3 Example: Model with a water layer . . . 64
5.3.1 Description of the model . . . 64
5.3.2 Modelling results . . . 65
5.3.3 Discussion . . . 67

6 Reservoir anisotropy **71**
6.1 Introduction 71
6.1.1 Elastic waves in anisotropic media 71
6.1.2 Fine structure of reservoirs 72
6.1.3 Production-related changes of reservoir anisotropy 72
6.1.4 BRM for anisotropic media 73
6.2 Stiffness and velocities in anisotropic media 74
6.2.1 Structure of the stiffness tensor 74
6.2.2 Weak elastic anisotropy – Thomsen parameters 75
6.3 Example 76
6.3.1 Setup and earth model 76
6.3.2 Modelling results for isotropic reservoir perturbation 77
6.3.3 Results for transversely isotropic reservoir perturbation . . . 81
6.3.4 Computing time 94
6.3.5 Conclusions 94

7 Conclusions and perspectives **97**

A Implementation of BRM **99**
A.1 Outline of the algorithm 99
A.2 Generation of Green's functions – `Green` 99
A.3 Repeat-modelling – `RMod` 101

References **105**

Dank **113**

Lebenslauf **115**

Abstract

In this thesis, I present an alternative approach to time-lapse modelling: The Born Repeat-Modelling technique (BRM). BRM is a combination of finite-difference modelling (FDM) and perturbation theory.

To plan surveys for seismic time-lapse studies, seismograms are usually simulated for a set of earth models that correspond to different stages of the oil production process. Such calculations can be expensive because often FDM is applied in order to achieve the desired accuracy.

In BRM, production effects are considered as small perturbations of the earth model, and I use Born approximation to compute the change of seismograms due to production-induced modifications of the reservoir properties. This approach can be very efficient for time-lapse modelling because production effects are confined to the reservoir region, which is usually only a small part of the earth model. BRM takes into account wave propagation in the overburden with FDM precision and the reciprocity theorem is applied to propagate the wave to the receivers.

I give a detailed description of the proposed modelling scheme and of its scientific background. The theoretical foundations of BRM are derived for land seismic experiments and an extension to the case of marine (pressure) seismograms is given. I investigate the applicability and performance of BRM with several numerical examples. In particular, a test with the Marmousi model demonstrates that BRM can even be applied in the case of an extremely complex overburden. These examples show that BRM normally requires at most a few percent of the computing time of a corresponding FD simulation.

The fracturing of reservoir rocks essentially determines their permeability for reservoir fluids. Investigation of seismic anisotropy often allows the determination of the orientation of small fractures that cannot be directly resolved by seismic waves. Fractures are frequently created or extended in a reservoir by fluid-injection at high pressure. Thus, small changes of the intrinsic reservoir symmetry may be detected in time-lapse surveys. BRM has been generalised to arbitrary anisotropic perturbations of the reservoir properties. As a test of anisotropic BRM, I have modelled the effects of different kinds of transversely isotropic reservoir perturbations in the seismogram.

Chapter 1

Introduction

Geophysics deals with research on the earth's structure and the related physical processes. Virtually the entire volume of our planet is not accessible for direct examination. Therefore, we have to rely mainly on indirect observations.

The investigation of the sub-surface structure with seismic waves (the subject of seismics) has been a history of great success throughout most of the twentieth century. As seismic waves are only weakly attenuated in the earth, they can travel very long distances and provide – depending on the frequency content – a good resolution of underground features.

Owing to their application to the world-wide exploration of natural resources, seismic methods are of great economical importance. Every day, the gas- and oil-producing industry acquires huge amounts of seismic data, a large part of it at sea.

1.1 Seismic reservoir monitoring

Hydrocarbons are extracted from wells drilled in reservoirs of porous rock. Additional boreholes provide information about the local geology, whereas through others water, steam, or chemical fluids are injected into the reservoir to stimulate hydrocarbon production. However, the limited number of boreholes makes it often very difficult to completely characterise the complex distribution of fluid permeability through reservoir rocks. Thus, frequently a considerable amount of hydrocarbons does not reach the production wells.

Originally, seismics was only used to *explore* new hydrocarbon reservoirs. Decisions concerning the development or the exploitation of these resources were mainly based on information obtained from boreholes. This is changing now, because recent technological advances have improved the accuracy and repeatability of seismic experiments. Now, it is possible to quantitatively compare the results of two seismic surveys carried out at different times above the same producing hydrocarbon reservoir. This new technology is called ***time-lapse seismics*** .

Industry increasingly uses time-lapse seismics to visualise production-related changes in oil reservoirs. Thus, information is obtained about the reservoir fluid distribution in between wells, or about the progress of measures of enhanced hydrocarbon recovery. This allows an earlier recognition of potential production problems and of necessary adjustments of production strategy. The importance of seismic reservoir monitoring constantly increases, because economic pressure demands more intensive exploitation of reservoirs (Wang and Nur, 1991; Justice, 1991; Robertson, 1991). In addition, newly discovered resources are often located in a complex geological environment.

In recent years, an increasing number of authors has reported about the successful application of time-lapse geophysics to monitor the effects of hydrocarbon production on reservoir properties. For example, Jenkins et al. (1997) describe seismic monitoring of a pilot steamflood in Indonesia. An early monitoring study of a combustion flood project is presented in the classical paper by Greaves and Fulp (1991). Other interesting case studies related to this topic are found in Lumley (1995), Koster et al. (2000), Matthews (1991), Waite and Sigit (1997), Talley et al. (1998), Johnston et al. (1998, 2000), and Burkhart et al. (2000).

During the course of a monitoring project, two or more seismic surveys are carried out over a hydrocarbon reservoir at different stages of the production process. The difference of the so-obtained data sets is used to find and visualise changes of the elastic properties of the reservoir. However, seismic data acquisition is very expensive. Therefore, particularly careful survey planning is required. Lumley et al. (1997) and Wang (1997) give general criteria for the feasibility of a seismic time-lapse project. Especially if production effects are rather small, or if the reservoir lies under a complex faulted overburden, a detailed feasibility study may be necessary to check whether predicted variations of fluid content can be detected in a future experiment (Hoffmann and Rekdal, 1999; Packwood, 1996; Koster et al., 2000; Al-Fares, 1995).

Typically, seismic forward modelling plays an important part in such a feasibility study (Biondi et al., 1998; Key et al., 1998; Lumley et al., 1994; Simm et al., 1997). Thus, synthetic seismograms are generated that correspond to changes of the elastic reservoir model calculated with petrophysical relations and numerical simulation of fluid flow (Wang and Nur, 1991; Mavko et al., 1998; Anderson et al., 1998).

1.2 Modelling time-lapse seismograms

In general both reservoir and overburden may have a complex geological structure. Therefore, accurate modelling of the complete elastic wave field is required, and typically finite-difference modelling (FDM) is the method of choice. FDM is a

standard seismic modelling technique that replaces the elastodynamic wave equation (Eqn. 2.9) by a difference equation and computes a solution for the wave field on a grid of depth points (for details, see Chapter 3, Virieux (1986), or Kelly et al. (1976)). By choosing a sufficiently fine grid, the numerical error can be adjusted to the specific requirements of the problem. Unfortunately, it is very expensive and time-consuming to simulate entire seismic surveys using FDM, even in 2-D. Therefore, faster alternatives with similarly high accuracy are sought (see Section 3.3 for details).

In this thesis, I present the Born Repeat-Modelling technique (BRM), which I have especially developed to speed up the generation of synthetic time-lapse seismograms. Born Repeat-Modelling is a time-saving extension to FDM. A combination of numerical modelling and elements of scattering theory is applied to calculate the production-induced change of time-lapse seismograms (Kirchner and Shapiro, 1998, 1999, 2000). Wave propagation in the overburden is taken into account with FDM precision. Changes in the reservoir are considered as small perturbations of the original earth model and the change of seismograms is calculated with Born approximation. BRM supports detailed geological structure in all parts of the earth model, but because of the perturbation approach there are restrictions to the magnitude of changes of reservoir properties. A detailed description of the proposed procedure is given in Chapter 4.

1.3 Overview of this thesis

My aim is to provide a report of my work that can be understood not only by specialists of time-lapse geophysics but also by people with a physical or mathematical background. Hence, I start with a summary of basic principles of reflection seismics (Section 1.4) and of the theory of elastic wave propagation relevant for the understanding of the subsequent chapters (Chapter 2). The expert reader is advised to skip these parts and – when necessary – to follow the explicit references to the respective equations and sections of Chapter 2.

Chapter 3 gives an overview of existing modelling schemes particularly relevant for time-lapse seismics. I briefly describe the basics of finite-difference modelling (FDM), of Lecomte's hybrid modelling technique, and of FD-injection. The former is an accurate and very versatile standard technique, which also serves as a part of BRM. The latter two have been selected as two prominent examples of recently developed, specialised time-lapse modelling techniques.

Chapter 4 is the central chapter of my thesis. It contains a detailed review of the standard form of the Born Repeat-Modelling procedure (BRM) and a discussion of its accuracy and efficiency. In an example, the production-induced change of displacement seismograms is simulated in 2-D for all possible types of isotropic perturbations of the elastic properties of the reservoir.

Seismic data acquisition with an areal distribution of sources and receivers provides images of the reservoir with much better quality, which is essential for time-lapse application. In Section 4.5, a test with a three-dimensional earth model demonstrates the potential usefulness of BRM in 3-D.

BRM can even handle earth models with an extremely complex overburden structure, like the Marmousi model. This is demonstrated in Section 4.6 for a fluid-substitution scenario based on the Marmousi model.

The standard form of BRM allows the simulation of the consequences of isotropic changes of the reservoir as recorded on land. Extensions to the cases of pressure seismograms and to anisotropic perturbations of the reservoir are given in Chapter 5 and Chapter 6. Both are relevant in practice because pressure is recorded in marine seismic surveys and anisotropy of the reservoir is an important indicator of fracturing. The feasibility of both extensions is investigated in two numerical examples.

My work involved certain computational difficulties, and the implementation of the BRM algorithm on several computers. Therefore, some important aspects of implementation are described in the appendix. Among others, this includes flow charts of the actual implementations, the description of solutions to problems of convergence and data management (Appendix A).

1.4 Basic concepts of exploration seismics

1.4.1 The reflection seismic experiment

In a reflection seismic experiment, controlled sources of seismic energy are used to generate elastic waves in the underground. These waves are reflected, refracted, or diffracted by sub-surface heterogeneities. Seismometers are spread out in dense linear or areal arrangements on the earth's surface to detect reflected or backscattered waves.

On land, seismic receivers are called geophones. They record one, or all three components of the vector of particle velocity, which is equivalent to particle displacement. Marine receivers sense incremental pressure. They are called hydrophones. The data are generally recorded with digital equipment. Subsequent processing and analysis is done with the help of supercomputers. Hereby, the significant information is amplified against the noise, and images of the sub-surface are generated that allow geological interpretation (see, e.g., Sheriff and Geldart, 1995; Yilmaz, 1987; Scales, 1994).

Figure 1.1 shows a sketch of a marine seismic experiment as typically carried out for hydrocarbon exploration. The seismic vessel pulls the seismic source(s) and

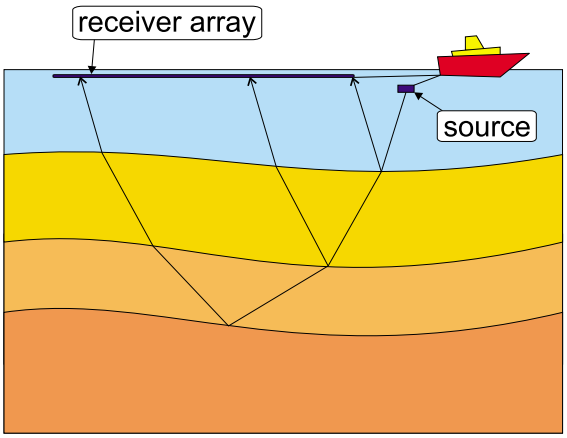

Figure 1.1: Sketch of a marine seismic experiment typical for hydrocarbon exploration. The seismic vessel pulls the seismic sources, and behind them long arrays of seismic receivers. As indicated by the black arrows, the seismic energy is transmitted or reflected at interfaces between layers with different elastic properties. Travel times of elastic waves between source and receiver provide information on the location of these interfaces. This picture is drawn in a way that implies a smoothly varying medium.

behind them long arrays of seismic receivers called streamers . The black arrows indicate some possible paths that the seismic energy may take. The seismic source is fired periodically. Thus, large amounts of data are created that provide information on the structure of the underground. What geophysicists call a seismic receiver is actually a whole cluster of detectors called a group Similarly, the seismic source is in fact an array of sources fired together to create the desired source signal or directivity. However, such details are not relevant for my following considerations.

The time-series, or seismogram, recorded by each receiver is called a seismic trace. The set of traces recorded by all receivers for a given source is called a common-source or common-shot (CS) gather. The common-shot gather is sometimes simply referred to as "shot gather". There are other ways of (re-)organising traces into gathers. For example, I will sometimes look at all traces whose source-receiver distance (called the offset) is equal to a fixed value. This set is called a common-offset (CO) gather. Sometimes the term "section" instead of "gather".

A seismic section particularly important for exploration seismics is the zero-offset (ZO) gather. It is a special case of a common-offset gather with offset equal zero, i.e., with source and receiver at the same location. A zero-offset gather cannot be measured in reality but must be simulated from other seismic data or by forward modelling. Illustrations of the two types of gathers used in this thesis are depicted in Figure 1.2.

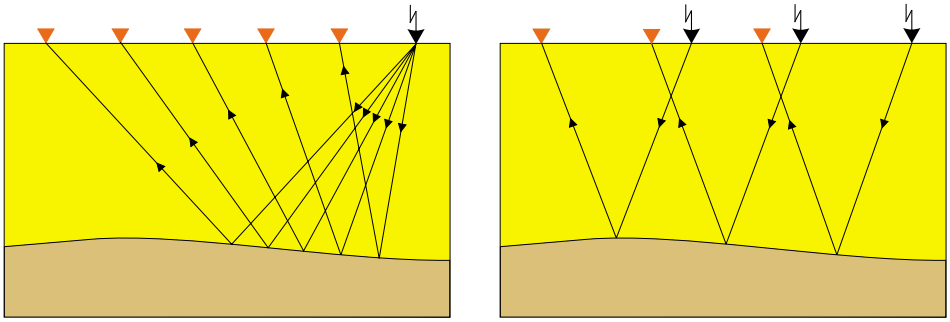

(a) Common-shot configuration **(b)** Common-offset configuration

Figure 1.2: Illustration of seismic recording geometries relevant for this thesis.

1.4.2 Time-lapse seismics

In recent years, it has become very popular to repeat seismic surveys near hydrocarbon reservoirs in order to monitor the development of their elastic properties induced by oil production.

Figure 1.3 illustrates the principle of time-lapse seismics. A seismic survey over a hydrocarbon reservoir is repeated at different stages of the production process. Production-induced changes of the elastic reservoir properties modify the seismic response. Information about the progress of the production programme can be extracted from these data sets by means of suitable processing.

The so-called *difference seismograms* are created by subtracting the seismic data from two subsequent seismic surveys. Difference seismograms are very useful for interpretation because production effects should be associated with high amplitudes in the difference sections. However, repeatability of seismic surveys is a critical issue for time-lapse experiments, because random variations of the source signal, recording geometry, the weather conditions, etc., tend to obscure the desired effects. The availability of special adaptive time-lapse processing techniques like cross-equalisation was a precondition for the feasibility of seismic reservoir monitoring.

Of course, repeatability is not a problem for seismic modelling. Apart from their computational cost, the generation of synthetic difference seismograms is quite straightforward. Variations of seismograms for other reasons than hydrocarbon production will be ignored throughout this thesis.

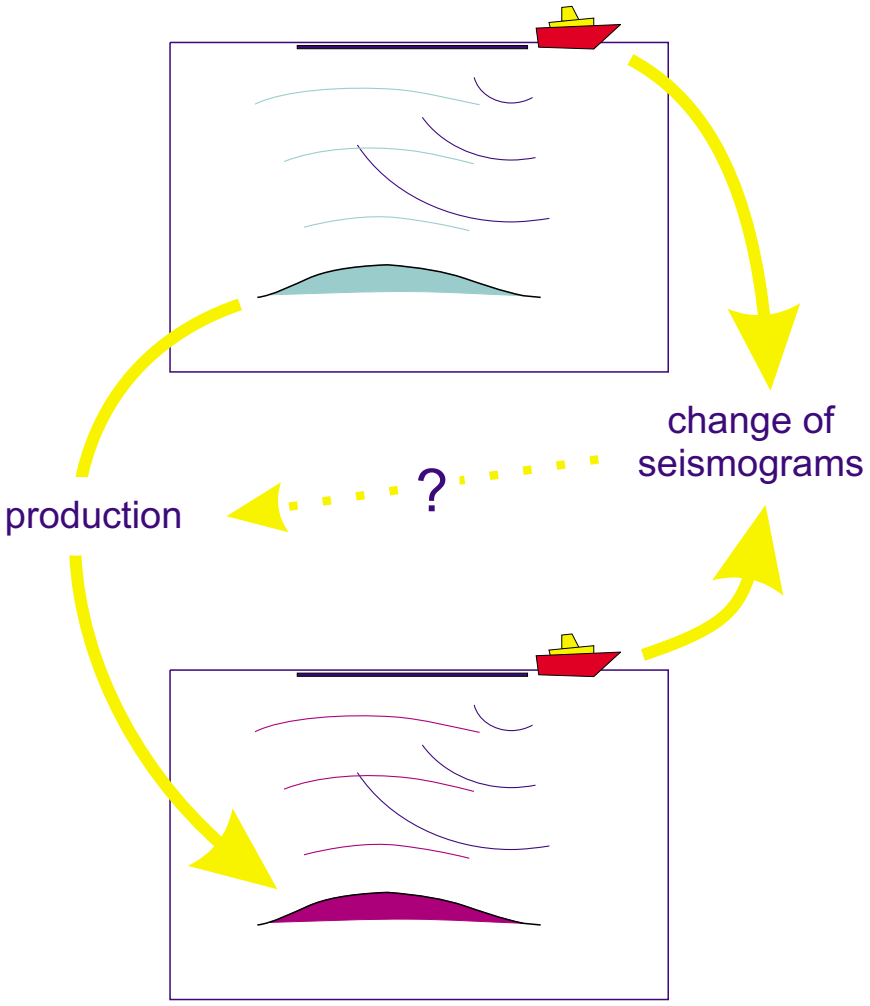

Figure 1.3: The principle of time-lapse seismics. A seismic survey over a hydrocarbon reservoir is repeated at different stages of the production process. Production-induced changes of the elastic reservoir properties modify the seismic response. Information about the progress of the production programme can be extracted from the so-obtained data sets by means of suitable processing.

Chapter 2

Fundamentals of elastic wave propagation

2.1 Introductory remarks

The theory of mechanics of the solid body is fundamental for the description of wave propagation. It is treated in several text books. My aim in this chapter is to bring together all the mathematical concepts and formulas referred to in the following chapters in consistent notation. For more details, I refer to Aki and Richards (1980), Hudson (1980), Sheriff and Geldart (1995), and particularly to the classical book by Auld (1990). Hertweck (2000) gives a comprehensive introduction to ray theory.

Throughout my thesis, the Einstein summation convention applies, i.e., a repeated index implies summation with respect to this index, and "$q_{,j}$" stands for the spatial partial derivative of the quantity q with respect to the jth coordinate of the Cartesian coordinate system. Indices run from one to three for three-dimensional problems and take on the values one and three in the two-dimensional case (representing x- and z-coordinates). Finally, I assume that all functions in the subsequent sections are sufficiently regular to allow the intended operations, particularly with respect to differentiability. Only displacement fields are considered that have continuous second derivatives in all points apart from the source location.

2.2 Description of elastic bodies

2.2.1 The elastic continuum

Since all phenomena of interest to seismics happen on a macroscopical scale, the solid body is described as if it were a continuum, and the discrete nature of matter

is ignored. However to derive the basic concepts, the solid body is usually divided in thought into small but finite portions called particles. These particles can exert forces (tractions) on each other via the surfaces where they are connected.

Consider a portion of a solid body inside the volume V, bounded by the surface S of V. When this particle is displaced from its equilibrium position, restoring forces arise. These forces accelerate the particle according to Newton's second law (Aki and Richards, 1980, Eqn. 2.5):

$$\iiint_V d^3r\, \rho(\mathbf{r}) \frac{\partial^2}{\partial t^2} \mathbf{u}(\mathbf{r}, t) \quad = \quad \iint_S dS(\mathbf{r})\, \mathbf{T}(\mathbf{n}; \mathbf{r}, t) \; + \; \iiint_V d^3r\, \mathbf{f}(\mathbf{r}, t) \; . \tag{2.1}$$

Here, $\mathbf{u}(\mathbf{r}, t)$ is the displacement vector at time t and at location $\mathbf{r}$. $\rho(\mathbf{r}, t)$ is the density of the solid body, and $\mathbf{T}(\mathbf{n}; \mathbf{r}, t)$ is the traction acting on the particle at $\mathbf{r}$ through its bounding surface S. The traction is a function of the orientation of the outward surface normal $\mathbf{n}$. In addition, there can be external forces acting directly upon particles in the interior of a body. $\mathbf{f}(\mathbf{r}, t)$ denotes the density of these "body forces". In seismics, $\mathbf{f}$ usually represents the source.

2.2.2 Stress and strain

Using the stress tensor σ, Equation 2.1 may be re-written in differential form:

$$\rho(\mathbf{r}) \frac{\partial^2}{\partial t^2} u_i(\mathbf{r}, t) \quad = \quad \sigma_{ji,j}(\mathbf{r}, t) + f_i(\mathbf{r}, t) \; . \tag{2.2}$$

This is the equation of motion for the continuum. It relates the forces in the medium to the measurable displacement. σ is a symmetrical tensor of second order. Via $T_i(\mathbf{n}; \mathbf{r}, t) = \sigma_{ji}(\mathbf{r}, t) n_j(\mathbf{r})$, it describes the complete stress condition at a certain point for any orientation $\mathbf{n}$ of the probing surface.

In rigid translations and rotations, the displacement vector $\mathbf{u}$ will be non-zero. To describe particle deformation only, the strain tensor

$$e_{ij}(\mathbf{r}, t) \quad = \quad \frac{1}{2} \left(u_{i,j}(\mathbf{r}, t) + u_{j,i}(\mathbf{r}, t) \right) \tag{2.3}$$

is more appropriate. Obviously, the strain tensor is symmetric, as well. Strictly speaking, this is only the linearised form of e_{ij}. The full strain tensor contains additional terms with products of displacement components. Seismic wave propagation involves only small deformations. Hence in Equation 2.3, second-order terms of displacement are neglected.

2.2.3 Linear elasticity and the stiffness tensor

The relation between stress and strain (constitutive relation) is a property of the medium, in which a wave propagates. For small deformations, it is an experimentally observed fact that the strain in a deformed body is proportional to the applied stress (Hooke's law). In general, this means that the components of stress are linear combinations of the strain components:

$$\sigma_{ij} = c_{ijkl}\, e_{kl} \,. \tag{2.4}$$

c_{ijkl} is called stiffness tensor, or elastic tensor. Its components (and some of their linear combinations) are called elastic moduli. These parameters are measures of the resistance to stress. Typical values of the elastic moduli for solids or fluids are in the range from 1 GPa to more than 10 GPa.

2.2.4 Symmetry properties and abbreviated notation

The symmetry of stress and strain tensors (together with thermodynamic considerations) implies the following symmetry properties for the stiffness tensor (e.g. Auld, 1990):

$$c_{ijkl} = c_{jikl} = c_{ijlk} = c_{klij} \,. \tag{2.5}$$

For reasons of symmetry, only six components of the stress and strain tensors can be independent. Therefore frequently, an abbreviated notation is used to simplify calculations. The independent components are arranged in a six-component column vector instead of a 3×3-matrix with

$$(\sigma_I) = \left(\sigma_{xx}, \quad \sigma_{yy}, \quad \sigma_{zz}, \quad \sigma_{yz}, \quad \sigma_{xz}, \quad \sigma_{xy} \right)^{\mathrm{T}} \tag{2.6}$$

for the stress, and

$$(e_I) = \left(e_{xx}, \quad e_{yy}, \quad e_{zz}, \quad 2e_{yz}, \quad 2e_{xz}, \quad 2e_{xy} \right)^{\mathrm{T}} \tag{2.7}$$

for the strain. Analogously, the 21 independent components of the stiffness tensor are arranged in a symmetric 6×6-matrix in such a way that the constitutive relation (Eqn. 2.4) remains valid:

$$(c_{IJ}) = \begin{pmatrix} c_{xxxx} & c_{xxyy} & c_{xxzz} & c_{xxyz} & c_{xxxz} & c_{xxxy} \\ & c_{yyyy} & c_{yyzz} & c_{yyyz} & c_{yyxz} & c_{yyxy} \\ & & c_{zzzz} & c_{zzyz} & c_{zzxz} & c_{zzxy} \\ & & & c_{yzyz} & c_{yzxz} & c_{yzxy} \\ & & & & c_{xzxz} & c_{xzxy} \\ & & & & & c_{xyxy} \end{pmatrix} \tag{2.8}$$

In abbreviated notation, indices obviously run from 1 to 6. They are written in capital letters to distinguish from detailed notation. In a two-dimensional medium the number of independent components reduces to three for stress and strain, and six for the stiffness tensor. Thus, possible values for indices are only 1, 3, and 5.

In my thesis, I use the abbreviated notation in the sections where BRM is applied to compute seismograms. It is also very useful to explain the algorithm used in my implementation of BRM. For analytical calculations, detailed notation is preferred.

2.3 Theory of wave propagation

2.3.1 The elastodynamic wave equation

Inserting Equation 2.4 into the equation of motion (Eqn. 2.2) yields the elastodynamic wave equation:

$$\rho(\mathbf{r}) \frac{\partial^2}{\partial t^2} u_i(\mathbf{r}, t) \quad = \quad \left[c_{ijkl}(\mathbf{r})\, u_{k,l}(\mathbf{r}, t) \right]_{,j} + f_i(\mathbf{r}, t) \ . \tag{2.9}$$

This hyperbolic system of three partial differential equations determines wave motion in linearly elastic media. All types of waves normally used in seismics are solutions of this system. Depending on the choice of c_{ijkl} and ρ, the medium may be heterogeneous and anisotropic.

2.3.2 Elastic parameters for isotropic media

In general media, the wave field $\mathbf{u}$ and hence its mathematical description are extremely complex. For most natural materials – at least on the macroscopic scale that is of interest in seismics – the elastic behaviour does not depend on the orientation of the material. For these isotropic media, this implies that the elastic tensor can be expressed in terms of only two independent parameters, the so-called Lamé parameters λ and μ (e.g. Hudson, 1980, Eqn. 1.23):

$$c_{ijkl}(\mathbf{r}) \quad = \quad \lambda(\mathbf{r}) \delta_{ij} \delta_{kl} + \mu(\mathbf{r}) \left(\delta_{ik} \delta_{jl} + \delta_{il} \delta_{jk} \right) \ , \tag{2.10}$$

with the Kronecker symbol

$$\delta_{ij} \quad = \quad \begin{cases} 1, & \text{for } i = j \\ 0, & \text{for } i \neq j \end{cases} \ . \tag{2.11}$$

μ is also called the shear modulus, because it is a measure for resistance to shear stress.

Another, more flexible parametrisation uses the components of the stiffness tensor in abbreviated notation. For the isotropic case, the independent elastic moduli are c_{11} and c_{55}, because the other stiffness components are equal to, or linear combinations of these two (Auld, 1990):

$$\begin{aligned} c_{11} &= c_{22} = c_{33} \quad (= \lambda + 2\mu) \\ c_{55} &= c_{44} = c_{66} \quad (= \mu) \\ c_{11} + 2\,c_{55} &= c_{12} = c_{13} = c_{23} \quad (= c_{21} = c_{31} = c_{32}) \end{aligned} \tag{2.12}$$

The other stiffness components are equal zero. From the non-zero components, only c_{11}, c_{33}, c_{55}, and c_{13} are there in two dimensions (in seismics, x and z are the spatial coordinates used for 2-D problems). Therefore, c_{55} was chosen instead of c_{44}. For anisotropic media, this set of parameters is easily generalised (Chapter 6).

2.3.3 P-waves and S-waves

For a homogeneous, isotropic, elastic material, the wave equation (Eqn. 2.9) becomes (Hudson, 1980, Eqn. 2.1)

$$\begin{aligned} \rho \frac{\partial^2}{\partial t^2} \mathbf{u}(\mathbf{r}, t) &= \mathbf{f}(\mathbf{r}, t) + (\lambda + 2\mu)\, \nabla\, [\nabla \cdot \mathbf{u}(\mathbf{r}, t)] \\ &\quad - \mu\, \nabla \times [\nabla \times \mathbf{u}(\mathbf{r}, t)] \ , \end{aligned} \tag{2.13}$$

since λ and μ are now constants. If we take the divergence and curl of this equation, we obtain two separate wave equations for the compressional ($\nabla \cdot \mathbf{u}$) and the rotational ($\nabla \times \mathbf{u}$) parts of the wave field. Consequently, there are two independent types of waves, which travel at different wave speeds.

The compressional wave is called P-wave ("primary"), because it corresponds to the first event usually observed in earthquake seismograms. It propagates with velocity

$$v_{\mathrm{P}} = \sqrt{\tfrac{\lambda + 2\mu}{\rho}} = \sqrt{\tfrac{c_{11}}{\rho}} \ . \tag{2.14}$$

The displacement vector is longitudinal to the direction of propagation. The other wave, which is transversely polarised, is called S-wave ("secondary"). With

$$v_{\mathrm{S}} = \sqrt{\tfrac{\mu}{\rho}} = \sqrt{\tfrac{c_{55}}{\rho}} \ , \tag{2.15}$$

the speed of the S-wave has to be lower than that of the P-wave, because, for thermodynamic reasons, all elastic moduli are non-negative numbers (Auld, 1990). The S-wave usually makes the *second* major event in earthquake seismograms, hence its name. Typical velocities of seismic body waves encountered in crustal seismology

range from $1000\frac{m}{s}$ for S-waves in shallow regions up to more than $5000\frac{m}{s}$ in deep layers.

For general media, the P- and S-waves are coupled. In the process of scattering or reflection at a heterogeneity, an incident wave of one type will give rise to reflected, refracted, or scattered waves of the other type. In addition, in an anisotropic medium, the S-wave may split into *two* orthogonal polarisations, which travel with different wave speeds (see also Chapter 6).

2.3.4 Wave propagation in fluids

From the point of view of wave propagation, a fluid is characterised by the absence of shear stress. The shear modulus μ of a fluid is equal to zero and λ assumes the role of the bulk modulus (inverse of compressibility). For seismic prospecting, this case is very important in two ways: Firstly, acoustics is often used as an approximation for wave propagation in solids. Secondly, the a large part of oil and gas resources are now discovered off-shore. Hence, we must take into account that seismic waves must propagate through the water layer before they can penetrate into the ground (Chapter 5).

In a fluid, there is only the compressional wave, which is more easily described by the (scalar) pressure field than by the displacement (Hudson, 1980, Eqn. 1.18):

$$p(\mathbf{r},t) \quad = \quad -\tfrac{1}{3}\,\sigma_{kk}(\mathbf{r},t) \quad = \quad -\lambda(\mathbf{r})\,\nabla\cdot\mathbf{u}(\mathbf{r},t) \tag{2.16}$$

By substituting the bulk modulus $K = \lambda + \frac{2}{3}\mu$, this equation is generalised to the case of an isotropic linear elastic solid subject to hydrostatic stress.

Wave propagation in fluids is governed by the (scalar) acoustic wave equation:

$$\frac{1}{\lambda(\mathbf{r})}\,\frac{\partial^2}{\partial t^2}p(\mathbf{r},t) \quad = \quad \nabla\left[\frac{1}{\rho(\mathbf{r})}\,\nabla\Big(p(\mathbf{r},t)\;+\;p_0(\mathbf{r},t)\Big)\right]\;, \tag{2.17}$$

which is easily obtained from Equation 2.9 by applying the divergence operator. The applied pressure p_0 represents the pressure distribution equivalent to the force density $\mathbf{f}(\mathbf{r},t) = -\nabla p_0(\mathbf{r},t)$.

2.3.5 Elastic properties of fluid-saturated porous solids

In a hydrocarbon reservoir, elastic waves propagate through porous fluid-saturated rock. One of the most important problems of rock physics is the prediction of effective seismic velocities in rocks saturated with one fluid from properties of rocks saturated with a second fluid – or, equivalently, saturated rock velocities from dry rock velocities. This is the *fluid substitution problem*.

Geological conditions in such media are very heterogeneous and elastic properties normally vary on length scales much smaller than the seismic wave lengths. Therefore, often a quasi-static effective-medium description of the reservoir rock is used. Generally, the fluid in the pores of a saturated rock increases its resistance to compression. Gassmann's equation predicts the resulting increase in effective bulk modulus K_{sat} of the saturated rock (Mavko et al., 1998):

$$\frac{K_{\text{sat}}}{K_0 - K_{\text{sat}}} = \frac{K_{\text{dry}}}{K_0 - K_{\text{dry}}} + \frac{K_{\text{fl}}}{\phi(K_0 - K_{\text{fl}})} \tag{2.18}$$

with the bulk modulus K_0 of the solid making up the rock, the effective bulk modulus K_{dry} of the dry (porous) rock frame, the bulk modulus K_{fl} of the saturating fluid, and the porosity ϕ.

The effective shear modulus of the saturated rock μ_{sat} remains unchanged by the presence of a pore fluid:

$$\mu_{\text{sat}} = \mu_{\text{dry}} \ . \tag{2.19}$$

Gassmann's equation assumes statistically isotropic pore space, but does not make any assumption concerning pore space geometry. It is valid at frequencies low enough to allow pore pressure to equilibrate throughout the pore space. This is normally the case in seismic experiments.

2.4 Green's function and related theorems

2.4.1 Green's function

Sources of seismic waves are usually small compared to the predominant wavelength they produce. Therefore, they are commonly described as point-sources. The simplest kind of seismic source is the impulsive point-source, which is given by

$$f_{im}(\mathbf{r}, t; \mathbf{r}', t') = \delta(\mathbf{r} - \mathbf{r}')\,\delta(t - t')\,\delta_{im} \ . \tag{2.20}$$

δ is the Dirac delta-function. The unit impulse is applied at $\mathbf{r} = \mathbf{r}'$ and $t = t'$ and in the m-direction.

The displacement field $G_{im}(\mathbf{r}, t; \mathbf{r}', t')$ from such a source is the elastodynamic Green's function. Thus, it satisfies the following differential equation:

$$\begin{aligned} \rho(\mathbf{r})\frac{\partial^2}{\partial t^2} G_{im}(\mathbf{r}, t; \mathbf{r}', t') &= \delta(\mathbf{r} - \mathbf{r}')\,\delta(t - t')\,\delta_{im} \\ &\quad + \left[c_{ijkl}(\mathbf{r})\, G_{km,l}(\mathbf{r}, t; \mathbf{r}', t') \right]_{,j} \ . \end{aligned} \tag{2.21}$$

The Green's function is a second-order tensor where the indices i and m each have a range of three, making a total of nine components altogether.

I will always use causal initial conditions for the Green's function, which means that the medium had been in elastic equilibrium before the source pulse was initiated at time t':

$$\begin{aligned} G_{im}(\mathbf{r},t;\mathbf{r}',t') &= 0, \quad \frac{\partial}{\partial t} G_{im}(\mathbf{r},t;\mathbf{r}',t') = 0 \\ \text{for} \quad t \leq t' \quad &\text{and} \quad \mathbf{r} \neq \mathbf{r}'. \end{aligned} \tag{2.22}$$

On the boundary of the volume, inside which Green's function is sought, the displacement or the traction must be specified. For example, Equation 2.23 shows that boundary conditions can have great influence on the field. For an unbounded volume, usually $G_{im}(\mathbf{r},t;\mathbf{r}',t') \to 0$ is required for $|\mathbf{r}-\mathbf{r}'| \to \infty$ (Sommerfeld radiation condition, e.g., Scales, 1994).

2.4.2 The representation theorem

The following identity shows that the knowledge of the complete Green's function implies the general solution of the elastodynamic wave equation (Eqn. 2.9) for a given medium inside a given volume V and for an arbitrary source configuration (Aki and Richards, 1980, Eqn. 2.41):

$$\begin{aligned} u_i(\mathbf{r},t) &= \int_{-\infty}^{\infty} dt' \iiint_V d^3r' \, f_m(\mathbf{r}',t') \, G_{mi}(\mathbf{r}',t;\mathbf{r},t') \\ &+ \int_{-\infty}^{\infty} dt' \iint_S dS_j(\mathbf{r}') \Big\{ G_{mi}(\mathbf{r}',t;\mathbf{r},t') \, \sigma_{ij}(\mathbf{r}',t') \\ &- u_m(\mathbf{r}',t') \, c_{mjkl}(\mathbf{r}) \, G_{ki,l}(\mathbf{r}',t;\mathbf{r},t') \Big\} \, . \end{aligned} \tag{2.23}$$

Here, all spatial integrations are over $\mathbf{r}'$, and $\mathbf{dS}(\mathbf{r}')$ is the outward directed surface element of the surface S of V at the point $\mathbf{r}'$. Equation 2.23 is called representation theorem. It is easily derived from Equations 2.9, and 2.21 using the Gauss divergence theorem (Aki and Richards, 1980; Gubernatis et al., 1977a). In addition, the assumption was made that before a certain time in the past the medium had been in equilibrium, which is, however, not a real restriction for seismic purposes.

The representation theorem states how the displacement field $\mathbf{u}$ at a certain point $\mathbf{r}$ is composed from contributions due to the distribution of (body force) sources $\mathbf{f}$ throughout V, plus contributions due to the given displacement and stress fields on the surface S (i.e., the boundary conditions on S).

2.4.3 Reciprocity

The Green's function possesses some symmetry properties. The most important one for this thesis is the reciprocity theorem (Aki and Richards, 1980, Eqn. 2.39):

$$G_{im}(\mathbf{r}, t; \mathbf{r}', t') \quad = \quad G_{mi}(\mathbf{r}', t; \mathbf{r}, t') \,, \tag{2.24}$$

This reciprocal relation allows to interchange source and receiver locations. Thus, the same Green's function can be used to propagate a wave from the source to the receiver, and back again.

Equation 2.24 is valid, if the boundary conditions are chosen in such a way that the surface integral vanishes in Equation 2.23. This is can be achieved, e.g., if the displacement or the traction vanishes everywhere on the boundary S at all times. The reciprocity property is derived by substituting the point-source according to Equation 2.20 into the representation theorem. Then, the result is compared with the Green's function corresponding to this source configuration.

2.5 Scattering at small heterogeneities

2.5.1 Waves in inhomogeneous media

In inhomogeneous media, seismic waves cannot propagate undisturbed. Fundamental to seismic exploration is that waves interact with the heterogeneities of the medium. Depending on the shape and size of the heterogeneity, we call this interaction reflection, refraction, or scattering.

Reflection and refraction is used to determine the location of large-scale features like interfaces between geological layers (see, e.g., Yilmaz, 1987; Sheriff and Geldart, 1995; Wood and Treitel, 1975). Conversely, prediction of small-scale structures, or effective seismic properties like effective propagation velocities, or attenuation coefficients of the (coherent) wave field is usually done with scattering theory (e.g. Shapiro and Hubral, 1999; Müller and Shapiro, 2000; Gold, 1997). The concept of scattering at small inhomogeneities of arbitrary shape is very important for this thesis (Chapter 4).

Only very simple geometries of the medium heterogeneities allow to solve the elastodynamic wave equation (Eqn. 2.9) exactly. Hence, we have to make (physical) approximations to obtain analytical expressions for generally shaped scatterers (e.g. Wu, 1989).

Because of its applicability to inclusions of general shape and structure, the integral equation method, especially the single-scattering or Born approximation has been

successful in seismics. When applied in reflection mode, the Born approximation gives a useful description of the waves scattered from heterogeneities that are small compared to the wavelength of the incident wave (Gubernatis et al., 1977b; Sato and Fehler, 1998).

2.5.2 The perturbation method

To derive the Born approximation of the scattered field, I use a perturbation approach following Gubernatis et al. (1977a). For further reference see, e.g. Burridge et al. (1998), Rytov et al. (1989), Wu (1989), Miles (1960), or Tygel and Ursin (1997).

Representation of the scattered field as an integral equation

I compare two very similar elastic earth models. The background or reference model is characterised by the density field $\rho(\mathbf{r})$, and the elastic moduli $c_{ijkl}(\mathbf{r})$. The second earth model is obtained by perturbing these properties inside a finite target zone by small amounts $\delta c_{ijkl}(\mathbf{r})$ and $\delta\rho(\mathbf{r})$, obtaining

$$\begin{aligned} \rho^{\mathrm{P}}(\mathbf{r}) &= \rho(\mathbf{r}) + \delta\rho(\mathbf{r}) \\ c^{\mathrm{P}}_{ijkl}(\mathbf{r}) &= c_{ijkl}(\mathbf{r}) + \delta c_{ijkl}(\mathbf{r}) \end{aligned} \tag{2.25}$$

To indicate quantities that belong to the *perturbed* model I use the superscript "^{P}". Usually, the elastic parameters change only inside a small region. Outside the target zone $\delta\rho$ and δc_{ijkl} vanish.

With regard to Chapter 4, I assume an unbounded medium, in which the wave field vanishes at large distances (Eqn. 2.22). This corresponds to the typical situation in seismics and scattering theory.

Let $u^{\mathrm{P}}(\mathbf{r},t)$ be the displacement field for the elastic medium characterised by the above properties. After inserting Equations 2.25, the elastodynamic wave equation can be arranged as follows:

$$\begin{aligned} \rho(\mathbf{r})\frac{\partial^2}{\partial t^2}u^{\mathrm{P}}_i(\mathbf{r},t) &= \Big[c_{ijkl}(\mathbf{r})\,u^{\mathrm{P}}_{k,l}(\mathbf{r},t)\Big]_{,j} + f_i(\mathbf{r},t) \\ &\quad - \delta\rho(\mathbf{r})\frac{\partial^2}{\partial t^2}u^{\mathrm{P}}_i(\mathbf{r},t) - \Big[\delta c_{ijkl}(\mathbf{r})\,u^{\mathrm{P}}_{k,l}(\mathbf{r},t)\Big]_{,j} \,. \end{aligned} \tag{2.26}$$

Apart from the third and fourth terms on the right-hand-side, this is just the wave equation for the background medium (Eqn. 2.9). The additional terms represent the influence of the heterogeneities and are commonly interpreted as secondary sources of the wave field.

Substituting all three source terms for **f** in Equation 2.23 yields an integral equation for $\mathbf{u}^{\mathrm{P}}$:

$$\begin{aligned} u_i^{\mathrm{P}}(\mathbf{r},t) &= u_i(\mathbf{r},t) + \iiint_V d^3r'\, G_{im}(\mathbf{r},t;\mathbf{r}',t') \\ &\quad \cdot \left\{ \frac{\partial}{\partial r_j}\delta c_{ijkl}(\mathbf{r}')\frac{\partial}{\partial r_l} - \delta_{ik}\,\delta\rho(\mathbf{r}')\frac{\partial^2}{\partial t^2} \right\} u_{k,l}^{\mathrm{P}}(\mathbf{r}',t') \,. \end{aligned} \tag{2.27}$$

$u_i(\mathbf{r},t)$ is the displacement field corresponding to the background medium. The bounding surface S was expanded to infinite size. Then, the corresponding surface integral vanishes. In addition, the reciprocity relation (Eqn. 2.24) was used to interchange the arguments of the Green's function.

This integral equation describes the displacement u_i^{P} measured by a seismic receiver at location **r** as the sum of two contributions. On the one hand, there is the background field, which corresponds to the wave coming directly from the source. On the other hand, the integral represents the scattered field as a sum of the contributions of all secondary sources.

Scattering series

To calculate the displacement field at the receiver location **r** from Equation 2.27, we need to know the exact field inside the scattering region, which is generally not available.

A common strategy is to iterate this equation and retain only the leading terms:

$$\begin{aligned} u_i^{\mathrm{P}}(\mathbf{r},t) &= u_i + \iiint_V d^3r'\, G_{im}(\mathbf{r},t;\mathbf{r}',t')\{\ldots\}u_m(\mathbf{r}',t') \\ &+ \iiint_V d^3r' \iiint_V d^3r''\, G_{im}(\mathbf{r},t;\mathbf{r}',t')\{\ldots\}G_{im}(\mathbf{r}',t';\mathbf{r}'',t'')\{\ldots\}u_m(\mathbf{r}'',t'') \\ &+ \ldots \end{aligned} \tag{2.28}$$

To keep the equations short, the operator enclosed in curved braces in Equation 2.27 is abbreviated by $\{\ldots\}$. This infinite series is called scattering series, or Born series. Physically, it is a decomposition of the displacement field according to the number of scattering events involved.

The first term of the series represents the unscattered wave, and the second term is the single-scattering contribution. The third term contains the operator twice and thus corresponds to two-fold scattering, etc.. Figure 2.1 gives an illustration of this principle.

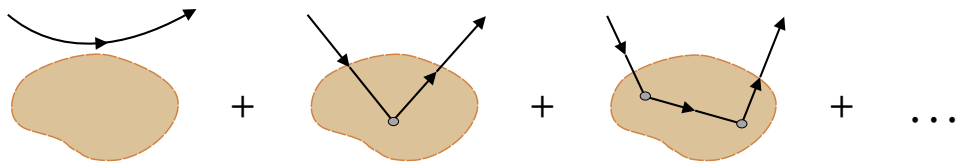

(a) Unscattered. **(b)** Single scattering. **(c)** 2nd-order scattering.

Figure 2.1: Illustration of the scattering series (Eqn. 2.28) after Cohen-Tannoudji et al. (1977)

Born approximation

The infinite series in Equation 2.28 is as intractable as the integral equation itself. However, if scattering is weak, it is very likely that higher-order terms of the scattering series will fall off quickly. Then, we may neglect multiple scattering and retain only the first two terms. The result is the single-scattering or Born approximation:

$$\begin{aligned} u_i^{\mathrm{P}}(\mathbf{r},t) &= u_i(\mathbf{r},t) + \iiint\limits_V d^3r'\, G_{im}(\mathbf{r},t;\mathbf{r}',t') \\ &\quad \cdot \left\{ \frac{\partial}{\partial r_j} \delta c_{ijkl}(\mathbf{r}') \frac{\partial}{\partial r_l} - \delta_{ik}\, \delta\rho(\mathbf{r}') \frac{\partial^2}{\partial t^2} \right\} u_{k,l}(\mathbf{r}',t') \,. \end{aligned} \tag{2.29}$$

δc_{ijkl} and $\delta\rho$ are often called perturbations of the medium because of this principle to search for a solution of a complicated problem by considering it as a perturbation of a known situation.

Born approximation replaces the exact displacement in the scattering volume by the incident field. An error is introduced, because inside the scattering region the incident wave will be distorted. Usually, the deviation $|\mathbf{u}^{\mathrm{P}} - \mathbf{u}|$ grows with the distance covered inside the scatterer, because interaction effects accumulate.

Analytical and numerical investigations suggest that Born approximation will very likely give good results, if the size of the scattering region is much smaller than the wavelength, or if the medium perturbations are not too large. For details, I refer to Hudson (1980); Kennet (1972); Gubernatis et al. (1977b); Rytov et al. (1989); Wu (1989); Keller (1969); Oristaglio (1985). See also the discussion of validity given in Section 4.3.2.

Several alternative methods have been suggested to (approximately) sum the scattering series (see, e.g., Habashy et al., 1993; Chapman and Coates, 1994; Trantanella et al., 1995). However, such approaches often involve additional computational ef-

fort and numerical difficulties that outweigh their advantages for numerical application to complex media.

2.6 Discrete representation of continuous functions — the sampling theorem

Numerical modelling or digital signal processing always involves the discrete representation of continuous functions. It is clear that discrete sampling may introduce an error, which will decrease, if the spacing between samples is refined. Shortage of computer memory and long computing times often make us want to use coarser grids. The sampling theorem gives a criterion for the choice of the sampling interval in the case of band limited functions (Press et al., 1992, chapter 12).

A function $u(t)$ is called band limited, if the spectrum of u is zero for frequencies outside of the interval $[-f_\nu; f_\nu]$. The ***sampling theorem*** states that a band limited function is completely determined by its values $f(t_n)$ at the countable set of points $t_n = n \cdot \Delta t$ (integer n) with the sampling interval

$$\Delta t = \frac{1}{2 f_\nu} . \tag{2.30}$$

Conversely, the sampling interval Δt of a certain time series defines the so-called Nyquist frequency $f_\nu = 1/2\Delta t$. All frequency components originally beyond the Nyquist frequency will be spuriously shifted into the interval $[-f_\nu; f_\nu]$. This kind of error is called aliasing. According to the sampling theorem, the critical sampling of a harmonic function is two samples per period. Figure 2.2 shows an example of aliasing for a harmonic function. The sampling interval is much too coarse, and produces an apparent frequency of $\frac{1}{3}$ of the true frequency.

Thus, the sampling theorem sets a lower limit to the number of samples used to discretise a certain time series. For Born Repeat-Modelling (BRM) the sampling interval for the time axis is chosen according to the sampling theorem. The theoretical limit for discretisation of the spatial coordinates in BRM is also given by the sampling theorem. However, numerical differentiation of the Green's function demands a slightly finer grid in the current implementation (see also Sections 3.2.3 and 3.2.5).

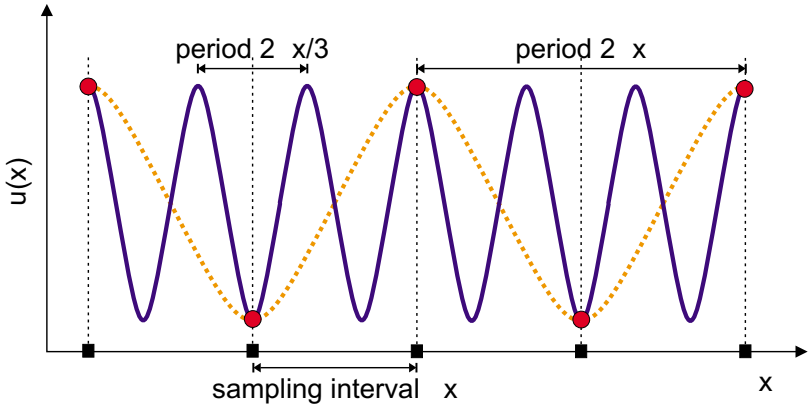

Figure 2.2: Illustration of aliasing. The sampling interval is much too coarse for the higher-frequent harmonic function and produces an apparent frequency of $\frac{1}{3}$ of the true frequency.

Chapter 3

Modelling time-lapse seismograms

3.1 Introduction

3.1.1 Numerical seismic modelling

The term seismic modelling means the calculation of synthetic seismograms for a given (elastic) earth model, source configuration, and recording geometry in order to, e.g., define the limits of seismic resolution, assess the ambiguity of interpretation, or just predict what features certain interesting sub-surface structures will cause in seismograms. For this, it is usually necessary to solve the elastodynamic wave equation (Eqn. 2.9) at least in parts of the elastic earth model. In most cases we have to resort to approximations and numerical calculations to complete this task, because for most earth models there is no analytical solution.

In practice, numerical modelling of complete seismic surveys very often reaches the limits of the available computational resources, particularly for three-dimensional models. Driven by the need to balance accuracy / generality on the one hand and computational cost on the other hand, numerous different modelling techniques have been designed with regard to special applications or purposes. Very popular are the methods based on wavefronts and rays (Červený, 2000), which can calculate travel times and amplitudes of seismic waves in an efficient way. Ray-based methods are therefore widely used for quick seismic modelling, or to compute large Green's function tables for seismic imaging. However, this approach involves a high-frequency approximation and is thus restricted to slowly varying, or "smooth", media.

Another popular class of modelling techniques is aimed at wave propagation in completely heterogeneous media. These methods discretise the medium and the

wave equation, and thus provide a solution for the wave field on a (regular or irregular) grid. The detail and accuracy of the results can be adjusted by refining the grid. For exploration seismics, the most important member of this group is the finite-difference modelling technique (FDM), which is described in detail in Section 3.2. Another important method of this type is finite-element modelling (Smith, 1975).

The challenge of time-lapse modelling is the fast generation of synthetic seismograms. Usually, those seismograms have to be re-created several times for the complete seismic survey, possibly in 3-D. The most obvious solution would be to choose one of the standard modelling techniques and to do full simulations of seismic wave propagation for all configurations of interest. Generally, both the reservoir and the overburden (i.e., the geological layers above the reservoir) may have a fine and complex geological structure. Hence, accurate modelling of the complete elastic wave field is required and, typically, finite-difference modelling (FDM) would be the method of choice. Currently, FDM is probably the simulation tool that is most widely used for time-lapse modelling. Elements of FDM are also used as a part of many of the newly developed specialised time-lapse modelling techniques (Section 3.3).

Unfortunately, detailed FD calculations consume large amounts of computational resources. Consequently, the mere size of the problem makes time-lapse modelling a difficult task. A possible remedy is the new Born Repeat-Modelling technique (BRM) (Kirchner and Shapiro, 1998, 1999, 2000), which is described in the next chapter. In recent years, seismic time-lapse modelling has been an active area of research. Therefore, several other approaches have been proposed that are specially optimised for the purpose of time-lapse modelling of complex earth models. In Section 3.3, I review the basic principles of – from my point of view – BRM's most promising competitors.

3.1.2 Modelling reservoir changes

For a hydrocarbon reservoir under development, a detailed geological reservoir model is built. It integrates all available information, like seismic data, well logs, or production history of the field. By accumulating data over time, the reservoir description is continually updated and refined (Story et al., 2000; Huang et al., 1998; He et al., 1998; Sheriff, 1991a). The main purpose of such a reservoir model is to support development decisions, e.g., concerning well placement. For this, fluid transport is simulated in the reservoir model for possible production scenarios.

The reservoir model is also very important to test the feasibility of seismic surveys during production, especially for time-lapse application. For characteristic stages of the production process, an elastic model of the reservoir region is generated. With the help of relations from rock physics, the results of fluid flow simulation

are converted into elastic moduli or seismic velocities. Thus, a set of (at least two) elastic earth models is generated. (e.g. Johnston et al., 1998; Biondi et al., 1998). The number of earth models to examine might be quite large, if uncertainties lead to several possible geostatistical realisations for every time step.

Since geological conditions can extremely vary, rock physics description is usually based on correlation analysis of experimental data (e.g. Key et al., 1998) and rather simple analytical relationships obtained from specific rock models or effective-medium theories (Mavko et al., 1998; Schön, 1983). For example, Gassmann's equation (Eqn. 2.18) yields the change of (effective) bulk modulus caused by substitution of one pore fluid (e.g. oil) by another (e.g. water). According to Gassmann's relations, fluid substitution only modifies the bulk modulus, and thus affects P-waves but not S-waves. In Section 4.6, I make the same assumption when choosing a simple, physically motivated reservoir perturbation for the Marmousi model. Another interesting reservoir scenario is the opening or closing of fractures due to production-related alterations of pore pressure, which would affect anisotropy of both P-wave and S-wave propagation in reservoir rock (see Chapter 6, or Mavko et al., 1998).

3.2 Finite-Difference modelling

3.2.1 Importance of the finite-difference method

Finite-difference modelling (FDM) is an accurate tool for simulating wave propagation in heterogeneous media. Because of its great versatility, it is widely used to generate synthetic seismograms (e.g. Kelly et al., 1976). As the finite-difference approach is based on the elastodynamic wave equation (Eqn. 2.9) without physical approximations, this method accounts for all existing types of waves including repeatedly reflected and diffracted compressional waves, and all kinds of shear waves. Furthermore, FDM can account for fine details in seismograms caused by subsurface features at the scale of a wavelength, and even smaller. Disadvantages of FDM are phenomena like reflections from the borders of the model, and grid dispersion (see Section 3.2.5). Both effects can be suppressed by refining or extending the grid, which quickly increases computational cost.

Because of its qualities, FDM was chosen as a part of the Born Repeat-Modelling (BRM) algorithm. In the Green's function generation step, FDM is applied to compute the displacement field on a grid inside the reservoir (see Section 4.1). In addition, discrete differentiation with the help of finite-difference operators (as described in the following section) is used to compute the spatial derivatives of the Green's function.

3.2.2 Example of FD seismograms

Figure 3.1 shows a seismogram of the vertical component of the displacement field computed with FDM for the (unperturbed) Marmousi model (Figure 4.9). A detailed description of the model and the modelling parameters is given in Section 4.6. To reduce the data volume, a lateral spacing of 100m between traces was chosen. The fine structure of the Marmousi model gives rise to many scattered and reflected waves. Thus, the details seen in the seismogram cannot be achieved with asymptotic methods. FDM always has to simulate the complete wave propagation in the earth model to compute synthetic seismograms. Therefore, at least two full FDM calculations are necessary to model the result of a seismic time-lapse experiment.

In Figure 3.2, a seismic *difference* section can be seen, which was obtained by subtracting the results of two FD simulations made for different reservoir configurations. This figure illustrates the role of seismic modelling for survey planning in complex environments. Obviously, seismic receivers should be located beyond $x = 4300$m to measure the effects of reservoir changes in this shot gather. The field recorded by receivers closer to the source is confused by interaction with the overthrust formation located above the reservoir. The possibility to predict such effects makes seismic modelling very important for survey design.

Most of the energy carried by the "difference P-wave" travels from the reservoir to the surface in a narrow strip on the right of the steeply dipping layers. This can be seen in the *difference* snapshot of the wave field taken at $t = 1.2s$ that is depicted in Figure 3.3. Such pictures are created by subtracting the momentary displacement fields of two FD simulations performed for slightly different earth models. Difference snapshots can be very useful for interpretation because they show the origin of events in difference seismograms.

3.2.3 Discretisation of derivatives

The FD method approximates the continuous elastic medium by its properties on a grid and the derivatives of the wave field are computed with *(finite) differences* of its values at neighbouring grid locations. Usually, a regular rectangular grid is used, but other grid types are possible, as well.

The simplest possible finite-difference operators are obtained from Taylor expansions of the wave field at a neighbouring grid site in terms of the local displacement and its spatial derivatives. If Δx is the grid spacing on the x-axis, we obtain for an arbitrarily differentiable function $\mathbf{u}$:

$$\begin{aligned}\mathbf{u}(x+\Delta x, y, z, t) &= \mathbf{u}(x, y, z, t) + \Delta x\, \mathbf{u}'(x, y, z, t) + \tfrac{1}{2}\Delta x^2\, \mathbf{u}''(x, y, z, t) \\ &\quad + \tfrac{1}{3!}\Delta x^3\, \mathbf{u}'''(x, y, z, t) + O(\Delta x^3)\end{aligned} \tag{3.1}$$

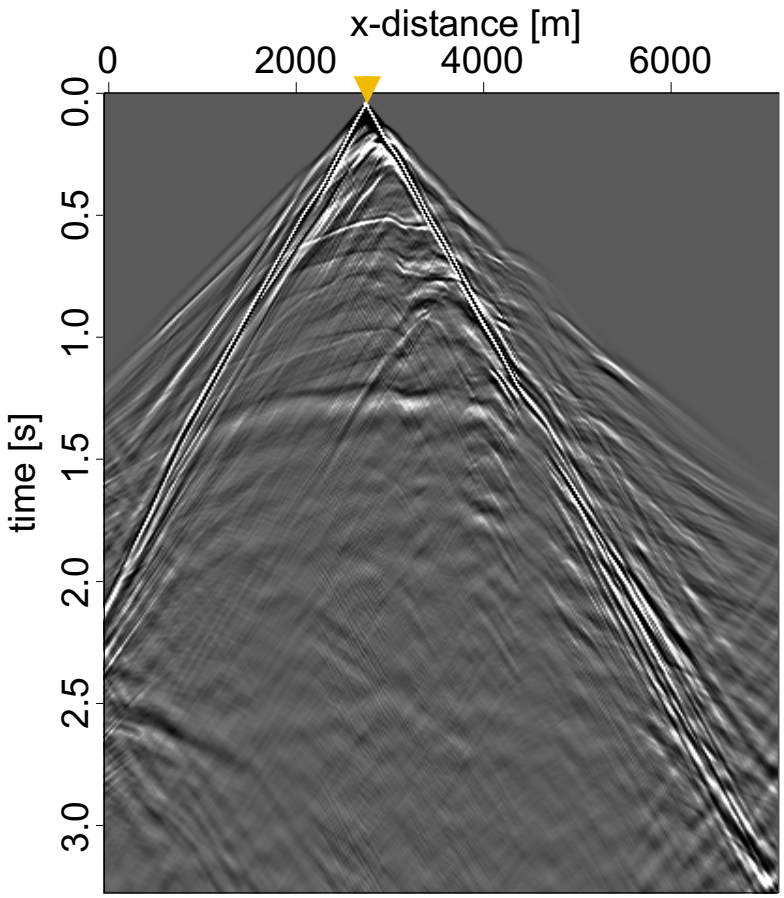

Figure 3.1: Example of a shot gather calculated with FDM for the Marmousi model shown in Figure 4.9. The source was located at $x = 2800$m and is indicated by a triangle. In this figure, high amplitudes of the vertical displacement component are shown as black (positive values) or white (negative values). In grey regions amplitudes are small.

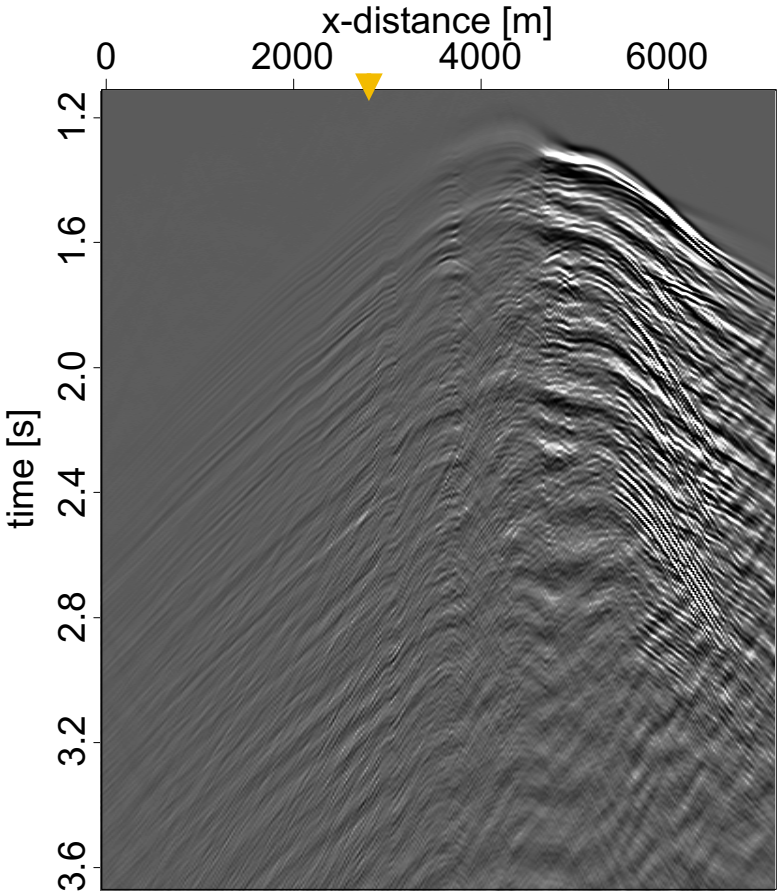

Figure 3.2: Difference seismogram calculated by subtracting the results of two FD simulations performed for the Marmousi model (Figure 4.9) with different reservoir configurations. The source location ($x = 2800$m) is indicated by a triangle. In this figure, high amplitudes of the vertical displacement component are shown as black (positive values) or white (negative values). In grey regions amplitudes are small.

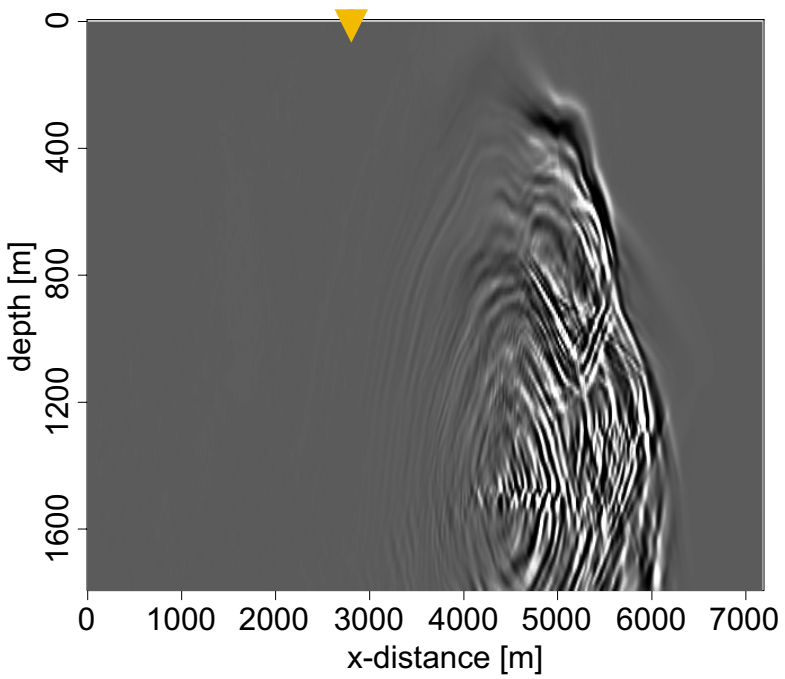

Figure 3.3: Difference snapshot of the vertical component of displacement in the sub-surface, calculated with FDM for the Marmousi model shown in Figure 4.9. The snapshot has been taken at $t = 1.2$s. The source point (at $x = 2800$m) is indicated by a triangle. In this figure, high amplitudes are shown as black (positive values) or white (negative values). In grey regions amplitudes are small.

$$\begin{aligned}\mathbf{u}(x-\Delta x,y,z,t) &= \mathbf{u}(x,y,z,t)-\Delta x\,\mathbf{u}'(x,y,z,t)+\tfrac{1}{2}\Delta x^2\,\mathbf{u}''(x,y,z,t)\\ &\quad -\tfrac{1}{3!}\Delta x^3\,\mathbf{u}'''(x,y,z,t)+O(\Delta x^3)\ .\end{aligned} \tag{3.2}$$

Here, $\mathbf{u}(x\pm\Delta x,y,z,t)$ and $\mathbf{u}(x,y,z,t)$ are values of the displacement field at grid locations (x,y,z,t) and $(x\pm\Delta x,y,z,t)$, respectively. Primes indicate (spatial) derivatives. $O(\Delta x^3)$ is one of the Landau-Symbols (Bronstein and Semendjajev, 1981), which replaces a function that goes to zero as quickly as its argument when $\Delta x\to 0$.

First adding, then subtracting these two equations yields approximate representations for the first and second derivatives of the wave field in x-direction:

$$\frac{\mathbf{u}(x+\Delta x,y,z,t)-\mathbf{u}(x-\Delta x,y,z,t)}{2\Delta x} = \mathbf{u}'(x,y,z,t)\ +\ O(\Delta x^3) \tag{3.3}$$

$$\begin{aligned}\frac{\mathbf{u}(x+\Delta x,y,z,t)-2\mathbf{u}(x,y,z,t)+\mathbf{u}(x-\Delta x,y,z,t)}{\Delta x^2} &= \mathbf{u}''(x,y,z,t)\\ &\quad +\ O(\Delta x^4)\ .\end{aligned} \tag{3.4}$$

The expressions on the left-hand sides of these equations are called second-order and third-order FD operators, respectively (applied to $\mathbf{u}$) because the former is exact up to second order in the grid spacing Δx, the latter to third order. As is shown in Figure 3.4, the tangent slope at a certain grid location x is approximated by the slope of the secant between neighbouring grid points.

Using field values at grid locations $(x\pm 2\Delta x,y,z,t)$, $(x\pm 3\Delta x,y,z,t)$, etc., higher-order error terms can be eliminated. The so-obtained finite-difference operators are accurate up to 4th, 6th, ... order in Δx. A similar discretisation is applied to the other spatial directions and for the time derivatives of the wave field (Levander, 1988; Kneib and Kerner, 1993).

In seismic modelling, staggered-grid finite-difference schemes are most popular (Madariaga, 1976; Virieux, 1984, 1986; Levander, 1988; Karrenbach, 1995). Here, the spatial derivatives are computed at inter-grid locations in the middle between the grid nodes:

$$\frac{\mathbf{u}\left(x+\frac{\Delta x}{2},y,z,t\right)-\mathbf{u}\left(x-\frac{\Delta x}{2},y,z,t\right)}{\Delta x} = \mathbf{u}'(x,y,z,t)\ +\ O\left(\left(\tfrac{\Delta x}{2}\right)^3\right)\ . \tag{3.5}$$

Effectively working with half of the grid spacing, a much higher accuracy is achieved (Figure 3.4). However, usage of inter-grid locations gives rise to serious difficulties: In a combination of staggered spatial derivatives along different coordinate axes, all grid locations of the field components, of the elastic moduli and of the density have to be defined consistently, which can cause stability problems in heterogeneous media (Gold et al., 1997; Saenger et al., 2000).

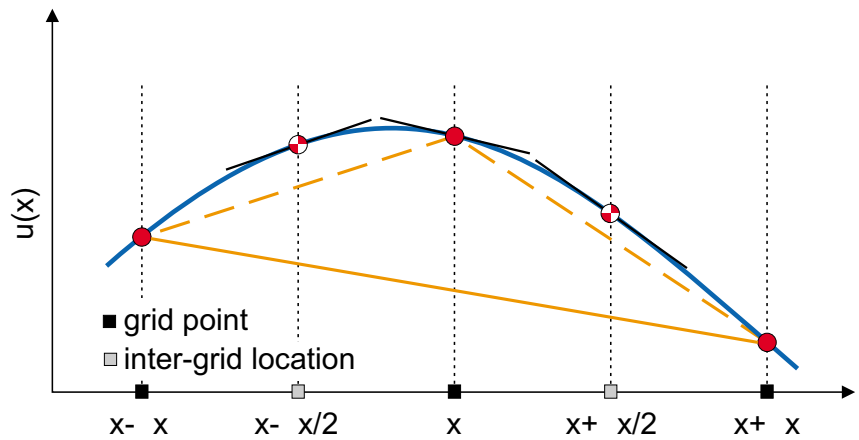

Figure 3.4: Discretisation of derivatives. The tangent slope at a certain grid location x is approximated by the slope of the secant between neighbouring grid points. The staggered grid scheme computes derivatives in the middle between grid nodes. Thus, effectively half of the grid spacing Δx is used for differentiation.

3.2.4 The time update

By using an operator like the one presented in Equation 3.4, the wave field at the grid point $\mathbf{r}$ and at time $t+\Delta t$ can be obtained from its previously computed values at time steps t and $t-\Delta t$, and from the second time derivative $\ddot{\mathbf{u}}$ at time t:

$$\mathbf{u}(\mathbf{r}, t+\Delta t) \quad = \quad 2\mathbf{u}(\mathbf{r}, t) - \mathbf{u}(\mathbf{r}, t-\Delta t) + \ddot{\mathbf{u}}(\mathbf{r}, t) \ . \tag{3.6}$$

The necessary – but yet unknown – values of the second time derivative are calculated from the elastodynamic wave equation (Eqn. 2.9) with the spatial derivatives replaced by their discrete counterparts according to Section 3.2.3:

$$\ddot{u}_i(\mathbf{r}, t) \quad = \quad \frac{1}{\rho(\mathbf{r})} \left[c_{ijkl}(\mathbf{r})\, u_{k,l}(\mathbf{r}, t) \right]_{,j} + f_i(\mathbf{r}, t) \ . \tag{3.7}$$

The above procedure is classified as explicit finite-difference scheme with second-order time update. Such FD schemes are very popular for seismic modelling because seismograms are computed efficiently with moderate requirement of computer memory. However, this way of computing the time update involves numerical instabilities if the sampling interval is too large (Section 3.2.5).

Most FD seismograms shown in this thesis have been computed with an explicit FD scheme with eighth order differentiation in space on a staggered grid and second order in time (Karrenbach, 1995). Recently, a new staggered-grid FD scheme has

been introduced (Gold et al., 1997; Gold, 1997; Saenger et al., 2000) that calculates spatial derivatives along grid diagonals. This FD scheme can compute the wave field near strong discontinuities with much less error. It is applied to simulate wave propagation in the model with a water layer presented in Section 5.3.

3.2.5 Restrictions of finite-difference modelling

The most important limitation of FDM is its large requirement of computer memory and CPU time. Thus, even with supercomputers FD simulations can be a challenge. Numerical errors caused by discretisation demand rather fine sampling. Especially the time step Δt has to be chosen usually a lot smaller than required by the sampling theorem (Eqn. 2.30) alone.

On the one hand, too coarse sampling can give rise to amplitude errors, which build up exponentially with time and cause numerical overflow. On the other hand, high-frequent waves sense the granularity of the (discrete) medium, and therefore propagate with another phase velocity than expected for the continuum. For both effects, the remedy is to choose finer sampling intervals according to grid-specific stability and dispersion conditions. The former effect can be completely avoided whereas the latter is a peculiarity of differentiation on a discrete grid.

By using a certain minimum number of grid points to discretise the longest wavelength present in the wave field, the velocity error can be reduced to an acceptable level. People often admit higher dispersion errors to keep computing times low, because CPU time for 2-D models quickly rises with about the third power of the inverse of the grid spacing. For 3-D models, the computing time increases even with the fourth power.

A good possibility to reduce numerical dispersion is the use of higher-order differentiation operators that take into account more than one neighbouring grid point at either side (Holberg, 1987; Levander, 1988; Kneib and Kerner, 1993). Thus, spatial and temporal grid size is reduced. However, even with high-order staggered-grid operators the number of grid points per wavelength will still be much greater than the two points that the sampling theorem demands. Since long operators will jut out at the borders of the earth model, they only make sense if the model is still much larger than the operator length. This may considerably influence the gain of computational resources of specialised time-lapse modelling techniques like FD-injection, or the hybrid modelling technique, which both involve FD modelling in a small subset of the earth model (see Sect. 3.3).

We normally want to use a finite grid in order to simulate wave propagation in an unbounded region of the earth. Therefore, reflections at the borders are considered as artifacts of the modelling scheme. The usual strategy is to simulate the infinite medium by extending the earth model with damping or absorbing boundaries at

all sides (see e.g. Clayton and Engquist, 1977). CPU time and storage is often considerably increased by large damping or absorbing boundaries because – as always with FDM – these boundaries must be thick to guarantee a reasonable quality of the modelling result. Again, boundary thickness will be a serious problem when wave propagation is simulated only on a small sub-grid. Then, badly suppressed boundary reflections will cause large errors, and the boundary volume may easily become larger than the medium itself.

Summarising the previous considerations, I conclude that the consumption of computational resources can be enormous, particularly if – like for the homogeneous earth models in Chapters 4 and 6 – a largely undisturbed wave field is desired.

3.3 Optimised approaches to time-lapse modelling

3.3.1 Special features of time-lapse models

The elastic earth models used to compute synthetic seismograms in a time-lapse study are very similar among each other. Usually, only the reservoir model is updated according to the results of fluid flow simulations. The biggest part of the model remains the same for all calculations because the elastic properties of the overburden are usually not affected by production. Conventional forward modelling algorithms do not make use of this fact. Thus, there is a great potential for optimisation.

A more refined modelling strategy must reduce this redundancy by finding an efficient way of propagating the waves up and down through the overburden without compromising too much the accuracy of the modelling inside the reservoir. Seismic time-lapse modelling is an active area of research and several specially optimised time-lapse modelling schemes have been proposed in recent years (Lecomte, 1996; Gjøystdal et al., 1998; Hokstad et al., 1998; Kirchner and Shapiro, 1998, 1999, 2000; Robertsson et al., 1999, 2000; Robertsson and Chapman, 1999, 2000; Mittet and Arntsen, 1998). At the Geophysical Institute, current research is being done by M. Riede and T. Hertweck on modelling by demigration (Santos et al., 1998; Hertweck, 2000). Their problem is similar but uses less heterogeneous media.

The common principle of all referred techniques (including BRM) is that repeated modelling of wave propagation for different configurations of the target zone are combined with Green's functions calculated once for a reference model to save computing time. These approaches differ in the choice of the modelling technique applied to obtain the Green's function data, and in the way they calculate the response of the target. This combination determines the accuracy and the type of earth model to which the respective technique can reasonably be applied. In the

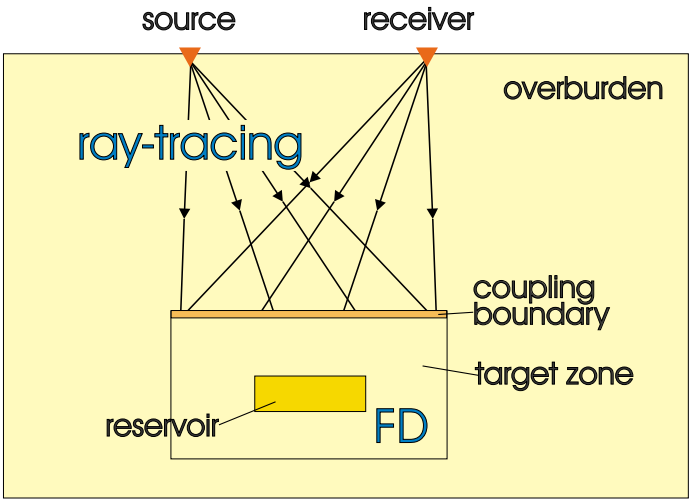

Figure 3.5: Domains of wave propagation of the hybrid modelling technique. Local FD simulations in a complex target zone are combined with efficient ray-tracing in the overburden. Solutions in both domains are connected in a narrow strip at the top of the target zone (Lecomte, 1996).

following, I explain details of two recently published methods that are closely related to BRM. They have been chosen because they appear to be particularly attractive for application to time-lapse modelling, and obviously usable implementations have already been developed.

3.3.2 The hybrid modelling technique by Lecomte et al.

Lecomte (1996), Hokstad et al. (1998), and Gjøystdal et al. (1998) propose a hybrid modelling scheme, which combines local FD simulations in a complex target with efficient ray-tracing techniques (as, e.g., described by Vinje et al., 1993) in the structurally much simpler overburden. According to the procedure, this defines two domains of wave propagation (see Figure 3.5) and requires special boundary conditions to connect the differently represented fields in the two domains (Mittet, 1994).

The hybrid modelling proceeds in three successive stages:

1. Calculation of the incident wave field by tracing rays from a given shot point to the top of the local finite-difference grid. In the acoustic case, this wave field is the pressure. In the elastic case all components of displacement *and* stress are required. The wave field is recorded in a narrow strip (at least three grid points thick for acoustic modelling) above the local FD grid.

2. Propagation of that field via FDM in the local complex reservoir structure. The incident field is introduced at the very top of the local FD grid and assumes the role of secondary sources of the wave field. Again, the scattered field is recorded in a narrow strip just below the secondary sources. The final result of the local FDM process is calculated by subtracting the recorded field and the incident field.

3. Extrapolation of the scattered field deduced from the second step towards the receivers using the representation theorem (Eqn. 2.23) or a similar relation. This type of expression is also often referred to as the Kirchhoff integral. The volume of integration in Equation 2.23 must contain all receivers and is bounded by the top of the local FD grid. Otherwise, it extends to infinity. To separate the incident field from the scattered field at the receivers, the volume integral is neglected. Thus, only the section of the surface integral coincident with the top of the FD grid contributes to the field at the receivers.

Extrapolation of the wave field in the third step requires knowledge of Green's function in the overburden, which must be computed in the same way as the incident field, by using the reciprocity principle (Eqn. 2.24) in addition. If sources and receivers occupy the same geographical locations, the Green's function may already exist from step 1. For time-lapse application, this method is very efficient because only steps 2 and 3 are repeated for all required reservoir models. The incident fields and Green's functions do not change and can therefore be re-used.

In a comparison of required CPU times presented by Gjøystdal et al. (1998), the 2-D acoustic implementation of the hybrid modelling technique required less than 1% of the time (including Green's function generation) of a pure FD scheme for the same earth model. This was achieved because the local FD grid is usually significantly smaller than the full earth model. In addition, it was possible to choose larger spatial and temporal sampling intervals, and a smaller number of time steps at the same level of accuracy.

A serious disadvantage of such a small FD grid are, however, always reflections from the boundaries (Lecomte, 1996, see also Sect. 3.2.5 of this thesis). Of course, the local FD grid should be chosen as small as possible to speed up computations. Then the boundaries will be very near to the reservoir and thus generate spurious events. Damping and absorbing boundaries may be added around the local grid to reduce this effect. Since effective reduction of boundary reflections requires a certain thickness of the extra boundaries, this may easily multiply the original size of the local FD grid and sometimes considerably reduce the savings.

3.3.3 FD-injection

In their interesting approach called FD-injection, Robertsson et al. (2000), and Robertsson and Chapman (2000) follow a three-step procedure very similar to the

one presented above. However, they use a more detailed Green's function for wave field extrapolation in the overburden. In contrast to the hybrid modelling, FDM is applied in both, the overburden and the inside of a small sub-volume containing the reservoir. This allows for fine detail and strongly scattering heterogeneities in all parts of the earth model, which extends the applicability of FD-injection to complex overburden models that cannot be treated appropriately with ray-tracing.

The incident wave field is introduced on a closed surface that surrounds the part of the reservoir where changes can happen. To reduce the effect of boundary reflections, the FDM sub-mesh is chosen (several times) larger than the actual volume of the reservoir. The scattered field is recorded on a plane horizontal surface that intersects the local FD grid. In their example, Robertsson and Chapman (2000) locate the output surface just in the middle between the reservoir and the top boundary of the sub-grid, and rather far away from both.

Again, the elastodynamic representation integral (Eqn. 2.23) is used to propagate the scattered field from the output surface to the receivers. For this, Green's function are required from all points of the output surface to all receivers. The Green's function is normally simulated with FDM using the reciprocity principle in the same way as described above for the hybrid modelling technique.

Since FD-injection is entirely based on FD calculations in all parts of the earth model, it has the potential to return very accurate solutions. It fully accounts for scattering of the wave field inside the FD sub-grid. Only when the scattered field interacts with the medium outside the FD sub-grid and propagates back into this sub-volume, errors with physical origin can occur.

As described for the hybrid modelling technique, reflections from the borders of the FD sub-grid can cause serious artifacts. This is probably the reason why in the published examples (Robertsson et al., 2000; Robertsson and Chapman, 2000) the FD sub-volume is chosen a lot larger than the region of model alterations, and a rather large distance is put between the output surface and the boundaries.

In a 2-D example with their elastic implementation (two traces are calculated), Robertsson and Chapman (2000) claim that they can compute the wave field at less than 7% of the CPU time of a full FD simulation for the same elastic earth model. The computational cost of the Green's function is not included. Robertsson et al. (2000) apply FD-injection integrated with a reservoir simulator in a large time-lapse study. Here, total computational savings of more than 98% are achieved by using a quasi-one-dimensional overburden model. The translation symmetry of the overburden extremely simplifies the generation of Green's functions. Only a small lateral inhomogeneity could increase computational effort by several times. Therefore, this study does not provide a realistic estimate of the computational efficiency for FD-injection.

3.3.4 Discussion

All these approaches have their specific advantages and disadvantages. Therefore, it is up to the user to choose the fastest modelling technique that meets the requirements of the problem he wants to solve. Among the presented methods, the hybrid modelling technique seems to be fastest for all cases in which it is applicable, whereas FD-injection probably covers the widest range of earth models. My approach, BRM, which is described in Chapter 4, is aimed at the situation in between: earth models with a complex geological structure in both the overburden and the reservoir, but with moderate reservoir perturbations.

Similarly to FD-injection, BRM uses finite-difference-simulated Green's functions to propagate the scattered field through the overburden. Such Green's function data can be obtained efficiently during a reference run of a seismic survey, if all receiver positions coincide with a source location. Otherwise efficiency will decrease. Since ray-tracing is usually a lot faster, such considerations are less critical for the hybrid modelling technique.

Wave propagation inside the target zone must be re-calculated for every reservoir model of interest. Therefore, this should be done in a particularly efficient way. Both, FD-injection and the hybrid modelling technique use FDM inside this region. However, because of boundary effects a rather big FD sub-volume ought to be chosen. In contrast, the perturbation calculations of BRM can really be restricted to the portion of the earth model where the properties actually change. Additionally, BRM in principle allows an even coarser discretisation of the wave field and of the earth model, which is only limited by the sampling theorem (Section 2.6). The computational effort for both approaches increases in about the same way with the volume of the sub-grid. Thus, perturbation calculations will probably require much less CPU time than the FD computations for the same reservoir. Since most production-induced variations of reservoir parameters are only small, I expect that BRM can be applied with great benefit.

Chapter 4

Born Repeat-Modelling

4.1 The BRM algorithm

As described at the beginning of the previous chapter, synthetic time-lapse seismograms are normally obtained by simulating wave propagation for a set of given earth models, which correspond to different stages of the production process. This is done to assess the detectability of production effects inside a reservoir.

In this chapter, I present an alternative approach to modelling of time-lapse seismograms, called Born-Repeat-Modelling (BRM). BRM combines FDM (see Section 3.2) with perturbation theory – namely Born approximation (Section 2.5) – to predict production-induced changes of the seismic response.

Especially if the change of reservoir properties is expected to be small and detectability is in doubt, the feasibility of a time-lapse survey has to be examined carefully, and probably a lot of effort will be spent on very detailed modelling. In such cases the validity of Born approximation will not be critical and BRM might be a promising alternative to established methods.

The procedure of BRM is illustrated with the flow chart in Figure 4.1. It consists of two steps:

Green's function generation: For the original earth model, i.e., the configuration before production, a reference survey is simulated using finite differences (or an equivalent technique). In addition to the seismograms registered near the receivers, the full wave field is recorded on a grid inside the reservoir. The reservoir grid must, of course, cover all points where the elastic parameters are modified. The data set recorded in this way is equivalent to the Green's function for the particular source configuration. It is required in order to compute the Born approximation in the following steps. With this strategy, scattering effects in the overburden are taken into account with FDM precision.

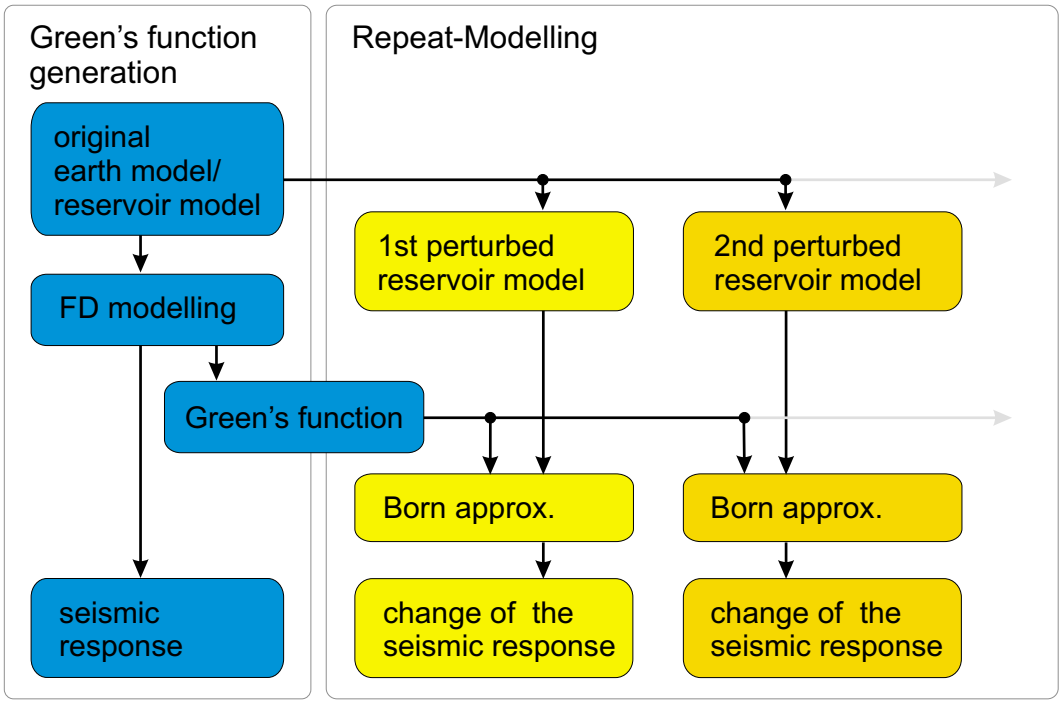

Figure 4.1: Flow chart to illustrate the procedure of Born Repeat-Modelling.

Repeat-Modelling: According to assumptions about production effects, a model of the elastic properties in the reservoir is defined for a certain time during production. With the Green's function data from the previous step, Born approximation is applied to compute production-induced changes of the seismic response.

The main part of the computational effort is spent during the first step, i.e., the-Green's function generation step. It is executed only once, whereas the Repeat--Modelling step is repeated for every desired reservoir configuration.

This approach is most useful, if seismograms are required for a large number of different reservoir configurations. In this case, BRM can save a large part of the CPU time, even in 2-D. For the Repeat-Modelling step, the gain in computing time increases with decreasing ratio of grid points in the reservoir and the total number of grid points. Thus, at most a few percent of the CPU time of the corresponding FD computation will be required. I expect that in 3-D this effect will be even larger than in 2-D.

4.2 Theoretical background

4.2.1 Simulating records of displacement or particle velocity

The standard way of generating synthetic time-lapse seismograms is to solve the wave equation numerically for a given survey geometry and a set of given elastic earth models characterised by the values of the stiffness tensor c_{ijkl} and the density ρ in all points $\mathbf{r}$. For numerical reasons, all BRM computations are actually done in frequency domain. In frequency domain the equation of motion for the components u_i of the displacement vector reads (see Section 2.3.1, or Aki and Richards, 1980):

$$\omega^2 \rho(\mathbf{r})\, u_i(\mathbf{r};\omega) + \left[c_{ijkl}(\mathbf{r})\, u_{k,l}(\mathbf{r};\omega)\right]_{,j} + f_i(\mathbf{r};\omega) \quad = \quad 0 \ . \tag{4.1}$$

Here, ω is the angular frequency and f_i is the ith component of an external force.

After a period of production, wave propagation will be governed by a similar differential equation with modified elastic properties:

$$\begin{aligned} \rho^{\mathrm{P}}(\mathbf{r}) &= \rho(\mathbf{r}) + \delta\rho(\mathbf{r}) \\ c^{\mathrm{P}}_{ijkl}(\mathbf{r}) &= c_{ijkl}(\mathbf{r}) + \delta c_{ijkl}(\mathbf{r}) \ . \end{aligned} \tag{4.2}$$

According to Section 2.5 (Eqn. 2.27), the solution for the perturbed model can be expressed as an integral equation in terms of the wave field in the unperturbed medium. By neglecting multiple scattering at the production-induced heterogeneities

$\delta\rho$ and δc_{ijkl}, we obtain the Born approximation of the wave field (Fourier transform of Eqn. 2.29):

$$\begin{aligned} u_i^{\mathrm{P}}(\mathbf{r};\omega) \;\approx\; & u_i(\mathbf{r};\omega) + \omega^2 \int_{\mathrm{res}} d^3r'\, G_{mi}\left(\mathbf{r}',\mathbf{r};\omega\right)\, \delta\rho\left(\mathbf{r}'\right) u_m\left(\mathbf{r}';\omega\right) \\ & + \int_{\mathrm{res}} d^3r'\, G_{mi,j}\left(\mathbf{r}',\mathbf{r};\omega\right)\, \delta c_{mjkl}\left(\mathbf{r}'\right) u_{k,l}\left(\mathbf{r}';\omega\right) \;. \end{aligned} \tag{4.3}$$

In Eqn. 4.3, I use the Green's function $G_{im}\left(\mathbf{r};\mathbf{r}';\omega\right)$, which is defined as the solution of Eqn. 4.1 for a point-source $f_{im}(\mathbf{r};\omega) = f(\omega)\delta(\mathbf{r}-\mathbf{r}')\delta_{im}$ located at the Point $\mathbf{r}'$ (see Section 2.4). Both integrations are over $\mathbf{r}'$. The volumes of integration must contain all points where the elastic properties are modified, typically the reservoir.

Eqn. 4.3 establishes the desired relationship between reservoir modifications and the change of the seismic response. It is valid for two as well as for three dimensions. Only the volumes of integration and the ranges for the indices have to be chosen appropriately. So far, no assumptions concerning medium symmetry had to be made. In principle, it is still possible to apply Eqn. 4.3, if reservoir properties become anisotropic, e.g., because of opening or closing cracks, etc. (Chapter 6; see also Mavko et al. (1998), section 2.4). In the common case of an isotropic medium Eqn. 4.3 becomes

$$\begin{aligned} u_i^{\mathrm{P}}(\mathbf{r};\omega) \;\approx\; & u_i(\mathbf{r};\omega) + \omega^2 \int_{\mathrm{res}} d^3r'\, G_{mi}\left(\mathbf{r}',\mathbf{r};\omega\right)\, \delta\rho\left(\mathbf{r}'\right) u_m\left(\mathbf{r}';\omega\right) \\ & + \int_{\mathrm{res}} d^3r'\, G_{mi,m}\left(\mathbf{r}',\mathbf{r};\omega\right)\, \delta\lambda\left(\mathbf{r}'\right) u_{k,k}\left(\mathbf{r}';\omega\right) \\ & + \int_{\mathrm{res}} d^3r'\, G_{mi,j}\left(\mathbf{r}',\mathbf{r};\omega\right)\, \delta\mu\left(\mathbf{r}'\right) \left(u_{m,j}\left(\mathbf{r}';\omega\right) + u_{j,m}\left(\mathbf{r}';\omega\right)\right) \;, \end{aligned} \tag{4.4}$$

with the Lamé parameters λ and μ. In the following, I will use the P-wave modulus $c_{11} = \lambda + 2\mu$ and the shear modulus $c_{55} = \mu$ in addition to the Lamé parameters, because via $v_{\mathrm{p}} = \sqrt{c_{11}/\rho}$ and $v_{\mathrm{s}} = \sqrt{c_{55}/\rho}$ they correspond more directly to the velocities. See Section 2.2.4 for details on the abbreviated notation for components of the stiffness tensor.

Eqn. 4.4 is the core of isotropic BRM. If the wave field is known in all points inside the reservoir from previous FD simulations, then Equation 4.4 can be used to compute quickly the change of the seismic wave field $\boldsymbol{\delta}\mathbf{u} = \mathbf{u}^{\mathrm{P}} - \mathbf{u}$ at the receiver for given perturbations of the elastic properties.

In the context of seismic monitoring the physical interpretation of these formulae is simple. The total displacement $u_i^{\mathrm{P}}(\mathbf{r};\omega)$ at the receiver is the sum of the wave field $u_i(\mathbf{r};\omega)$ scattered from the overburden and from the reservoir in its original configuration, plus the contribution of the newly introduced heterogeneities. In the integral kernels, $u_i(\mathbf{r};\omega)$ is the wave field incident on the reservoir. At the reservoir

point $\mathbf{r}'$, the perturbations $\delta\rho$ and δc_{ijkl} give rise to the scattered field, which is then transmitted to the receiver at $\mathbf{r}$ by the Green's function $G_{mi}\left(\mathbf{r}', \mathbf{r}; \omega\right)$. There is no term to account for two-fold or higher-order interaction with the production-induced reservoir changes. However, multiples generated by the overburden and by the unperturbed reservoir are already included in $u_i(\mathbf{r}; \omega)$.

With Eqn. 4.3, we can roughly understand the origin of the gain in computing time for the Repeat-Modelling step compared with an FD simulation. Dealing with arbitrarily heterogeneous models, both methods use a grid. For FDM, a time update must be computed for all grid points at every time step. However, the reservoir integration in Equation 4.4 is confined to a small subset of grid points. Consequently, the gain must increase linearly with decreasing ratio of grid points used by both techniques. For the simple 2-D model that I use in Section 4.4 the ratio of grid points was approximately 85 (see also Section 4.3.1, below).

4.2.2 Generation of Green's functions

Normally, seismic sources can be described as point-sources with frequency--dependent source signal $f(\omega)$. Particularly for zero-offset configuration, the Green's function G required for Eqn. 4.3 and Eqn. 4.4 is in fact very similar to the field u of the incident wave. The following expression applies if the source / receiver is located at $\mathbf{r}'$:

$$G_{im}\left(\mathbf{r}, \mathbf{r}'; \omega\right) \cdot f(\omega) = u_i(\mathbf{r}; \omega) \ . \tag{4.5}$$

$\mathbf{r}$ represents a point inside the target zone, and the index m describes the directivity of the source. The reciprocity relation (Eqn. 2.24)

$$G_{im}(\mathbf{r}', \mathbf{r}) = G_{mi}(\mathbf{r}, \mathbf{r}') \tag{4.6}$$

allows the interchange of source and receiver coordinates. Thus, I can easily calculate the Green's function with an FD simulation and subsequent deconvolution of the wave field with the known source wavelet $f(\omega)$.

For finite offsets the Green's function is obtained from an FD simulation with a point-source at the position of the receiver. Modelling whole surveys, a lot of effort can be saved by re-using the Green's function data several times.

BRM is particularly useful for zero-offset modelling, because then the incident wave and the Green's function coincide, which saves additional time in both, the Green's function generation step and the Repeat-Modelling step.

4.3 Applicability of BRM

4.3.1 Estimate of computational efficiency

In contrast to FDM, which always produces shot gathers, Born Repeat-Modelling (and most other techniques optimised for time-lapse modelling) is an inherently trace-oriented approach. Thus, the survey geometry substantially influences its performance and the gain of CPU time compared with, e.g., a pure FDM computation.

If N different reservoir configurations have to be tested in a time-lapse study, the amount of CPU time required by an FD solver would be

$$T_{\mathrm{FDM}} = N \cdot S \cdot t_{\mathrm{FDM}} \,. \tag{4.7}$$

Here, S stands for the number of shots in a survey, and t_{FDM} for the total CPU time required to simulate one shot using FDM.

The process of BRM consists of two steps. Therefore, the total computing time is the sum of contributions T_{G} from the Green's function generation step and T_{RM} from the Repeat-Modelling step:

$$\begin{aligned} T_{\mathrm{BRM}} &= T_{\mathrm{G}} + T_{\mathrm{RM}} \\ &= (S+R)\cdot t_{\mathrm{G}} + (S+R)\cdot(N-1)\cdot t_{\mathrm{RM}} \,. \end{aligned} \tag{4.8}$$

R is the number of receiver locations that do not coincide with a shot location of the survey. The symbols t_{G} and t_{RM} represent the time required for the basic BRM operations: t_{G} is the CPU time necessary to create the Green's function data for one shot location, and t_{RM} is the time required to simulate one trace with BRM.

Hence, I expect an improvement of the computational cost by a factor

$$\frac{T_{\mathrm{BRM}}}{T_{\mathrm{FDM}}} = \frac{1}{N}\cdot\frac{S+R}{S}\cdot\frac{t_{\mathrm{G}}}{t_{\mathrm{FDM}}} + \frac{N-1}{N}\cdot\frac{S+R}{S}\cdot\frac{t_{\mathrm{RM}}}{t_{\mathrm{FDM}}} \,. \tag{4.9}$$

The first term describes the effort necessary to generate the Green's function for the reference model. Since typically $\frac{S+R}{S}\cdot\frac{t_{\mathrm{G}}}{t_{\mathrm{FDM}}} \approx 1$, the first term will vanish for a large number N of simulations. The gain of computing time for the second and all further simulations is described by the second term in Eqn. 4.9. Normally, $\frac{N-1}{N}\cdot\frac{S+R}{S}$ is also of the order of magnitude of 1.

The computational efficiency is therefore mainly determined by the quotient $\frac{t_{\mathrm{RM}}}{t_{\mathrm{FDM}}}$, which is proportional to the ratio of the number of grid points in the reservoir V_{R}, and the total number of grid points in the earth model V:

$$\frac{t_{\mathrm{RM}}}{t_{\mathrm{FDM}}} = \alpha\cdot\frac{V_{\mathrm{R}}}{V} \,. \tag{4.10}$$

The factor α depends on the machines and implementations used. I expect that α will normally be of order 1, which is confirmed by timings made in my tests. Computer memory is usually not critical, because a large part of computations can be done sequentially.

4.3.2 Validity

For Born approximation to be valid, the modifications of the reservoir properties have to be small, which is usually the case in practice. Then scattering is weak, and thus the approximations made to obtain Eqn. 4.3 are justified.

In the past, a lot of authors have discussed the problem of accuracy and validity of Born approximation (see, e.g., Rytov et al., 1989; Keller, 1969; Wu, 1989; Habashy et al., 1993; Chapman and Coates, 1994). Conditions like "The scattered energy must be negligible compared to the incident energy." are frequently read. However, such conditions are often difficult to apply in practice. For a homogeneous background model with density ρ and stiffness components c_{11} and c_{55}, Hudson and Heritage (1981) consider a wave with minimum wavelength Λ incident on a scattering region of size d. Inside the scattering region the density and the stiffness components deviate by $\delta\rho(\mathbf{r})$ and $\delta c_{ii}(\mathbf{r})$ (with $i = 1$ or 5, no summation) from the homogeneous background medium. By estimating the magnitude of the neglected term they find the following condition (in my notation):

$$\eta \ll 1 \tag{4.11}$$

$$\text{with} \quad \eta := \left(\frac{d}{\Lambda}\right)^2 \sup_{\forall \mathbf{r}} \left(\frac{\delta\rho}{\rho}\right) + \left(\frac{d}{l}\right)^2 \sup_{\forall \mathbf{r}} \left(\frac{\delta c_{ii}}{c_{55}}\right) \tag{4.12}$$

and $l = \min(d, \Lambda)$. The above expression was originally derived for a 3-D problem. However, with a similar calculation I the same condition is found for 2-D. Hudson and Heritage admit that – owing to the generality of their derivation – Born approximation holds in many cases in which η is less or equal to 1.

The configuration examined by Hudson and Heritage is very similar to the situation in time-lapse seismics with the thickness of the reservoir substituted for the size d of the scatterer. I expect that in practice η will very often be close to 1, particularly if there are large perturbations of the P-wave modulus c_{11}.

To test the applicability and flexibility of Eqn. 4.11 in my case, I have performed a series of tests. A typical result will be discussed in Section 4.4.3 with an example. My results suggest indeed that BRM still works for values $\eta \approx 1$ and sometimes for even larger values. For practical application, I propose therefore to use the above condition in the form

$$\eta \leq 1 \tag{4.13}$$

as a guideline for the applicability of BRM.

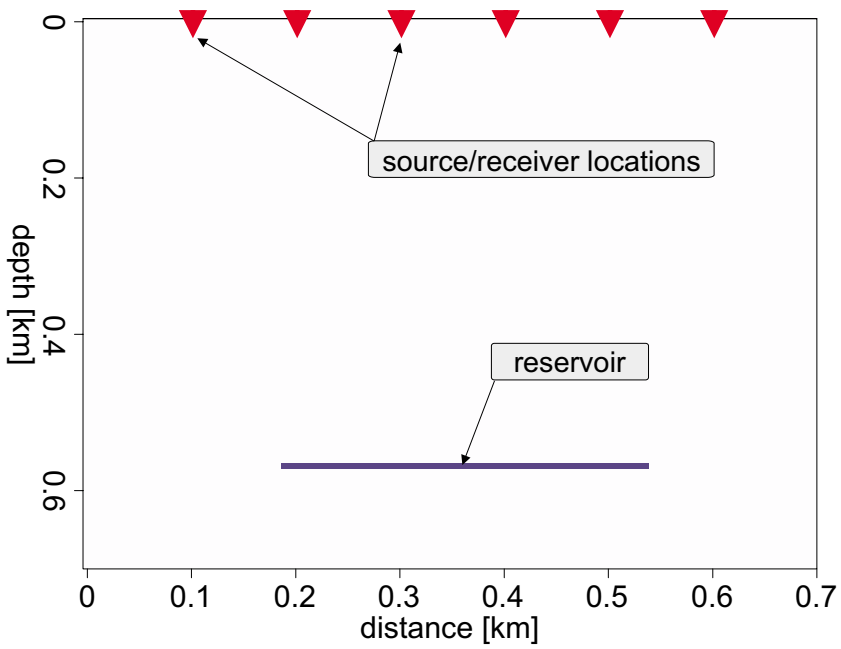

Figure 4.2: Simple 2-D earth model as described in Section 4.4.1. The triangles at the surface indicate source and receiver locations.

4.4 Application to a model with homogeneous overburden

4.4.1 Description of the model

In order to demonstrate the performance of BRM, I have applied this new technique to a very simple two-dimensional earth model (see Figure 4.2). I have chosen a 700m $\times$ 700m homogeneous block (grid spacing 2m) with seismic velocities $v_\mathrm{p} = 4000\frac{\mathrm{m}}{\mathrm{s}}$, $v_\mathrm{s} = 2236\frac{\mathrm{m}}{\mathrm{s}}$, and density $\rho = 2.0\frac{\mathrm{g}}{\mathrm{cm}^3}$. Inside a rectangular region near the bottom of the model the elastic parameters were perturbed to simulate the effect of production on a reservoir. The "reservoir" was chosen 16m thick and 360m wide. In this simple configuration, it is possible to observe clearly the effect of reservoir perturbations on the seismograms without being confused by waves scattered from the overburden.

4.4.2 Modelling results

For the source and receiver locations indicated in the figure with triangles, I have simulated a few seismic sections with different offsets. The source wavelet was

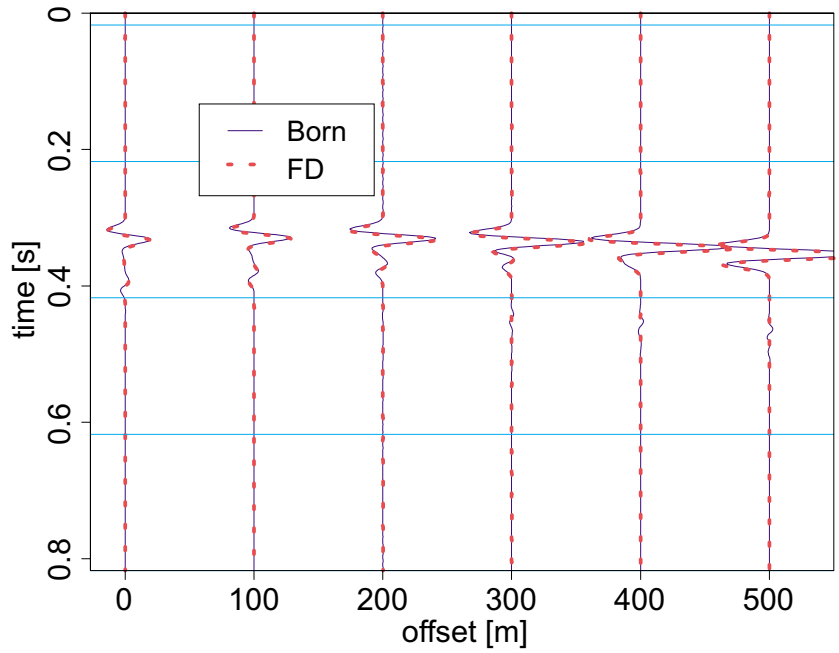

Figure 4.3: Difference seismograms for the model shown in Figure 4.2. Change of a shot gather that is caused by an increase of the P-wave modulus c_{11} by 5%. This is equivalent to an increase of the Lamé parameter λ by 13.3%. μ and ρ were kept constant. The source was located at $x = 100$m, and the leftmost trace is zero-offset.

the derivative of a Gaussian with a central frequency of 35Hz (sampling interval $\Delta t = 1.6$ms). The Green's function data required for BRM were obtained from FD simulations for the unperturbed block. A selection of my results is depicted in Figures 4.3 – 4.6. Since the effect is usually hard to observe directly in seismic sections, I always consider the *difference signal*, i.e., the change of the seismic response caused by a perturbation of reservoir properties.

Figures 4.3 – 4.5 offer the possibility to compare results of BRM with corresponding data obtained with FDM for different types of perturbation. To demonstrate the dependence on offset and position, I show a common-offset gather and a shot gather for the leftmost source location marked in Figure 4.2. The trace on the very left in the shot gather is zero-offset (see also Section 1.4 for illustrations of seismic recording geometries).

In Figure 4.3, results can be seen for perturbations of the P-wave modulus $c_{11} = \lambda + 2\mu$. In all points inside the reservoir, c_{11} was increased by 5%. This corresponds to a 13.3% increase of λ. The S-wave velocity and the density were kept constant. Since the wavelength is a little larger than the reservoir, this corresponds to $\eta \approx 0.15$ (compare Section 4.3.2). In these gathers, two real events are identified: Firstly, there is the reflected P-wave, which arrives at about $t \approx 0.3$s for small offsets. The

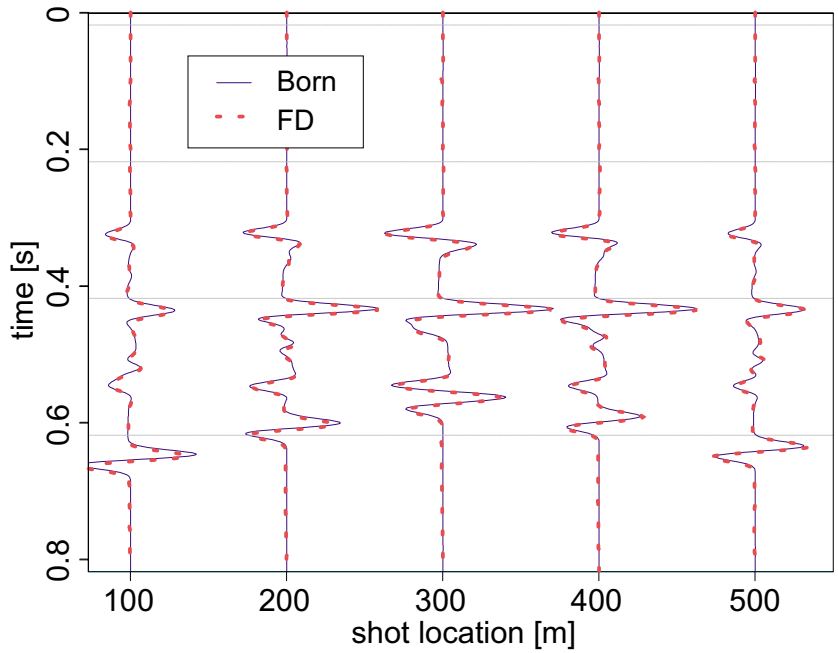

Figure 4.4: Difference seismograms for the model shown in Figure 4.2. A common-offset difference section is shown that was calculated for an increase of the shear modulus μ by 5%. The common offset is 100m.

second event (at $t \approx 0.38$s in the zero-offset trace) is the P-wave diffracted at the upper right corner of the reservoir. Both events approach each other when source and receiver are set at symmetrical positions. For larger offsets, at about $t \approx 0.43$s another "event" appears in the Born results of the shot gather. However, this is only a small artifact caused by the discrete computation of the (zero) divergence of the field of the S-wave.

Results of similar analyses are depicted in Figures 4.4 and 4.5. For Figure 4.4, the shear modulus $c_{55} = \mu$ was increased by 5%. c_{11} and ρ were left unchanged (i.e., $\eta \approx 0.05$). Perturbing μ affects both, P-wave and S-wave. Therefore, I expect both types of events to appear. The same is true for Figure 4.5, which shows difference traces due to 5% perturbation of the density ρ for constant elastic moduli. Since the wavelength was slightly larger than the reservoir thickness, validity is even less critical in this case.

By estimating travel times, quite a number of different events are found in those figures. In addition to the events seen in Figure 4.3, I identify the P- to S- converted wave at $t \approx 0.42$s in the leftmost traces of both sections. Then, at $t \approx 0.52$s, two overlapping events appear. The first one is the converted wave coming back from the upper right corner of the reservoir. The second one is the S-wave. The last event is the S-wave diffracted from the remote corner.

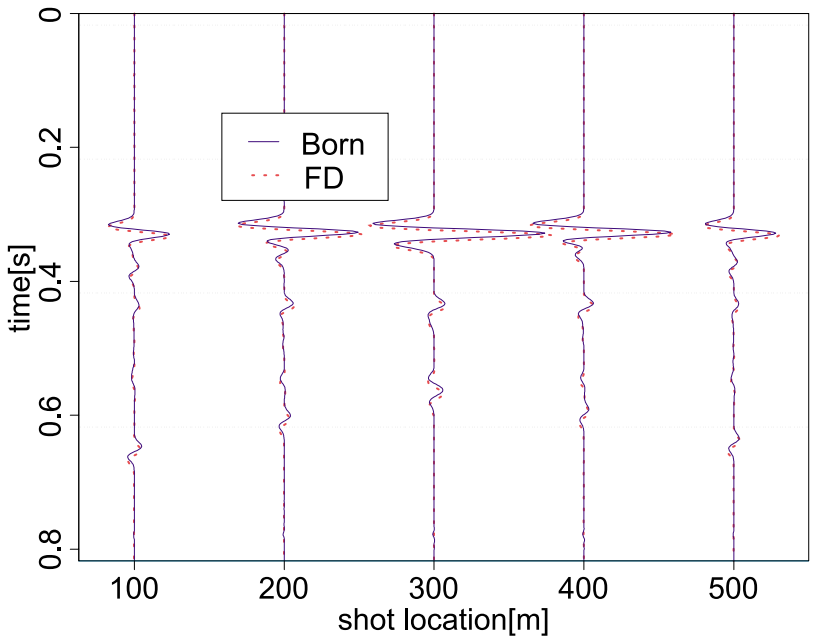

Figure 4.5: Common-offset difference section over the homogeneous earth model shown in Figure 4.2. I show the change of the seismic response for a 5% increase of the density ρ in the target zone. The common offset is 100m.

Obviously, in Figures 4.3, 4.4, and 4.5 the differently calculated traces coincide very well. By comparison with an established modelling tool, the BRM results have been confirmed for all offsets and source / receiver locations, for all possible kinds of moderate perturbations, and for all types of events. This approach is also fast. For example, to compute the data for Figure 4.3, BRM required less than 3% of the CPU time of the corresponding FDM calculations.

4.4.3 Behaviour for large perturbations

The question, in which cases a perturbation of the reservoir parameters can be considered small enough for Born approximation to be valid, is a critical issue. Therefore, I have tested very large perturbations of the elastic reservoir properties. Born approximation treats the contributions of the scattered wave field independently for all reservoir points. Consequently, multiple-scattering effects inside the reservoir are neglected. If the frequency and the perturbation are too big, multiple-scattering will start to become important and the agreement will decrease.

Figure 4.6 shows results for large perturbations of the P-wave modulus c_{11}. The traces have been obtained for offset 500m (shot at $x = 100$m, and receiver location $x = 600$m). This corresponds to the rightmost trace in the shot gather of Fig-

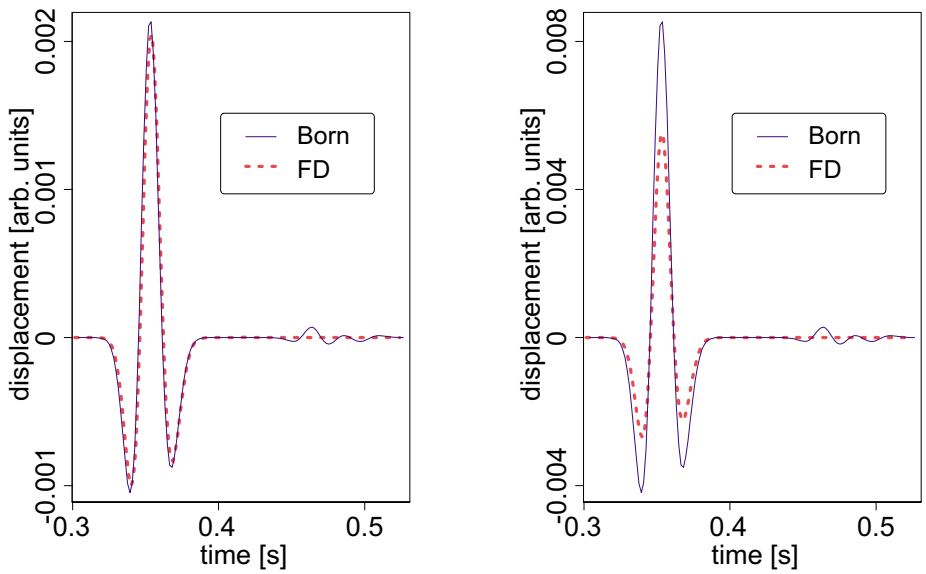

(a) $\delta c_{11}/c_{11} = 20\%$ **(b)** $\delta c_{11}/c_{11} = 80\%$

Figure 4.6: The change of a seismic trace (offset=500m) for different large perturbations of c_{11}.

ure 4.6(a). I have chosen $\delta c_{11}/c_{11} = 20\%$ for the graph on the left hand side, and $\delta c_{11}/c_{11} = 80\%$ on the right hand side. These values are equivalent to 53% and 213% perturbations of the Lamé parameter λ.

Apart from the small numerical artifacts at $t \approx 0.43$s, the curves on the left hand side match perfectly. In the picture on the right hand side, however, I observe a considerable discrepancy. This suggests that the range of validity was exceeded for the model used here. In practical situations, I hardly expect to encounter such large changes of reservoir properties.

In the first case (i.e., $\delta c_{11}/c_{11} = 20\%$), the value of η according to Eqn. 4.12 was 0.64, whereas for $\delta c_{11}/c_{11} = 80\%$ I find $\eta = 2.56$. This suggests that Born approximation was indeed sufficiently accurate up to a value of $\eta \approx 1$.

For the other reservoir parameters c_{55} and ρ, I have made similar tests with 20% and 80% perturbations. In all cases – even for 80% – I have observed a very good agreement between results of BRM and FDM.

4.5 3-D modelling with BRM

4.5.1 Importance of 3-D modelling

The simulation of seismic wave propagation in two-dimensional media can be very useful for theoretical investigations in order to develop or demonstrate new techniques. Especially in connection with the finite-difference method, 2-D modelling is still very popular.

For practical application wave propagation ought to be simulated in three-dimensions in order to obtain realistic seismic amplitudes (this should not be confused with 3-D data acquisition). The calculations considerably simplify for earth models with strict translational or rotational symmetry. In such cases a part of the calculation can be done analytically (e.g. Mittet and Arntsen, 1998). For more general earth models without special symmetries, a full 3-D computation is generally required.

Especially for the finite-difference modelling technique, three-dimensional calculations require huge amounts of computational resources, and a three-dimensional finite-difference simulation of a complete realistic seismic time-lapse survey is hardly possible at present. Optimised time-lapse modelling techniques like the ones described in Sections 3.3 and 4.1 have the potential to reduce the computation time by one or two orders of magnitude and might thus facilitate time-lapse modelling in 3-D.

An implementation of the BRM algorithm in 3-D has been developed. The aim of the following section is to provide a test of the feasibility of BRM computations in three dimensions. Thus, the potential usefulness of BRM for practial application is investigated.

4.5.2 Example

The earth model

To test BRM in 3-D, I use a homogeneous cubic earth model with size 3.2km$\times$3.2km$\times$3.2km with the elastic wave velocities $v_{\mathrm{P}} = 4500\frac{\mathrm{m}}{\mathrm{s}}$, $v_{\mathrm{S}} = 2500\frac{\mathrm{m}}{\mathrm{s}}$, and the density $\rho = 2.7\frac{\mathrm{g}}{\mathrm{cm}^3}$. A sketch of this model is shown in Figure 4.7. For computational reasons, waves are reflected at all outer surfaces of the cube. The reservoir is represented by an inclusion of size 400m$\times$400m$\times$60m, which is located near the centre of the model. Inside this inclusion the P-wave modulus was increased by 5% to simulate production effects.

At the source point, which is indicated by a cross in the sketch of the model (Figure 4.7), elastic waves were excited by a vertical force. The source wavelet has the shape of the derivative of a Gaussian function with central frequency $f_{\mathrm{c}} = 30\mathrm{Hz}$.

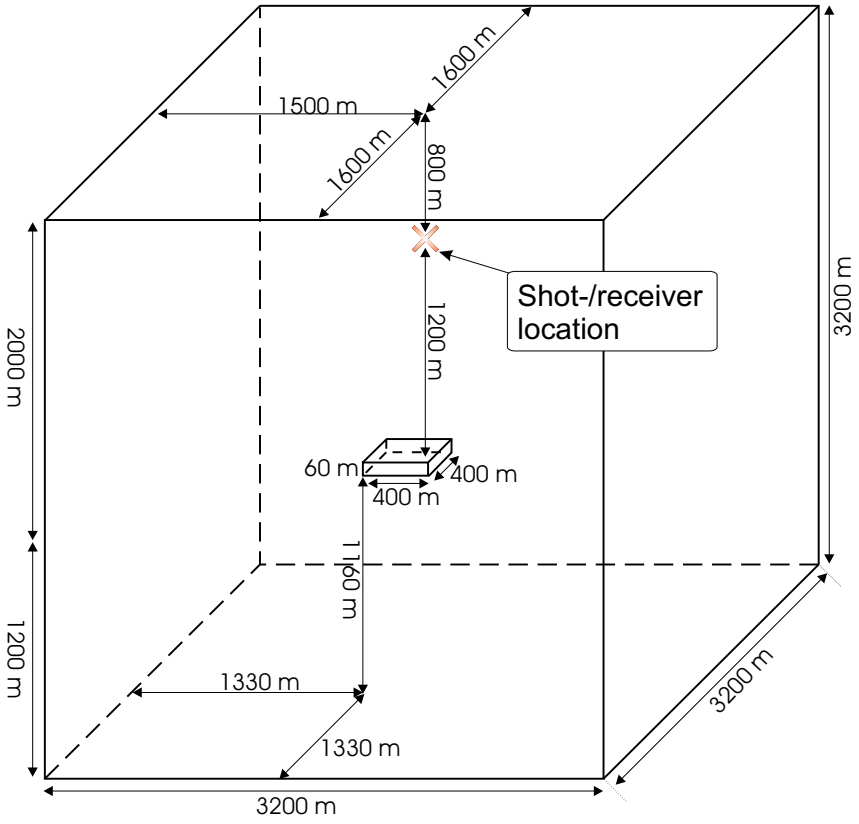

Figure 4.7: Sketch of the elastic earth model used to test BRM in 3-D.

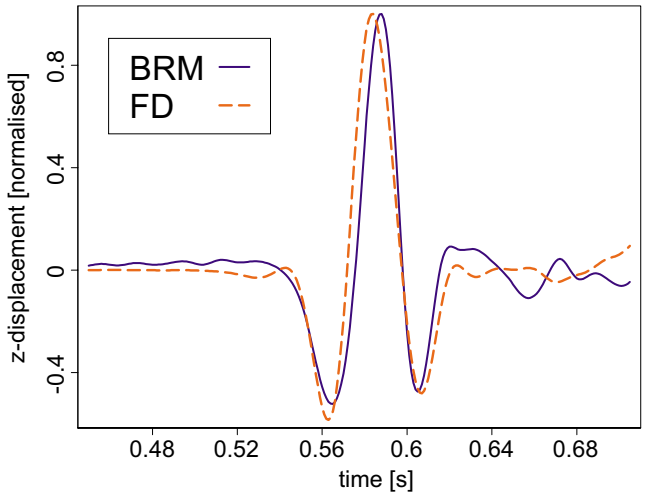

Figure 4.8: Zero-offset difference trace simulated for the 3-D model depicted in Figure 4.7. The source and the receiver were located at $x = 1500$m, 1200m above the target.

Modelling result

The change of the zero-offset trace was calculated with BRM. For comparison this trace was re-computed with FDM. Only one trace was modelled to save computational resources. All finite-difference computations were carried out with the FDM scheme described by Saenger et al. (2000) using the following parameters:

Grid spacing:	10m (all directions)
Sampling interval:	8ms (internal sampling interval: 1ms)
Recording length:	1024 time steps

The respective modelling results are plotted together in Figure 4.8. For comparison, both traces have been normalised because for the FDM implementation used the absolute pulse height was not exactly known.

The traces show one event that corresponds to the P-wave reflected from the target. There is a good agreement of the travel time and of the pulse shape between the results of both modelling techniques. In 3-D the energy of the source is distributed on a spherical surface. Therefore, the amplitudes of the scattered waves that make up the difference signal are much smaller than the displacement at the source. Both difference traces have been slightly smoothed. However, much numerical noise is still visible in the difference traces where the signal amplitude is small.

4.5.3 Computational aspects

The BRM trace shown in Figure 4.8 was computed within 53.1s (real time of the Repeat-Modelling step) on a HP C-160 workstation whereas the corresponding FDM calculation required about 10^6 seconds CPU time on a Cray T3E. The large ratio of computing times of approximately 0.005% is mainly due to the small relative size of the reservoir compared to the model volume: the fraction of grid points inside the inclusion is less than $1/3500$.

Compared with FDM, the memory requirements of BRM are small. However, about 84MB were required to store the Green's function data. This amount may be reduced by up to one order of magnitude by using spatial derivatives produced by the FDM program. This would allow to decrease the grid spacing to the limit given by the sampling theorem (see also Section 2.6 and Appendix A).

4.6 Test of BRM with an extremely complex overburden

4.6.1 Numerical setup for the Marmousi model.

For the previous example, I have chosen a homogeneous background model, because simple configurations permit to understand and check all details of the modelling result. Herewith, I have been able to develop the code and to demonstrate that the BRM algorithm works in principle. From the theoretical point of view, there are no restrictions regarding the complexity of the overburden: BRM takes into account the full overburden structure with the precision of FDM, which — e.g. compared with ray-based methods — is a great advantage. In order to investigate the relevance for practical application, a test with a heterogeneous sub-surface model is required, because realistic earth models may have a very complex overburden with thin, dipping layers and faults.

Time-lapse seismograms have been computed for an elastic earth model with extraordinarily complex sub-surface structure: From the two-dimensional Marmousi model, I have cut out an area of 7200m $\times$ 1800m with a grid spacing of 2m (see Figure 4.9). Assuming everywhere a constant ratio $v_p/v_s = \sqrt{3}$, an additional S-wave velocity model was derived.

From this "base model" the "time-lapse model" was created by modifying the values of the Lamé parameter λ inside the reservoir. This type of model alteration may arise when oil in a part of the reservoir is replaced by another fluid (see Section 2.3.5). For a test with a realistic earth model, it would not have been appropriate to change a rectangular area. To get a better approximation of production effects near a well, I assume a Gaussian profile for the modifications of the Lamé parameter λ. Starting with a maximum of $\delta\lambda/\lambda = 5\%$, the reservoir alteration falls below

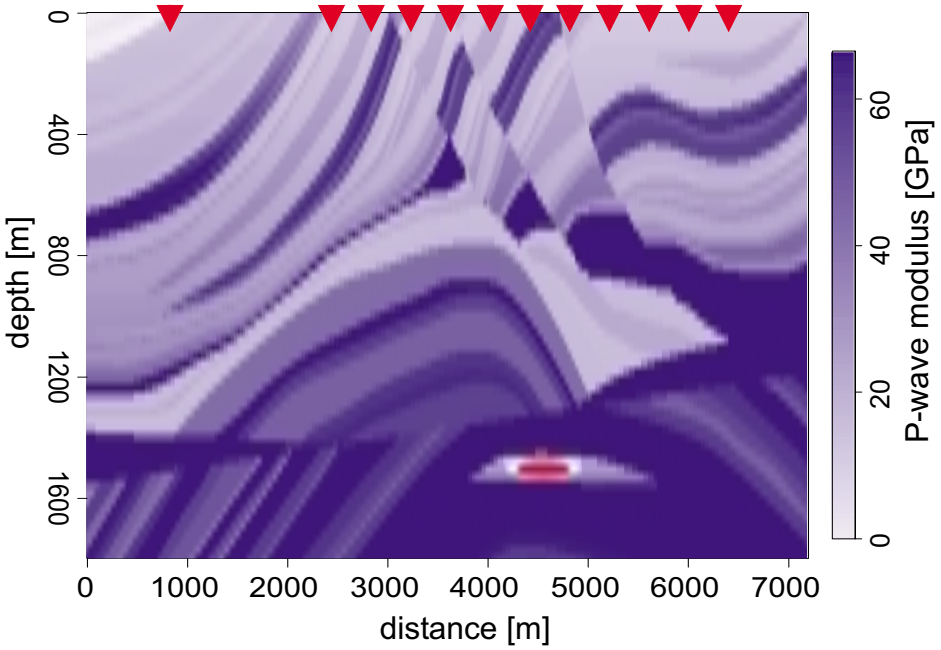

Figure 4.9: Marmousi-based elastic earth model used in Section 4.6. Here, the distribution of the P-wave modulus $c_{11} = \lambda + 2\mu$ is shown. The Lamé parameter λ was modified to simulate production effects near a well. The elliptically shaped spot inside the reservoir indicates the the region inside which the perturbation of λ was larger than 2.5%. Sources and receivers have been put up near the position of the triangles.

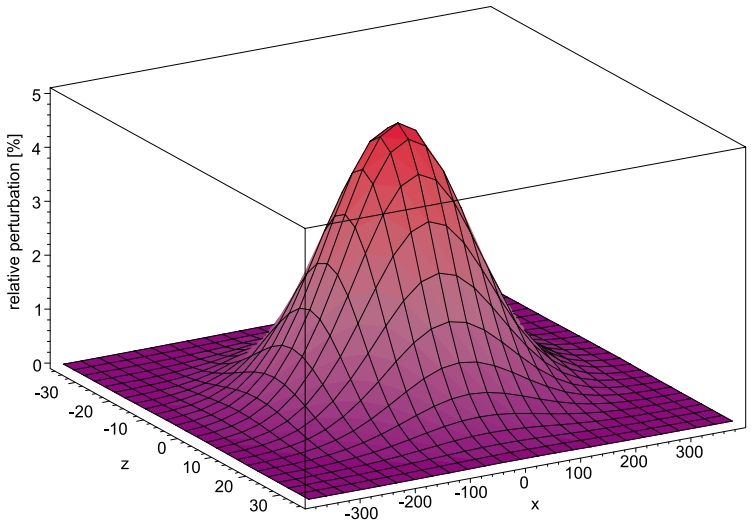

Figure 4.10: Profile of the reservoir perturbation used together with the Marmousi model (Figure 4.9). The vertical axis shows the relative perturbation as a function of distance from the centre of the reservoir. The maximum perturbation was 5%.

2.5% at distances of $\Delta x = 192$m and $\Delta z = 16$m in the respective directions. The shear modulus μ and the density ρ have not been changed. BRM computations have been restricted to an area of 768m $\times$64m centred around the perturbation maximum. Figure 4.10 visualises the perturbation profile. The (red) spot inside the reservoir in Figure 4.9 shows the area where these modifications took place. Triangles near the top of the elastic model indicate positions of sources or receivers used for at least one of the traces shown below. The seismic source was a vertical force, and the wave form used was the first derivative of a Gaussian with central frequency $f = 35$Hz sampled with $\Delta t = 1.6$ms. All receivers record the vertical component of particle displacement.

4.6.2 Modelling results and discussion

Owing to the complexity of the overburden, the traces recorded for the Marmousi model consist of a multitude of events. I investigate the quality of the difference seismograms obtained with BRM for varying source position and offset. Figures 4.11 and 4.12 show a shot gather with source location at $x = 2800$m near the surface, and a zero-offset gather, respectively. For comparison, results of BRM and FDM are always plotted together in the same diagram. Only a short time interval is shown in these sections to allow a detailed comparison of the amplitudes and the wave forms of FDM and BRM results. In both figures, there is a strong variation in amplitudes. This is evident from the few selected difference traces that

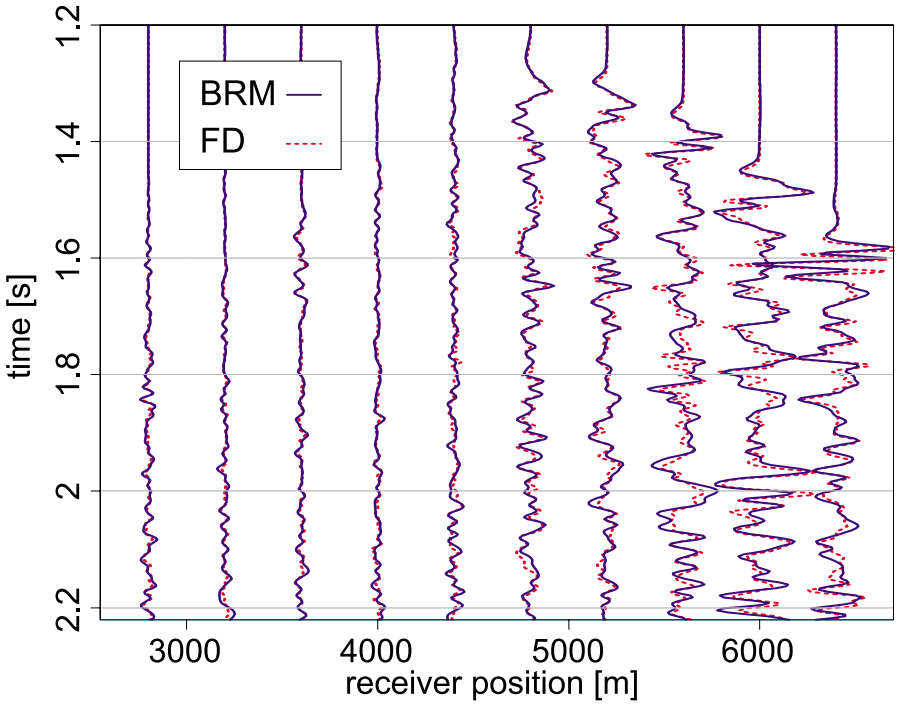

(a) Shot gather.

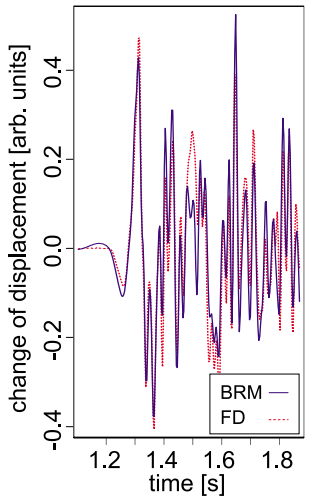

(b) Trace at $x = 4800$m.

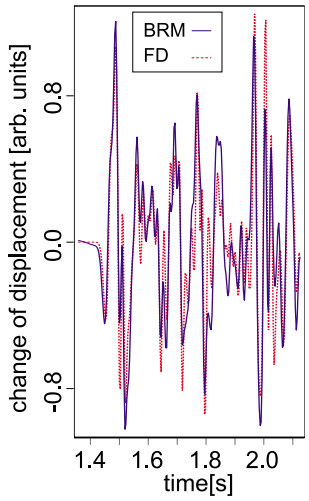

(c) Trace at $x = 6000$m.

Figure 4.11: Change of a shot gather calculated for the Marmousi model shown in Figure 4.9. The source was located at $x = 2800$m. The zero-offset trace is depicted in Figure 4.12(b).

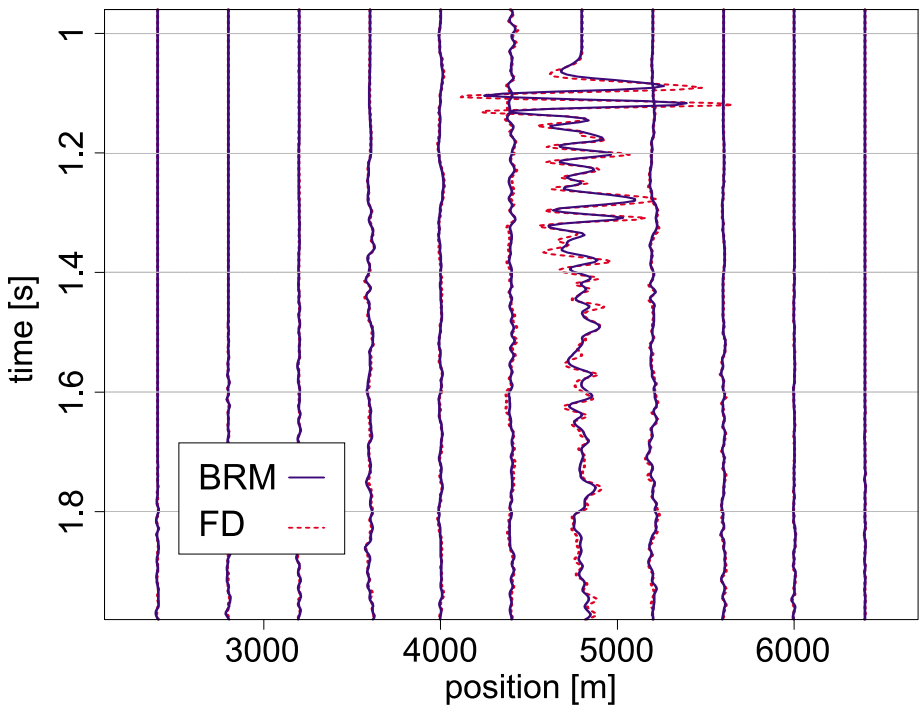

(a) Zero-offset gather.

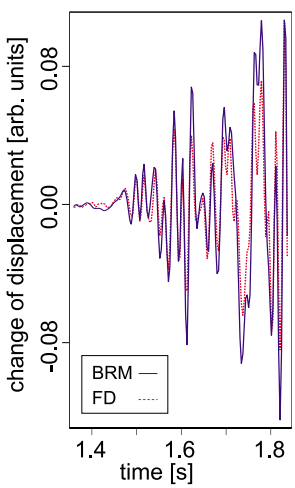

(b) Zero-offset trace at $x = 2800$m.

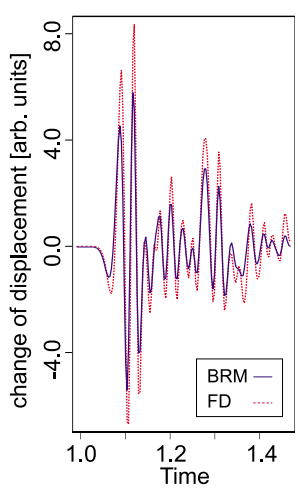

(c) Zero-offset trace at $x = 4800$m.

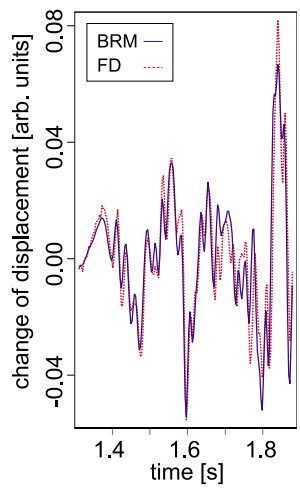

(d) Zero-offset trace at $x = 6000$m.

Figure 4.12: Change of a zero-offset gather calculated for the Marmousi model shown in Figure 4.9.

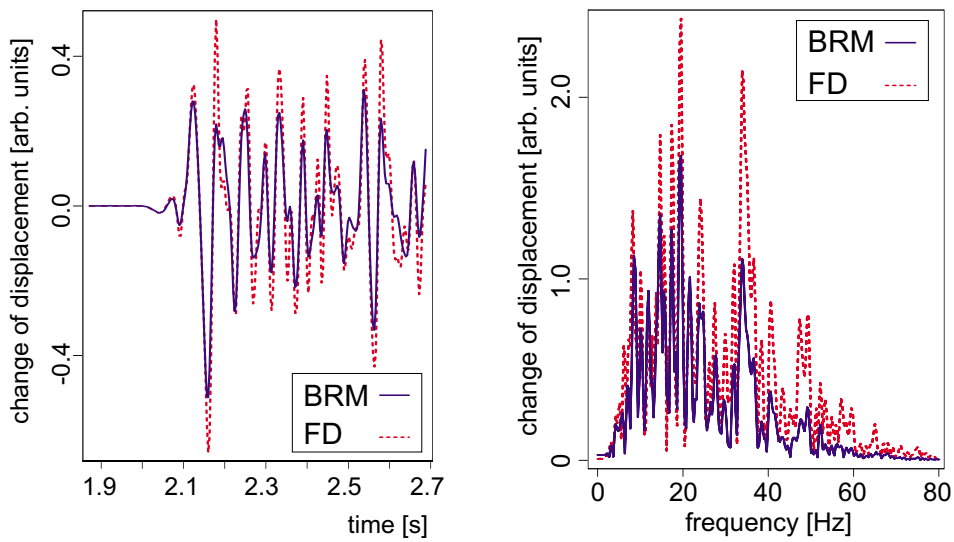

(a) Change of displacement. **(b)** Amplitude spectrum.

Figure 4.13: Far-offset difference trace obtained for the Marmousi model shown in Figure 4.9. The source was located at the surface at $x = 800$m, the receiver at $x = 6400$m.

have been plotted in separate diagrams for a quantitative comparison of the amplitudes. As already observed in Figure 3.2, the amplitudes of the difference shot gather increase significantly on the right of the fault zone. Especially, in the zero-offset gather (Figure 4.12), I observe a very quick change of the amplitude by two orders of magnitude. The apparent wavelength in the zero-offset trace corresponds to the P-wave travel time inside the perturbed region.

I cannot interpret all the events in these difference traces. It is only possible to compare the results of both modelling techniques. Obviously, there is an excellent agreement of travel times for all events and all offsets. The wave forms and amplitudes are not fully identical. However, there is a great similarity. Apparently, the wave forms mainly differ in small-scale features, whereas for all traces in these figures the large-scale or low-frequency structure is more or less the same for FDM and BRM. For the zero-offset trace at $x = 2800$m (Fig. 4.12(b)) I estimate $\eta \approx 0.6$ in Eqn. 4.13.

A difference trace corresponding to a very large offset can be seen in Figure 4.13(a). Here, the source was located near the surface at $x = 800$m, and the receiver at $x = 6400$m. Apparently, the predominant wavelength is much larger for this difference trace than for the zero-offset trace, because the travel path is considerably longer. For BRM this weakening of the high frequencies seems to be stronger than

geometry	BRM (avg.) [s]	FDM (avg.) [h]	ratio [%]
common-shot (10 traces)	780	99	0.22
zero-offset (11 traces)	560	1100	0.014
single trace	51	99	0.014

Table 4.1: Comparison of average computation times of BRM (Repeat-Modelling step) and FDM for different recording geometries. The times given are real CPU times including input/output activity (2 sigificant figures). Differences in CPU performance and clock rate are not taken into account.

for FDM. This is also evident from the amplitude spectra corresponding to these difference traces with the largest offset (Figure 4.13(b)). To a small degree, I can attribute this effect to tapers and band-pass filters that I use in the BRM algorithm to make the deconvolution of the wave field and the Fast Fourier Transform run stable (see Appendix A). The cause is very likely a peculiarity of Born Approximation: Eqn. 4.12 suggests that the accuracy of Born Approximation diminishes with decreasing ratio of wavelength and thickness of the target.

4.6.3 Computing time

The calculations for the Repeat-Modelling step for a zero-offset trace required less than one minute (real time) on a HP C-180 workstation, whereas the corresponding FDM trace took about 100 CPU hours on a Cray T3E (see Table 4.1). Differences in CPU performance are not taken into account. The reason for this big difference is, of course, the large ratio of grid points in the perturbed zone and the total number of grid points in the earth model. The single trace value is the average CPU time for separate computation of all eleven zero-offset traces. There are only very small fluctuations. The BRM time increases for finite offsets, because twice as much Green's function data must be loaded as for zero-offset. FDM can simulate one shot gather at a time, whereas the time required for BRM is proportional to the number of traces. The given computation times are real CPU times and thus include all required input/output activity.

Chapter 5

Modelling marine surveys

5.1 Importance of pressure seismograms

In the preceding chapters, I have demonstrated that BRM is a useful tool for modelling seismic time-lapse surveys. So far, I have only considered displacement seismograms, because the elastodynamic wave equation (Eqn. 2.9) suggests this. Of course, displacement seismograms are equivalent to records of particle velocity.

A large part of the industrial seismic surveys is carried out at sea. From the modelling point of view this means that the top layer of the sub-surface model will be water, and wave propagation in the fluid layer will be better characterised by the pressure field than with displacement or particle velocities. Pressure is also the quantity to which air guns and hydrophones couple. Consequently, there is the need for a possibility to model pressure seismograms efficiently together with elastic modelling of wave propagation in all the layers below. Of course, the following equation always permits the computation of the pressure field from the displacement field in any point $\mathbf{r}$ of the fluid layer (see also Section 2.3.4):

$$p(\mathbf{r}, t) = -\lambda(\mathbf{r})\, \nabla \mathbf{u}(\mathbf{r}, t)\ . \tag{5.1}$$

For BRM this would mean an enormous decline of performance, because it requires the both the computation and the numerical differentiation of all three components of the displacement vector. Instead, I chose to look for a concurrent modification of the equation of motion (Eqn. 4.1) and the BRM equation (Eqn. 4.3) to integrate acoustic and elastic modelling in the different parts of the earth model with optimum use of the power of BRM. The generalisation of the BRM equation (Eqn. 4.3) from displacement to pressure seismograms is not straightforward. Nevertheless, I have found an elegant way to incorporate a pressure source and pressure receivers into the BRM algorithm. A detailed derivation is given in the following section. With this result I can simulate marine seismograms with the same numerical effort as required for displacement modelling.

5.2 Derivation of the pressure modelling equation

In the last section I have already mentioned that it is always possible to compute the pressure at a certain point from the displacement field in its vicinity. I apply Eqn. 5.1 to the change of the displacement seismograms according to Eqn. 4.3:

$$\begin{aligned}\delta p(\mathbf{r};\omega) &= -\lambda(\mathbf{r})\frac{\partial}{\partial r_n}\delta u_n(\mathbf{r};\omega) \\ &= \iiint d^3r' \left(-\lambda(\mathbf{r})\right)\frac{\partial G_{nm}(\mathbf{r},\mathbf{r}';\omega)}{\partial r_n} \\ &\quad \cdot \left[\left(\delta c_{mijkl}\left(\mathbf{r}'\right) u_{k,l}(\mathbf{r}';\omega)\right)_{,j} + \omega^2\rho(\mathbf{r})u_m(\mathbf{r}';\omega)\right] \quad . \end{aligned} \tag{5.2}$$

In the integral kernel only the Green's function $G(\mathbf{r},\mathbf{r}';\omega)$ depends on the position $\mathbf{r}$ of the receiver. Therefore, all other quantities are not affected by the divergence operator. In Eqn. 4.3 the Green's function is responsible for the propagation of the scattered wave to the receiver. Here, the "pseudo-Green's function" $g_m(\mathbf{r},\mathbf{r}';\omega)$ with

$$g_m(\mathbf{r},\mathbf{r}';\omega) = -\lambda(\mathbf{r})\,\frac{\partial G_{nm}(\mathbf{r},\mathbf{r}';\omega)}{\partial r_n} \tag{5.3}$$

seems to fulfil the same task for the pressure field. In summary, we may re-write Eqn. 5.2 in the following form:

$$\begin{aligned}\delta p(\mathbf{r};\omega) &= \iiint d^3r' g_m(\mathbf{r},\mathbf{r}';\omega)\Big[\left(\delta c_{mijkl}\left(\mathbf{r}'\right) u_{k,l}(\mathbf{r}';\omega)\right)_{,j} \\ &\quad + \omega^2\rho(\mathbf{r})u_m(\mathbf{r}';\omega)\Big] \quad . \end{aligned} \tag{5.4}$$

According to Eqn. 5.4, it is possible – at least in principle – to calculate pressure seismograms with the BRM implementation that has so far been used for displacement seismograms. Still, there is the problem of finding an efficient way to obtain $g_m(\mathbf{r},\mathbf{r}';\omega)$. Eqn. 5.3 seems to necessitate enormous numerical effort. To obtain the spatial derivatives required for the divergence, the values of all nine components of $G(\mathbf{r},\mathbf{r}';\omega)$ must be computed in at least three (2-D) or four points (3-D) near the receiver. Of course, such a procedure would never be practicable for production.

The strategy is to modify the elastodynamic wave equation (Eqn. 4.1) in order to obtain a differential equation for $g_m(\mathbf{r},\mathbf{r}';\omega)$. This would permit the computation of all necessary information about this function with a single run of a finite-difference scheme.

As mentioned in Section 4.2 of the previous chapter, the Green's function $G(\mathbf{r},\mathbf{r}';\omega)$ is a special solution of Eqn. 4.1. It corresponds to a wave generated by an impulsive force applied at the point $\mathbf{r}'$:

$$L_{ik}(\mathbf{r};\omega)\,G_{km}(\mathbf{r},\mathbf{r}';\omega) + \delta_{im}\delta(\mathbf{r}-\mathbf{r}') = 0 \tag{5.5}$$

with the abbreviation

$$L_{ik}(\mathbf{r};\omega) = \delta_{ik}\,\omega^2\rho(\mathbf{r}) + \frac{\partial}{\partial r_j}\,c_{ijkl}(\mathbf{r})\frac{\partial}{\partial r_l}\ . \tag{5.6}$$

I compute the divergence on both sides of Eqn. 5.5 and subsequently multiply by $-\lambda(\mathbf{r})$. This yields:

$$L_{ik}(\mathbf{r};\omega)\left(-\lambda(\mathbf{r})\frac{\partial}{\partial r'_m}G_{km}(\mathbf{r},\mathbf{r}';\omega)\right) - \lambda(\mathbf{r})\frac{\partial}{\partial r'_m}\delta_{im}\delta(\mathbf{r}-\mathbf{r}') = 0\ . \tag{5.7}$$

L_{ik} and the divergence operator have been commuted, because they affect different coordinate vectors.

The expression in brackets is very similar to $g_m(\mathbf{r},\mathbf{r}';\omega)$. Taking into account the reciprocity theorem (Eqn. 2.24), which allows the exchange of arguments of the Green's function of the elastodynamic wave equation, I find that they are in fact identical. In addition, I apply the following relation:

$$\frac{\partial}{\partial r_m}\delta(\mathbf{r}-\mathbf{r}') = \frac{\partial}{\partial r'_m}\delta(\mathbf{r}-\mathbf{r}')\ . \tag{5.8}$$

This relation holds, because the Delta-function only depends on the difference of $\mathbf{r}$ and $\mathbf{r}'$, but not on either one of these variables individually. Thus, I can write

$$L_{ik}(\mathbf{r};\omega)g_k(\mathbf{r},\mathbf{r}';\omega) - \lambda(\mathbf{r}')\frac{\partial}{\partial r_i}\delta(\mathbf{r}-\mathbf{r}') = 0\ . \tag{5.9}$$

With this, the differential equation for the "pseudo-Green's function" $g_k(\mathbf{r},\mathbf{r}';\omega)$ is found. The body force distribution equivalent to a pressure source is the negative gradient of the pressure field (see Section 2.3.4):

$$f_i(\mathbf{r};\omega) = -p(\omega)\frac{\partial}{\partial r_i}\delta(\mathbf{r}-\mathbf{r}')\ . \tag{5.10}$$

Accordingly, Eqn. 5.9 can be interpreted as the elastodynamic wave equation that determines the displacement field $g_m(\mathbf{r},\mathbf{r}';\omega)$ caused by the pressure distribution $P(\mathbf{r},\omega)$ around the source point $\mathbf{r}'$ with

$$P(\mathbf{r};\omega\,|\,\mathbf{r}') = \lambda(\mathbf{r}')\delta(\mathbf{r}-\mathbf{r}')\ . \tag{5.11}$$

These results show how to compute $g_m(\mathbf{r},\mathbf{r}';\omega)$ with a standard FD scheme that comprises an implementation of a pressure point-source: Simply place a pressure source at the desired receiver location and register the displacement field on a grid inside the reservoir. Subsequently, multiply the result with the value of the Lamé

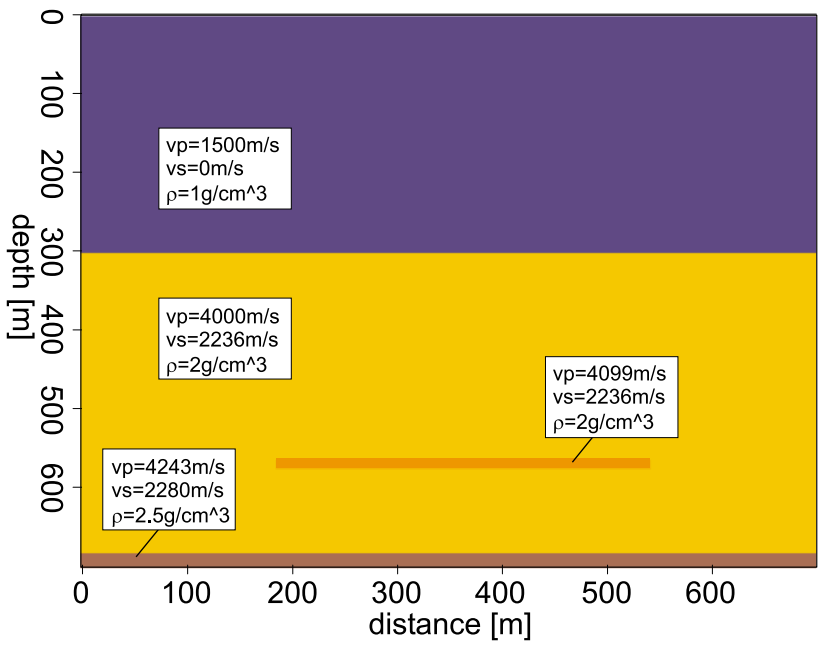

Figure 5.1: Simple earth model with a water layer.

parameter λ at the receiver. In practical situations this will very likely be the λ of water (2.25GPa).

Of course, the field obtained with the above algorithm is appropriate for both the incident wave and the "pseudo-Green's function" $g_m(\mathbf{r}, \mathbf{r}'; \omega)$. Consequently, marine surveys can not only be simulated with the same BRM and FDM algorithms and software used for displacement seismograms (i.e. land surveys) but this can also be done with equally small computational effort.

5.3 Example: Model with a water layer

5.3.1 Description of the model

The principle of pressure modelling with BRM is new and different from displacement modelling. Consequently, a test of its basic features is required. I have simulated the change of two representative seismic traces in consequence of modifications of the simple 700m $\times$ 700m subsurface model shown in Figure 5.1. The earth model used consists of three layers:

1. The top layer has the elastic properties of water: $v_\mathrm{p} = 1500\frac{\mathrm{m}}{\mathrm{s}}$, $v_\mathrm{s} = 0\frac{\mathrm{m}}{\mathrm{s}}$, and $\rho = 1\frac{\mathrm{g}}{\mathrm{cm}^3}$.

2. The second layer is fully elastic with $v_\mathrm{p} = 4000\frac{\mathrm{m}}{\mathrm{s}}$, $v_\mathrm{s} = 2236\frac{\mathrm{m}}{\mathrm{s}}$, and $\rho = 2\frac{\mathrm{g}}{\mathrm{cm}^3}$. In this layer is a rectangular target zone (360m $\times$ 16m) is located where the P-wave modulus $c_{11} = \lambda + 2\mu$, the shear modulus $c_{55} = \mu$, and the density ρ have been changed by 5%, respectively, to simulate a developing reservoir. The figure shows the case of modified c_{11}.

3. In the bottom layer the elastic properties are $v_\mathrm{p} = 4242\frac{\mathrm{m}}{\mathrm{s}}$, $v_\mathrm{s} = 2194\frac{\mathrm{m}}{\mathrm{s}}$, and $\rho = 2.7\frac{\mathrm{g}}{\mathrm{cm}^3}$.

The bottom layer was introduced in order to test to what extent BRM can predict time shifts of reflections from horizons below the reservoir caused by velocity changes inside this reservoir. The Green's function data set that is necessary for BRM was obtained with the unperturbed model.

In all numerical experiments the pressure point-source was located near the surface at $x = 100$m on the left of the model. Again, I use the derivative of a Gaussian with central frequency 35Hz as source wavelet. But now, the values are interpreted as applied pressure, and not as magnitude of an external force.

All FD calculations for the above earth model have been performed with a modified finite-difference scheme described by Saenger et al. (2000). Compared to a standard FDM technique, this yields much higher accuracy of the wave field near the interface between layers 1 and 2 with its high contrast in S-wave velocity.

5.3.2 Modelling results

The pressure field was recorded at two points indicated by red triangles in Figure 5.1. One receiver was located near the source, another in the right part of the model with 500m distance to the source.

Figure 5.2 shows the change of two pressure traces due to a 5% increase of the P-wave modulus c_{11}. As in Example 1, $\eta \approx 0.15$. For comparison, the results of BRM and the corresponding FDM results are plotted together in the same figure. In Figure 5.2(a), the zero-offset difference traces can be seen.

I classify the events by rough estimates of the possible travel times along rays. The first event (at $t \approx 0.53$s) is the P-wave diffracted from the upper left corner of the target. After approximately 0.67s the diffraction from the remote corner arrives. The two other events are identified as waves reflected from the boundary between layer 2 and layer 3 before or after interacting with the reservoir. The event at $t \approx 0.6$s corresponds to a wave that has travelled from the source to the left of the reservoir, then to the interface below, and finally back to the source / receiver. A similar travel path can be constructed for a wave that is diffracted at the right-hand side of the target. The corresponding travel time is $t \approx 0.74$s.

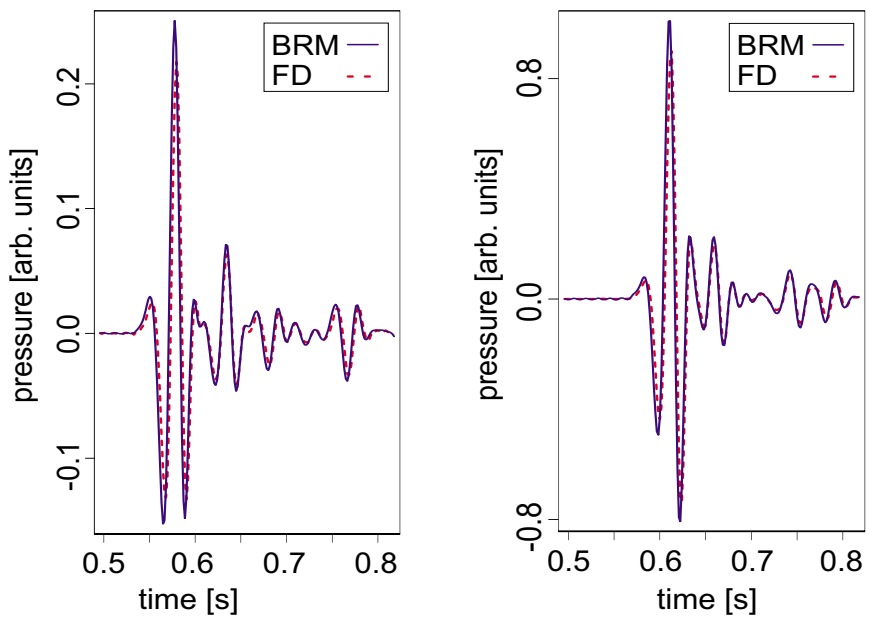

(a) **(b)**

Figure 5.2: Change of seismic (pressure) traces due to a 5% increase of the *P-wave modulus* c_{11} inside the target zone of the earth model in Figure 5.1.
(a) Zero-offset trace recorded near the surface at $x = 100$m.
(b) Offset 500m. The source was at $x = 100$m, the receiver at $x = 600$m.

The same types of events can be found in the 500m-offset difference traces depicted in Figure 5.2(b). Like the zero-offset traces, the first arrivals are the waves coming directly from the reservoir (both at $t \approx 0.57$s). The waves taking the detour via the interface below the reservoir arrive after $t \approx 0.71$s. Because of the model's symmetry, reflections and diffractions from both sides of the target arrive with a very small delay. Consequently, they are hard to discriminate.

I have carried out similar tests for small modifications of the shear modulus μ and of the density ρ inside the reservoir. For a comparison of BRM and FDM, traces with offset 0m and 500m are shown in Figures 5.3 and 5.4. These figures are interpreted similarly to the discussion above. Of course, this time the reservoir scatters all types of waves, and I expect that P-wave and S-wave events appear in the difference traces.

5.3.3 Discussion

For all numerical experiments presented in the current chapter the results obtained with BRM and FDM agree excellently. The travel times, the wave forms, and the signal amplitudes are virtually equal for the difference traces simulated with both techniques. Thus, I conclude that the extension of BRM to modelling of pressure seismograms is feasible, and its perfomance is as good as for displacement modelling.

This applies not only to events caused by waves reflected directly from the target. It was also possible to reproduce events from waves that have been reflected at the interface below the target. In theory, this is a very difficult case, because small-angle scattering is involved, and it is well-known that Born approximation is least accurate for small scattering angles.

To compute the above difference traces, the BRM implementation for displacement seismograms had to be only slightly modified. The results are now multiplied with the respective value of the Lamé parameter λ near the source. Therefore, the pressure modelling algorithm allows one to simulate pressure seismograms as efficiently as displacement / particle velocity traces with the same program.

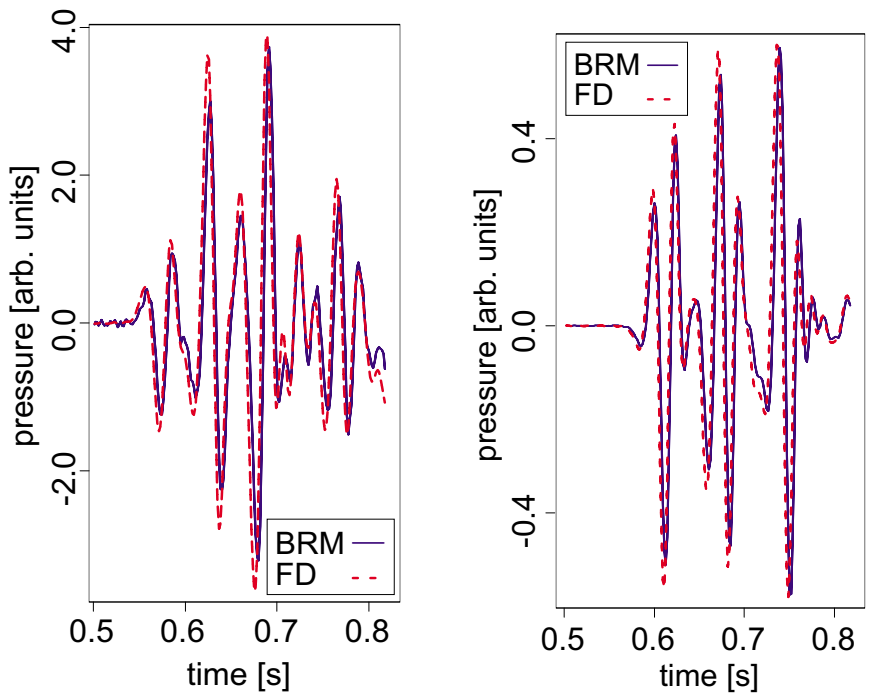

Figure 5.3: Change of seismic (pressure) traces due to a 5% increase of the *shear modulus* c_{55} inside the target zone of the earth model in Figure 5.1. (a) Zero-offset trace recorded near the surface at $x = 100$m.
(b) Offset 500m. The source was at $x = 100$m, the receiver at $x = 600$m.

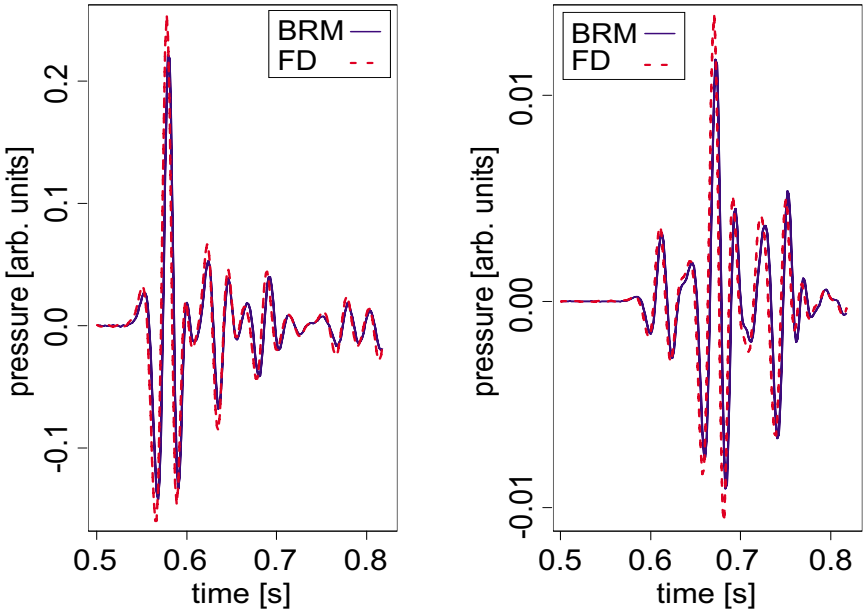

(a) **(b)**

Figure 5.4: Change of seismic (pressure) traces due to a 5% increase of the *density* ρ inside the target zone of the earth model in Figure 5.1. (a) Zero-offset trace recorded near the surface at $x = 100$m.
(b) Offset 500m. The source was at $x = 100$m, the receiver at $x = 600$m.

Chapter 6

Reservoir anisotropy

6.1 Introduction

6.1.1 Elastic waves in anisotropic media

When we investigate the earth with seismic waves, it is normally described as an isotropic medium. However, many natural materials actually show *anisotropic* behaviour, i.e., propagation velocities depend on the direction of a travelling wave. In this context, the term "anisotropic" refers to a medium that is inhomogeneous on a scale much smaller than the wavelength of the probing seismic wave. Sometimes this may even be the atomic scale. A passing elastic wave cannot resolve such small-scale heterogeneities. Therefore, it behaves as if it was propagating through a *homogeneous* medium with certain effective properties. This effective medium reflects the intrinsic symmetry of the inhomogeneous material. If the distribution of small-scale heterogeneities is non-uniform or depends somehow on direction, the effective medium might be anisotropic. Of course, the type of anisotropy of a certain material may vary with the length scale considered.

Three types of anisotropy are found at the seismic scale. These are transverse isotropy (or hexagonal anisotropy), orthorhombic anisotropy, and monoclinic anisotropy. The simplest and most frequently encountered kind is transverse isotropy, which is caused by thinly layered structures. These can be, e.g., layers of different types of rock, but also parallel oriented fractures. A transversely isotropic medium possesses a symmetry axis perpendicular to the layers. Depending on the orientation of the axis, we distinguish between "vertically transverse isotropy" (VTI, vertical symmetry axis) and "horizontally transverse isotropy" (HTI, horizontal symmetry axis). This is illustrated in Figure 6.1. Orthorhombic anisotropy is equivalent to a superposition of vertically and horizontally transverse isotropy. Monoclinic anisotropy can be produced by superimposing tilted fractures on a layered medium (Ebrom and Sheriff, 1991; Schoenberg and Muir, 1989).

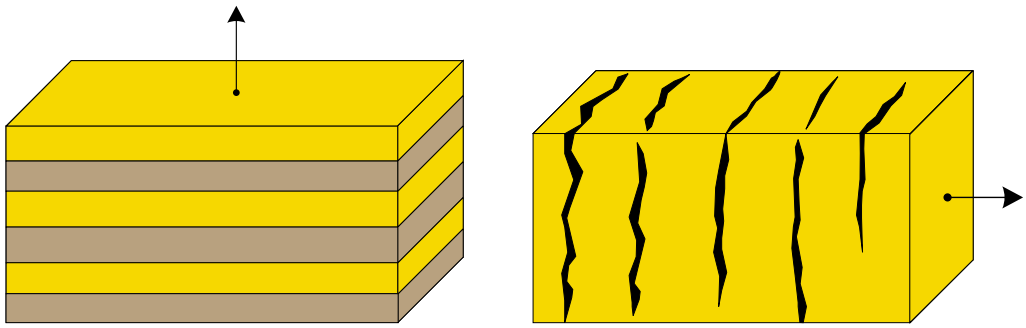

(a) Vertically transversely isotropic (VTI) medium consisting of thin horizontal layers of rock.

(b) Horizontally transversely isotropic (HTI) medium. Anisotropic behaviour is caused by vertically oriented parallel fractures.

Figure 6.1: Illustration of materials with effective transversely isotropic behaviour (after Ebrom and Sheriff (1991)). Vertically transverse isotropy is frequently found for thinly layered media, whereas systems of vertically oriented parallel fractures produce horizontally transverse isotropy.

6.1.2 Fine structure of reservoirs

Fracturing is important for fluid flow in many reservoirs. The knowledge of the location and orientation of fractures can help to find optimum locations for wells. With suitable processing, it is possible to extract anisotropy parameters and thus fracture orientation and intensity from seismic data — especially in connection with S-waves or converted waves (MacBeth and Crampin, 1991; Winterstein and Meadows, 1991a,b). In (three-dimensional) anisotropic media, there are in general two independent S-wave modes, which propagate at different wave speeds. This phenomenon is called birefringence, or S-wave splitting. The polarisation indicates fracture orientation, and the degree of splitting gives a rough measure of the fracture intensity. Modelling wave propagation in anisotropic media is therefore important for survey design.

6.1.3 Production-related changes of reservoir anisotropy

Seismic time-lapse studies can be used to investigate production-related changes of reservoir symmetry (e.g. Winterstein et al., 1998). The cause of such a behaviour might be the deliberate extension of fractures or the creation of new ones by inserting fluid at a well with high pressure ("hydraulic fracturing", Meadows and Winterstein (1994); Groenenboom and van Dam (2000); Groenenboom and Falk (2000)).

The closing or opening of cracks due to changes of effective stress (i.e., confining stress minus pore pressure) tends to increase or decrease the effective elastic moduli (Nur and Simmons, 1969; Schön, 1983; Mavko et al., 1998). Consequently, seismic anisotropy may indicate production-induced changes of the stress condition in the reservoir. Cracks will preferentially be affected, if the confining stress is perpendicular to the crack faces. Depending on the fracture distribution at low stress, and on the symmetry and direction of the confining stress, different types of effective anisotropy may arise (Nur, 1971). Figure 6.2 illustrates the stress-induced anisotropy of the P-wave velocity according to measurements of Nur and Simmons (1969). Similar results have been obtained for the two S-wave polarisations.

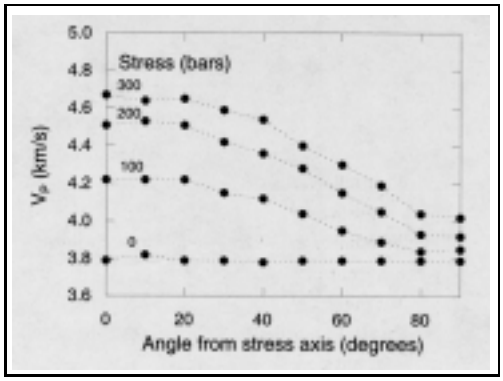

Figure 6.2: Stress-induced anisotropy of P-wave propagation according to Nur and Simmons (1969); Mavko et al. (1998). The rock becomes considerably stiffer in the direction parallel to the applied uniaxial stress resulting in a transversely isotropic effective medium. The original crack distribution was isotropic.

6.1.4 BRM for anisotropic media

Born Repeat-Modelling (BRM) can provide synthetic difference seismograms corresponding to anisotropic perturbations of reservoir properties. The most general version of the BRM equation (Eqn. 4.3) contains a general modification δc_{mjkl} of the stiffness tensor instead of the Lamé parameters:

$$\begin{aligned} u_i^{\mathrm{P}}(\mathbf{r};\omega) \;\approx\; & u_i(\mathbf{r};\omega) + \omega^2 \int_{\mathrm{res}} dV'\, G_{mi}\left(\mathbf{r}',\mathbf{r};\omega\right)\, \delta\rho\left(\mathbf{r}'\right) u_m\left(\mathbf{r}';\omega\right) \\ & + \int_{\mathrm{res}} dV'\, G_{mi,j}\left(\mathbf{r}',\mathbf{r};\omega\right)\, \delta c_{mjkl}\left(\mathbf{r}'\right) u_{k,l}\left(\mathbf{r}';\omega\right) \;. \end{aligned} \tag{6.1}$$

This feature allows to calculate the change of the seismic response for arbitrarily anisotropic reservoir perturbations. The formula was implemented for general anisotropic media.

For isotropic overburdens, anisotropic BRM may be combined with an isotropic finite-difference modelling (FDM) scheme. This also is important, if no anisotropic FDM implementation is available. Then, anisotropic modelling results are available at the shorter computation time of the simpler, isotropic scheme.

6.2 Stiffness and velocities in anisotropic media

6.2.1 Structure of the stiffness tensor

In contrast to the two elastic moduli of the isotropic case, it requires five independent parameters to completely determine a transversely isotropic elastic material. These moduli can be conveniently represented using the abbreviated notation (see Sect. 2.2.4):

$$\begin{pmatrix} c_{11} & c_{12} & c_{13} & 0 & 0 & 0 \\ c_{12} & c_{11} & c_{13} & 0 & 0 & 0 \\ c_{13} & c_{13} & c_{33} & 0 & 0 & 0 \\ 0 & 0 & 0 & c_{55} & 0 & 0 \\ 0 & 0 & 0 & 0 & c_{55} & 0 \\ 0 & 0 & 0 & 0 & 0 & c_{66} \end{pmatrix} \quad \text{where } c_{12} = c_{11} - 2c_{66} \ . \tag{6.2}$$

c_{55} was used instead of c_{44} for consistency with the two-dimensional case. Here, the axis of symmetry is oriented along the z-direction. A two-dimensional transversely isotropic medium is completely determined by the shaded matrix elements.

For orthorhombic media, there are even nine independent elastic moduli. If the coordinate planes are the symmetry planes of the orthorhombic medium, the stiffness tensor becomes

$$\begin{pmatrix} c_{11} & c_{12} & c_{13} & 0 & 0 & 0 \\ c_{12} & c_{11} & c_{23} & 0 & 0 & 0 \\ c_{13} & c_{23} & c_{33} & 0 & 0 & 0 \\ 0 & 0 & 0 & c_{44} & 0 & 0 \\ 0 & 0 & 0 & 0 & c_{55} & 0 \\ 0 & 0 & 0 & 0 & 0 & c_{66} \end{pmatrix} \ . \tag{6.3}$$

Even for transverse isotropy, all elements of the above matrix may become non-zero after an arbitrary rotation. Therefore, an implementation of BRM for general

anisotropic media is necessary unless extreme restrictions for the orientation of the symmetry axis are accepted. The shading of matrix elements shows that this symmetry class will not differ from a transversely isotropic medium in 2-D.

6.2.2 Weak elastic anisotropy – Thomsen parameters

Expressions for the seismic velocities in anisotropic media are rather complicated. Therefore, Thomsen (1988) proposed a convenient notation for weakly anisotropic VTI media. Seismic velocities are parametrised with the following five constants ("Thomsen parameters"):

$$\alpha = \sqrt{\frac{c_{33}}{\rho}} \qquad \text{(vertical P-wave velocity)}, \tag{6.4}$$

$$\beta = \sqrt{\frac{c_{55}}{\rho}} \qquad \text{(vertical S-wave velocity)}, \tag{6.5}$$

$$\epsilon = \frac{c_{11} - c_{33}}{2c_{33}} \qquad \text{("P-wave anisotropy")}, \tag{6.6}$$

$$\gamma = \frac{c_{66} - c_{55}}{2c_{55}} \qquad \text{("S-wave anisotropy")}, \tag{6.7}$$

$$\delta = \frac{(c_{13} + c_{55})^2 - (c_{33} - c_{55})^2}{2c_{33}(c_{33} - c_{55})} \ . \tag{6.8}$$

In a transversely isotropic material, there are three independent solutions of the elastodynamic wave equation: the quasi-longitudinal wave (P), the transverse wave (SH), and the quasi-transverse wave (SV). In terms of the Thomsen-parameters, the phase velocities of these waves are:

$$v_{\mathrm{P}}(\theta) = \alpha(1 + \delta \sin^2\theta \cos^2\theta + \epsilon \sin^4\theta) \tag{6.9}$$

$$v_{\mathrm{SV}}(\theta) = \beta\left(1 + \frac{\alpha^2}{\beta^2}(\epsilon - \delta)\sin^2\theta\cos^2\theta\right) \tag{6.10}$$

$$v_{\mathrm{SH}}(\theta) = \beta(1 + \gamma \sin^2\theta) \ . \tag{6.11}$$

The angle between the wavefront normal and the vertical axis is denoted by θ. A similar notation exists for HTI media (e.g. Tsvankin and Grechka, 2000). Thomsen (1988) argues that δ is the most important anisotropy parameter, because it governs the wave speed of the P-wave for nearly vertical propagation ($\theta \approx 0$).

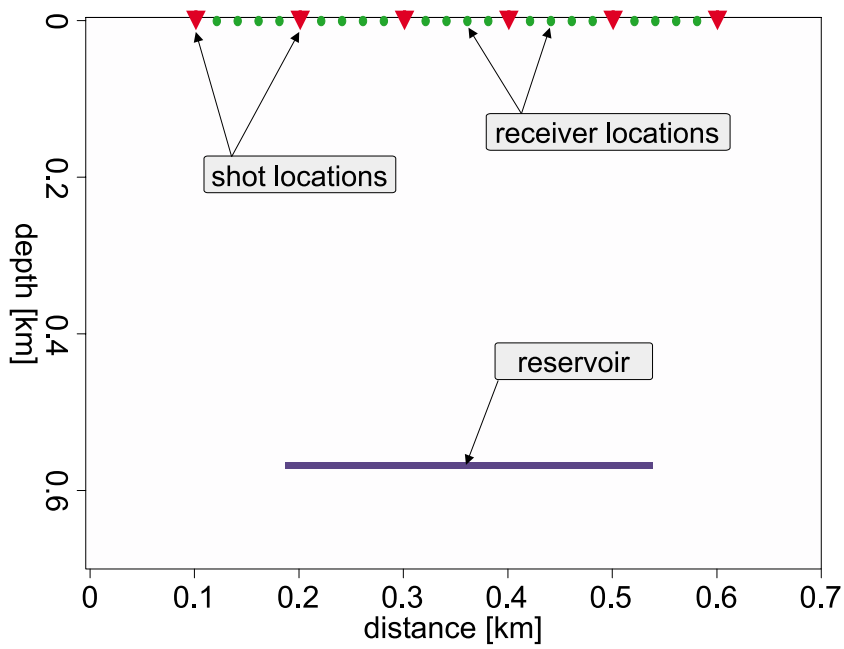

Figure 6.3: Earth model for anisotropic reservoir perturbation

6.3 Example

6.3.1 Setup and earth model

A detailed test of the anisotropic BRM modelling scheme was performed to investigate how the quality of simulation results depends on the offset, and on the relative position of source and target. For the former purpose, I show several shot gathers, whereas the latter is treated by analysing zero-offset sections.

The numerical experiments are done for a homogeneous 700m$\times$700m earth model already used in previous tests of the isotropic scheme. A sketch of this earth model is depicted in Figure 6.3. Parameters of the homogeneous and isotropic background are $v_P = 4000\frac{m}{s}$, $v_S = 2236\frac{m}{s}$, and density $\rho = 2\frac{g}{cm^3}$. Production-related changes of the reservoir are simulated by uniform modifications of the elastic properties inside the 360m$\times$16m rectangular target zone near the bottom of the earth model.

The triangles and dots at the surface of the earth model indicate locations where the vertical displacement component has been recorded in the numerical experiments. At the places of the triangles, seismic sources have been installed in addition to the receivers. The leftmost source (at $x = 100$m) was used in the common-shot experiment, whereas the traces of the zero-offset experiment correspond to all triangle

locations. Elastic waves were stimulated by impulsive, vertical body forces at the respective source point. The source wavelet has the shape of the derivative of a Gaussian function with central frequency $f_c = 35\text{Hz}$.

All seismograms shown below consist of difference traces that do not describe the temporal variation of a displacement component, but the *change* of displacement in consequence of reservoir modifications. For comparison, all traces have been re-calculated with a transversely isotropic, elastic FDM scheme originally implemented by Martin Karrenbach (Karrenbach, 1995). I have used the following parameters:

Grid spacing:	2m
Sampling interval:	1.6ms (internal sampling interval: 0.2ms)
Recording length:	8192 time steps

To avoid reflections from the edges of the model, boundaries have been added at all sides. All the BRM traces have been calculated with the same Green's function data set. Although generated with the anisotropic FDM scheme, this data set could as well have been obtained with an isotropic scheme. Because of the symmetry of the earth model, only three FDM runs were necessary to obtain the complete Green's function data set required for all shot- and zero-offset gathers.

6.3.2 Modelling results for isotropic reservoir perturbation

Isotropic perturbation

The first step in the development of the anisotropic BRM scheme was a test of its behaviour for isotropic reservoir perturbations. An isotropic parameter modification is a special case of a anisotropic perturbation with

$$\begin{aligned} \delta c_{11} &= \delta c_{33} \\ \delta c_{13} &= \delta c_{11} - 2\,\delta c_{55} \\ \delta c_{15} &= \delta c_{35} = 0 \end{aligned} \tag{6.12}$$

in 2-D (in abbreviated subscript notation).

The results of such a test can be easily compared with existing simulations made with the isotropic scheme to check consistency. I restrict the following discussion of the isotropic limit to a small perturbation of the P-wave modulus c_{33}. It is chosen because, according to theory, perturbations of c_{33} are expected to be the most critical ones (see Section 4.3.2).

The main interest in reflection seismics lies in P-waves propagating in nearly vertical direction. Hence, the name c_{33} is preferred before c_{11}, because c_{33} determines the speed of P-waves in transversely isotropic materials for vertical direction of propagation (see Section 6.3.3).

Synthetic seismograms for $\delta c_{33}/c_{33} = 5\%$

Shot gather at x=100m Figure 6.4(a) shows the change of a shot gather caused by an isotropic perturbation of c_{33} by 5% in the target. For comparison, results of FDM and BRM are plotted together in the same figure. The source was located near the surface at $x = 100$m on the left-hand side of the earth model (Figure 6.3). 26 traces have been recorded with 20m receiver spacing, starting at zero-offset.

Only the P-wave should be affected by an isotropic perturbation of c_{33}, therefore only two events are expected in the seismograms. Both are diffractions of the P-wave at the upper left and upper right corners of the target. At the source point, the diffraction from the left-hand side comes at $t \approx 0.3$s, whereas the other wave arrives at $t \approx 0.38$s. With increasing offset, both events approach each other and finally join at the largest offset. The second event has only a comparatively small amplitude and is therefore hardly detectable in the shot gather. Figures 6.4(b) - 6.4(d) show zoomed traces, where this event is clearly visible. In addition to the expected events, there are others at $t \approx 0.5$s and $t \approx 0.65$s in the zero-offset trace. These travel times correspond to S-waves and converted waves.

Zero-offset gather In a similar manner, zero-offset traces have been obtained (Figure 6.5). The source/receiver locations were at $x = 100$m, 200m, 300m, 400m, 500m, and 600m. The rather large trace spacing had to be chosen, because for every zero-offset trace an additional FD simulation is required. With the Green's function data used in the preceeding section, a zero-offset gather with 20m spacing between traces is available by means of BRM within minutes.

In Figure 6.5, we see both P-wave events described above. Being separate in the leftmost zero-offset trace, they join in the centre and separate again farther on the right. Of course, this symmetry of the seismogram reflects the symmetry of the earth model. In the BRM traces, there are also the additional undesired events already identified in the shot gather.

Discussion

The travel times and wave forms, and even the amplitudes of the P-wave events agree very well in the results for isotropic perturbation of c_{33}. The small observed deviation apparently increases with offset, but does not depend on the shot location.

In the results of the purely isotropic modelling scheme and of FDM, most of these additional S-wave and converted wave events have not been observed, at all. Thus, they are clearly identified as artifacts. The difference traces for isotropic perturbation of c_{33} are created in the anisotropic scheme by adding the independent (anisotropic) results obtained for c_{11}, c_{13}, and c_{33}, respectively. The reason for the

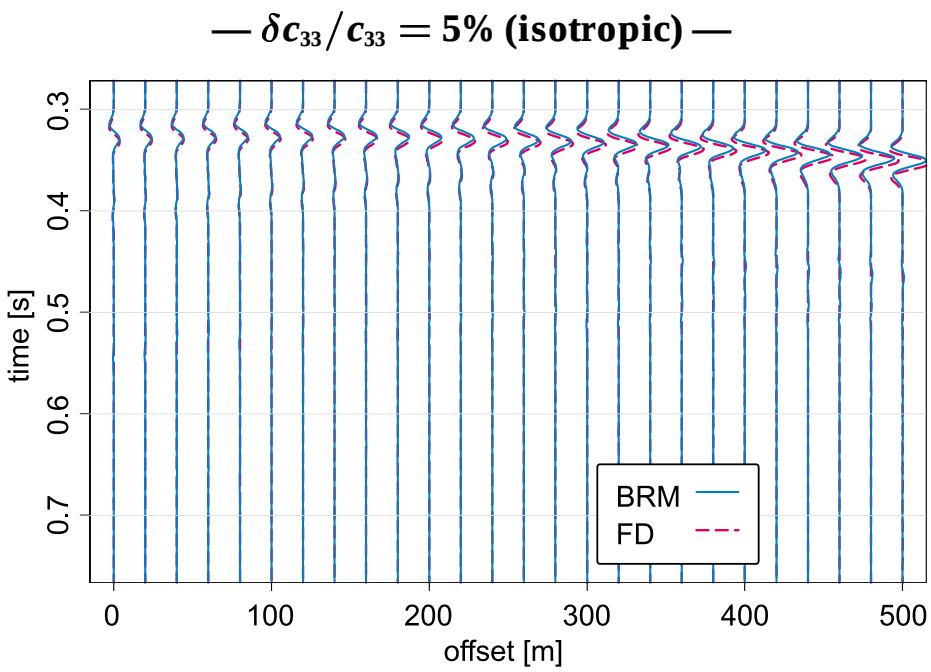

(a) Shot gather

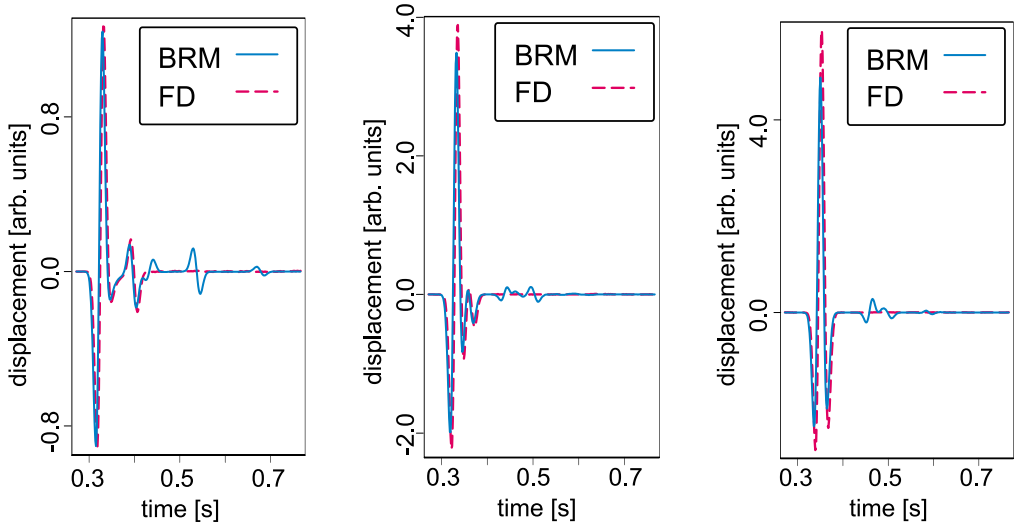

(b) Zero-offset trace **(c)** Offset 300m **(d)** Offset 500m

Figure 6.4: Change of a shot gather over the earth model shown in Figure 6.3 caused by the isotropic reservoir perturbation $\delta c_{33}/c_{33} = 5\%$. The source was located at $x = 100$m.

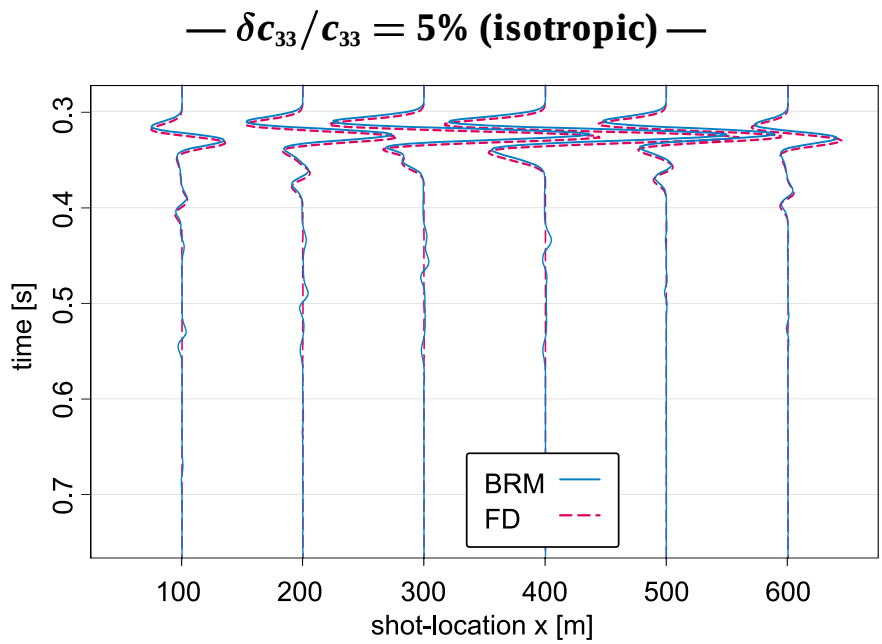

Figure 6.5: Change of zero-offset traces for isotropic reservoir perturbation $\delta c_{33}/c_{33} = 5\%$ in the earth model shown in Figure 6.3.

undesired events lies in the already incorrect results computed for some of the constituents, especially c_{11}, which fail to completely cancel out each other (See also Section 6.3.3).

In contrast to the isotropic scheme, the contributions of the different stiffness components are independent and *must* be calculated separately. Obviously, this makes anisotropic BRM a little bit more sensitive to inaccuracies. However, these results should still be sufficiently accurate to allow a reasonable estimate of the maximum amplitude of a signal, and of the wave form of a certain P-wave event.

6.3.3 Results for transversely isotropic reservoir perturbation

Elastic parameters for TI media – types of perturbation

As mentioned above, in a transversely isotropic material, there are three independent solutions of the elastodynamic wave equation: the quasi-longitudinal wave (P-wave), the transverse wave (SH-wave), and the quasi-transverse wave (SV-wave). In a 2-D medium – as used in this study – no SH-wave exists. Therefore, the "V" of the SV-wave will be dropped in the following.

The propagation velocities of these waves are determined in 2-D by four independent elastic moduli: c_{11}, c_{13}, c_{33}, and c_{55}. For vertical wave propagation in a vertically transversely isotropic medium (VTI), the wave speeds are

$$\begin{aligned} v_{\mathrm{P}}(\text{vertical}) &= \sqrt{\frac{c_{33}}{\rho}} \\ v_{\mathrm{S}}(\text{vertical}) &= \sqrt{\frac{c_{55}}{\rho}} \,. \end{aligned} \tag{6.13}$$

For other angles, – even for a weakly anisotropic VTI medium – the variation of the velocities with angle (for near-offset reflection configuration) is determined by the parameter δ, which is a function of almost all of the moduli. Consequently, perturbations of all possible parameters must be tested. In the following, I show a selection of my results.

Perturbations of c_{13}

In an isotropic material, the value of the c_{13}-component of the stiffness tensor is implicitly determined by the choice of c_{33} and c_{55}. This condition is relaxed in anisotropic media, and c_{13} may deviate from its isotropic limit $\lambda = c_{33} - 2c_{55}$.

In this section, I investigate whether BRM can model effects in the seismic response of the earth model caused by uniform perturbations of c_{13} from its isotropic limit

inside the target zone. The accuracy of Born approximation is expected to reduce for larger perturbations. Therefore, in addition to 5% deviation from the isotropic limit, the larger perturbation $\delta c_{13}/c_{13} = 20\%$ was tested. These perturbations cause values of 0.019 and 0.079, respectively, of the Thomsen anisotropy parameter δ inside the reservoir.

Behaviour for 5% perturbation Figures 6.6 and 6.7 show my results for 5% perturbation of c_{13}. In Figure 6.6(a) a shot gather with 26 traces can be seen. Again, there are the two P-wave events, both with two-way travel time $t \approx 0.33$s in the 500m-offset trace (zoomed in Fig. 6.6(d)). In contrast to the isotropic case, I also observe converted wave events and S-wave events at travel times $t \approx 0.44$s, and $t \approx 0.57$s, respectively, in the 500m-offset trace. With decreasing offset, all three reflection events split into two diffraction events coming from the upper left and upper right corners of the target. The same seismic events are found in the zero-offset section depicted in Figure 6.7.

The agreement of FDM and BRM results is quite good. A small phase-shift is observed almost throughout both gathers. Nevertheless, the wave forms and the amplitudes match almost perfectly in most parts of the seismograms. Only events involving S-waves seem to exhibit a small difference in amplitude between FDM and BRM. Although some events in some traces seem to deviate more than others, a pronounced dependence of accuracy on the offset or source location is hardly evident.

Behaviour for 20% perturbation Simulation results for the larger reservoir perturbation $\delta c_{13}/c_{13} = 20\%$ can be seen in Figures 6.8 and 6.9. It is not a surprise that these seismograms are very similar to the ones obtained for the 5% case. In agreement with the expectation that Born approximation is more accurate for small perturbations, the differences in signal amplitude between BRM and FDM have generally grown. However, I do not observe an increase of the time shift, or a change of the of the wave form. For larger offsets, the increase of the error seems to be more pronounced for S-waves than for P-waves. A dependence on the source location is not discernible.

Perturbation of c_{33}

As mentioned in Section 6.3.2, the difference seismograms for complex reservoir modifications are obtained as sum of the separate contributions of the different components of the stiffness tensor. For the isotropic results discussed in Section 6.3.2, the by far strongest contribution comes from the modulus c_{33}. This stiffness component dominates, because it mainly determines the vertical P-wave

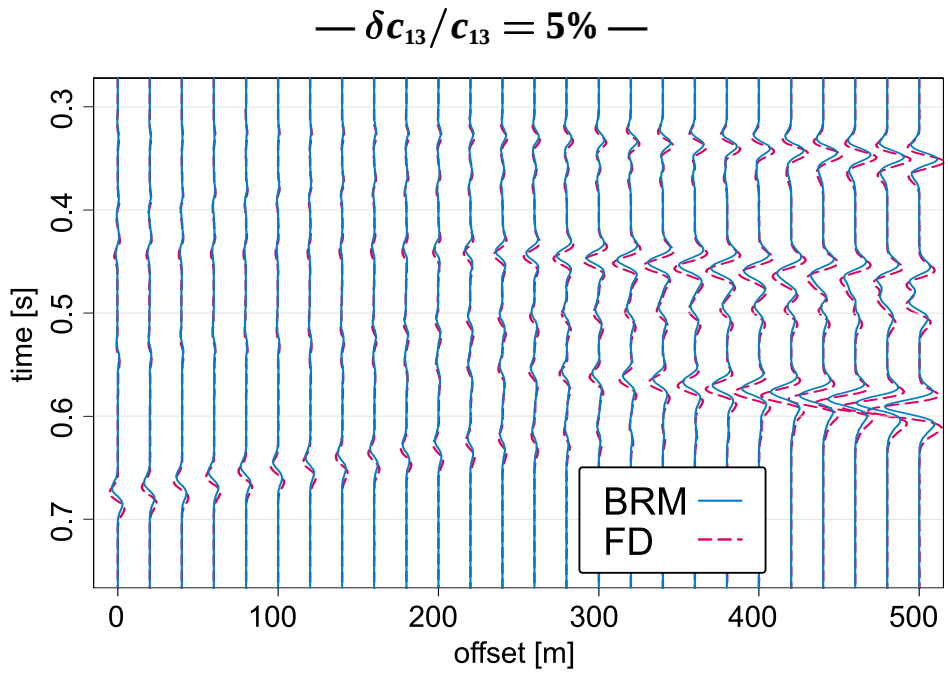

(a) Shot gather

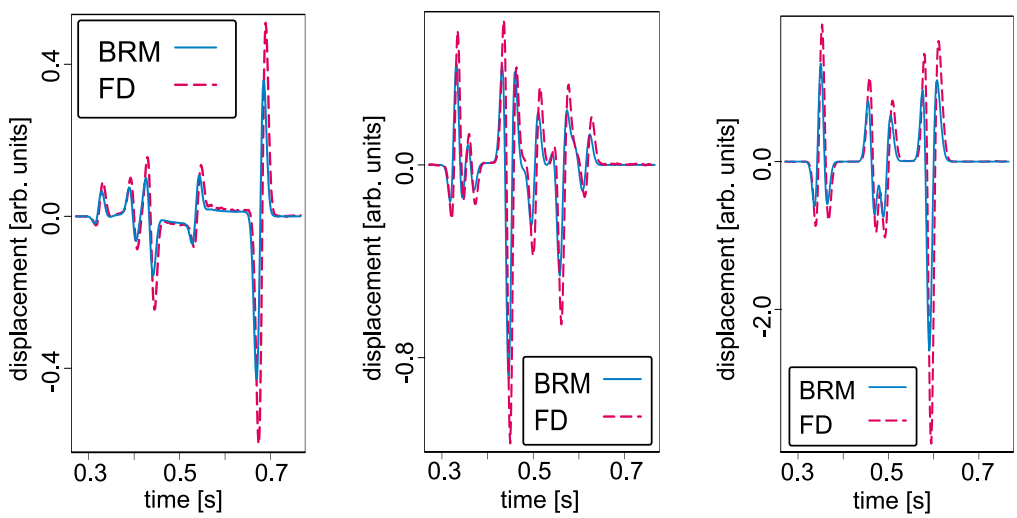

(b) Zero-offset trace **(c)** Offset 300m **(d)** Offset 500m

Figure 6.6: Change of a shot gather over the earth model shown in Figure 6.3 caused by the reservoir perturbation $\delta c_{13}/c_{13} = 5\%$. The source was located at $x = 100$m.

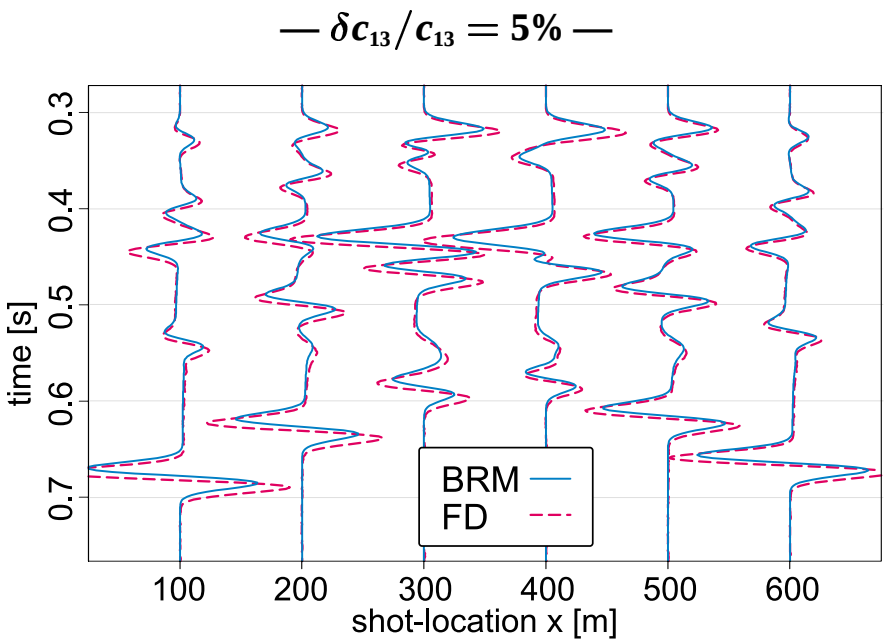

Figure 6.7: Change of zero-offset traces for reservoir perturbation $\delta c_{13}/c_{13} = 5\%$ in the earth model shown in Figure 6.3.

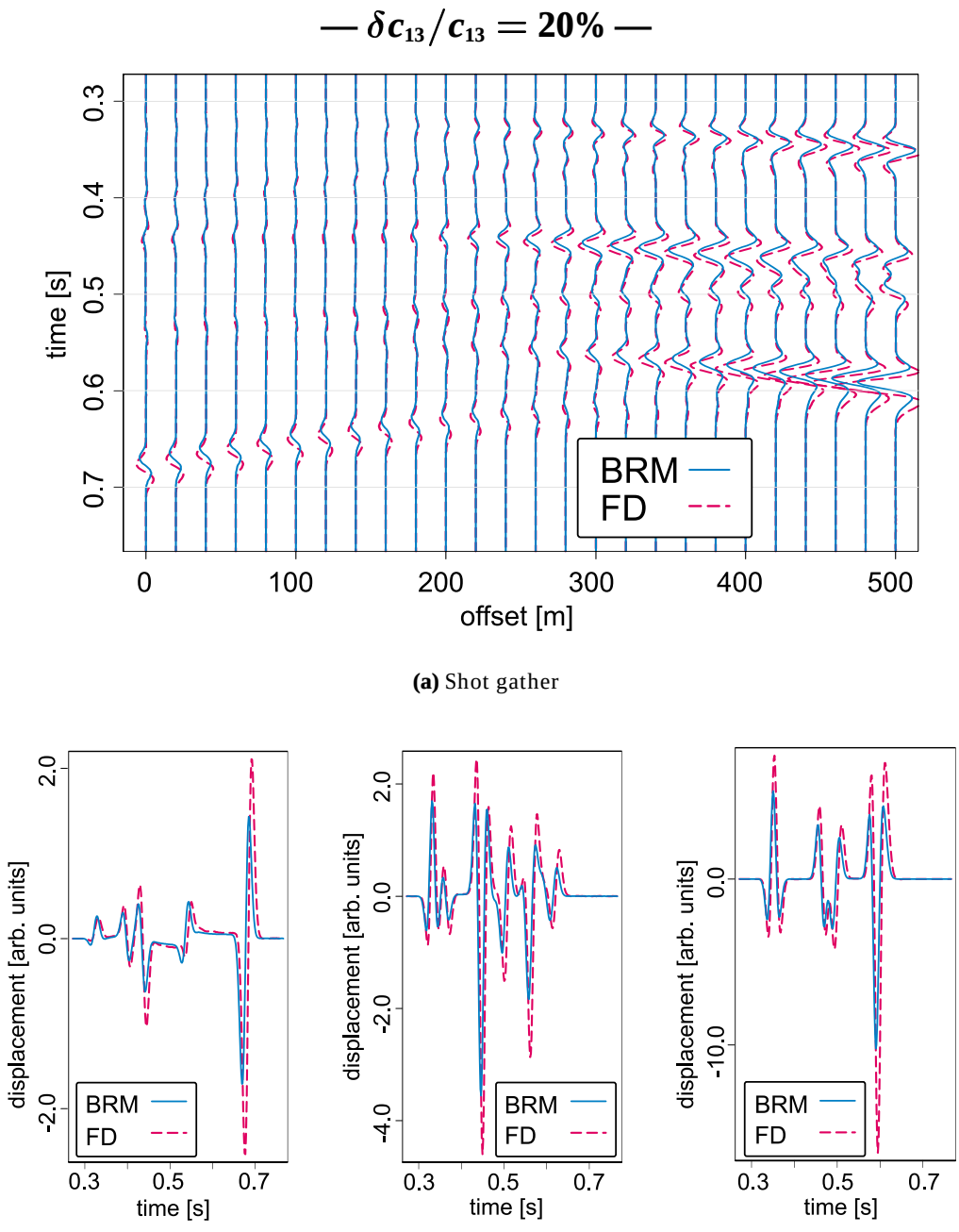

(a) Shot gather

(b) Zero-offset trace

(c) Offset 300m

(d) Offset 500m

Figure 6.8: Change of a shot gather over the earth model shown in Figure 6.3 caused by the reservoir perturbation $\delta c_{13}/c_{13} = 20\%$. The source was located at $x = 100$m.

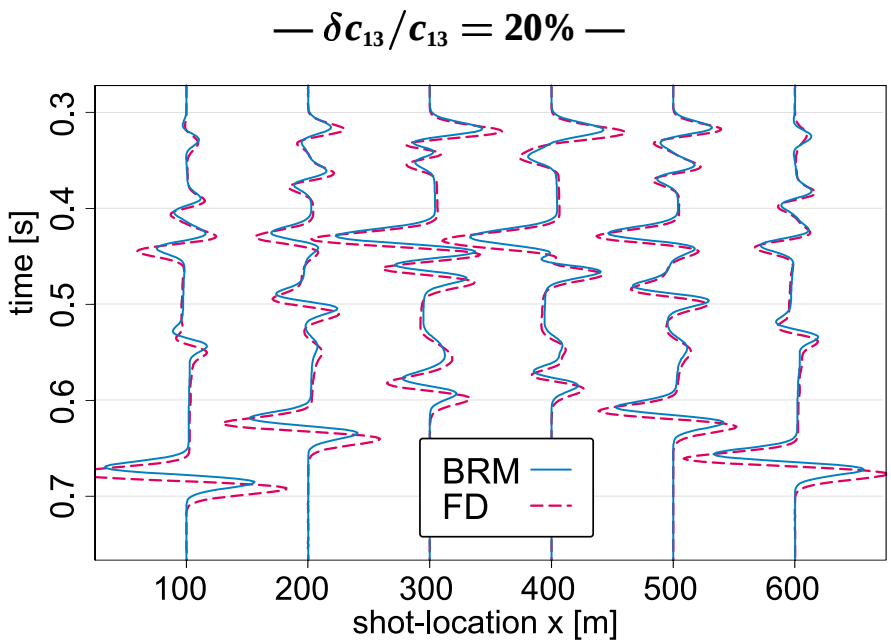

Figure 6.9: Change of zero-offset traces for reservoir perturbation $\delta c_{13}/c_{13} = 20\%$ in the earth model shown in Figure 6.3.

velocity for both, isotropic and transversely isotropic media. In this section, I investigate a 5% perturbation of c_{33} inside the target zone, which gives rise to reservoir anisotropy with Thomsen parameters $\delta = -0.046$ and $\epsilon = -0.024$.

Figures 6.10 and 6.11 show difference seismograms computed with BRM and FDM. As expected, all of them are very similar to the corresponding results obtained for isotropic perturbation of c_{33}. I identify all types of events already discussed for the perturbations of c_{13}. These are quasi-P-waves, converted waves, and quasi-S-waves. Hardly any difference is visible in the results of FDM and BRM.

In contrast to the isotropic perturbation of c_{33}, theory predicts S-wave scattering in the current case too. I observe that for the traces calculated with BRM and with FDM, the agreement with regard to the S-wave events is as good as for the P-wave events. c_{33} is the most important constituent for the isotropic seismograms. However, in this case the S-wave events are also strongly influenced by other stiffness components.

Perturbations of c_{11} and c_{55}

The last contribution to the difference seismograms for isotropic perturbation of the P-wave modulus comes from c_{11}. Synthetic difference seismograms for 5% reservoir modification are depicted in Figures 6.12 and 6.13. This corresponds to Thomson parameters $\delta = 0$, and $\epsilon = 0.025$. δ is equal zero. Thus, c_{11} only very weakly affects the near-vertical P-wave velocity, and I expect only very small P-wave events in the seismograms.

All seismic events according to the section on c_{13}-perturbations are seen in the simulation results. However, the agreement of curves computed with BRM and FDM is not as good as for the cases discussed above. Although travel times and wave forms are consistent, the amplitude difference can reach 50%. This is particularly evident from the zero-offset gather shown in Figure 6.13.

The situation is similar for c_{55}, which mainly determines near-vertical S-wave motion: I have tested a 5% perturbation of this modulus, which results in Thomsen parameters $\delta = 0.032$ and $\epsilon = 0$. A shot gather for source location $x = 100$m can be seen in Figure 6.14(a), a zero-offset gather in Figure 6.13.

The travel time and shape of all events are modelled very well by BRM. Like for c_{11}, I observe strong discrepancies of the amplitudes in some parts of the seismograms. However, the error is far smaller than for c_{11}. In both cases, these deviations from the FDM result seem to vary strongly with the source location. Starting on the left-hand side of the earth model the discrepancy is quite large, but decreases more and more approaching the centre. Finally, on the right-hand side of the model, it can hardly be detected.

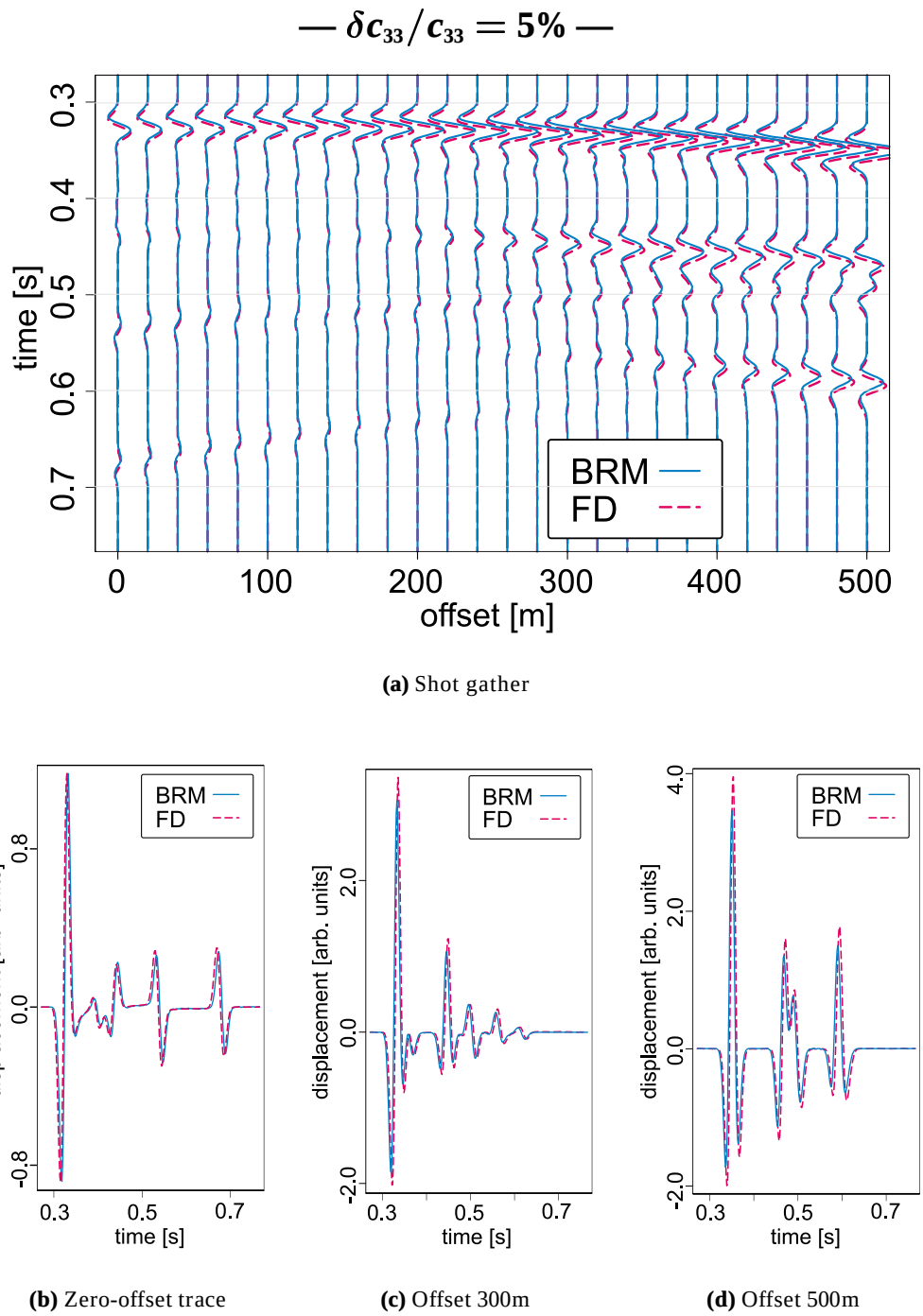

(a) Shot gather

(b) Zero-offset trace

(c) Offset 300m

(d) Offset 500m

Figure 6.10: Change of a shot gather over the earth model shown in Figure 6.3 caused by the reservoir perturbation $\delta c_{33}/c_{33} = 5\%$. The source was located at $x = 100$m.

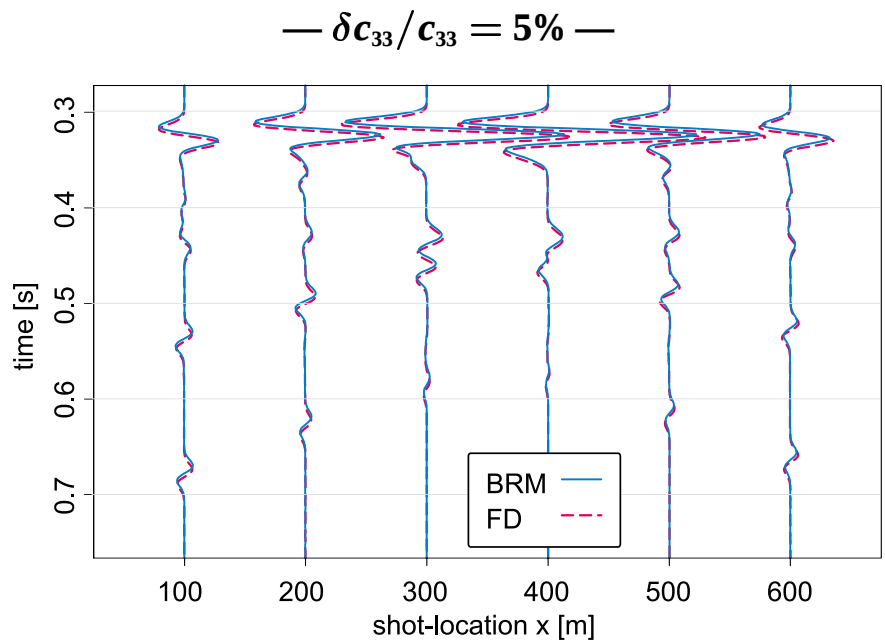

Figure 6.11: Change of zero-offset traces for reservoir perturbation $\delta c_{33}/c_{33} = 5\%$ in the earth model shown in Figure 6.3.

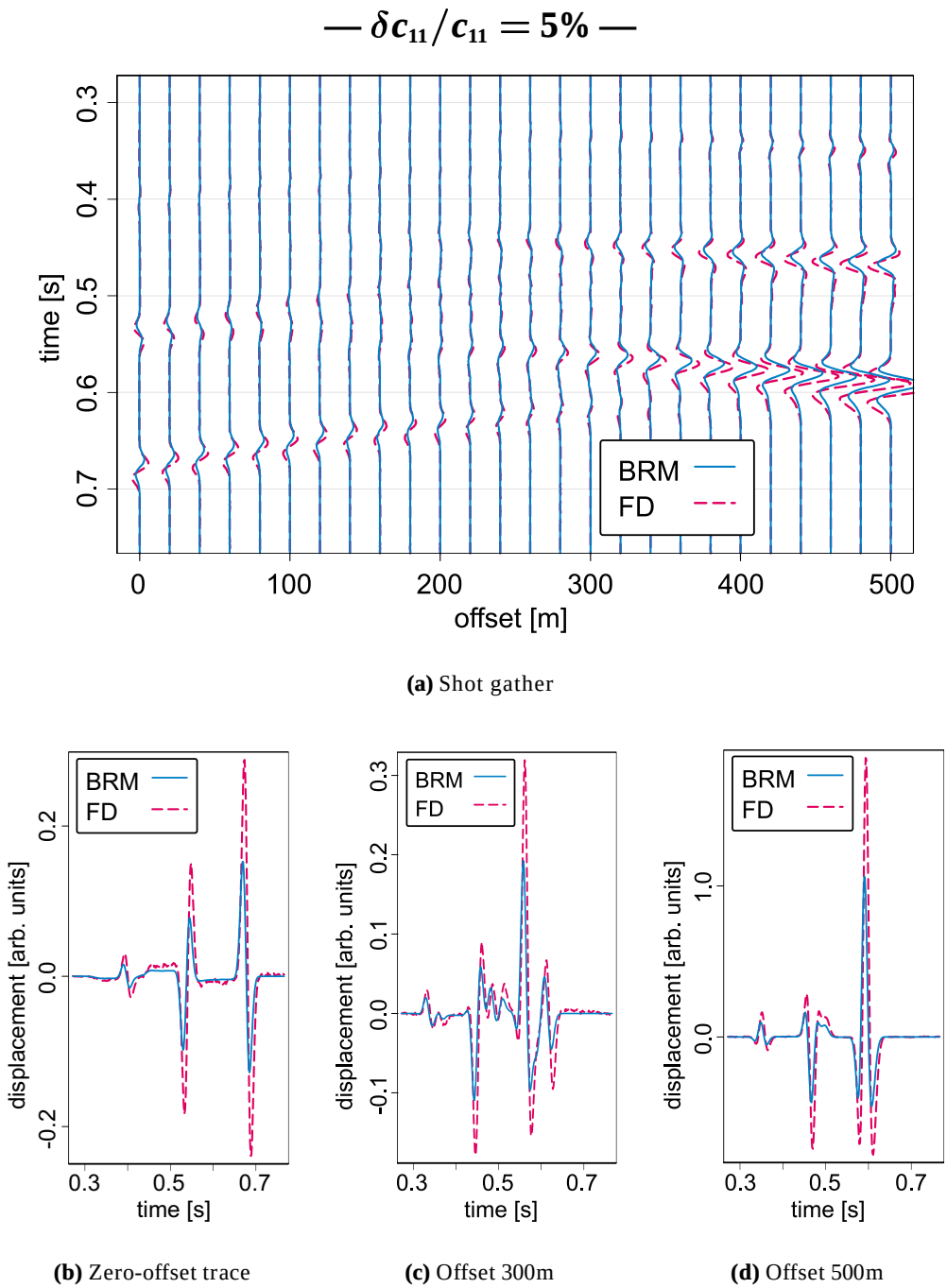

(a) Shot gather

(b) Zero-offset trace

(c) Offset 300m

(d) Offset 500m

Figure 6.12: Change of a shot gather over the earth model shown in Figure 6.3 caused by the reservoir perturbation $\delta c_{11}/c_{11} = 5\%$. The source was located at $x = 100$m.

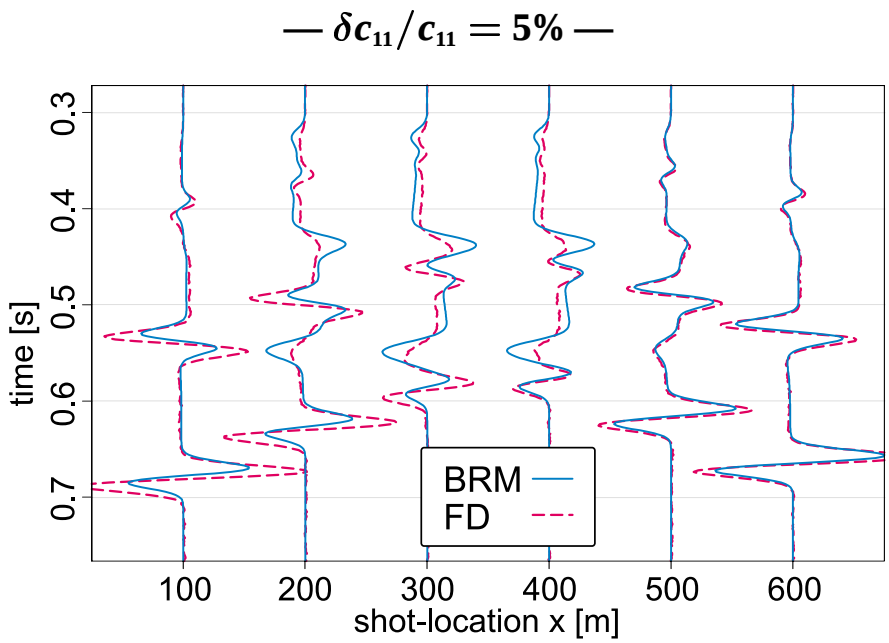

Figure 6.13: Change of zero-offset traces for reservoir perturbation $\delta c_{11}/c_{11} = 5\%$ in the earth model shown in Figure 6.3.

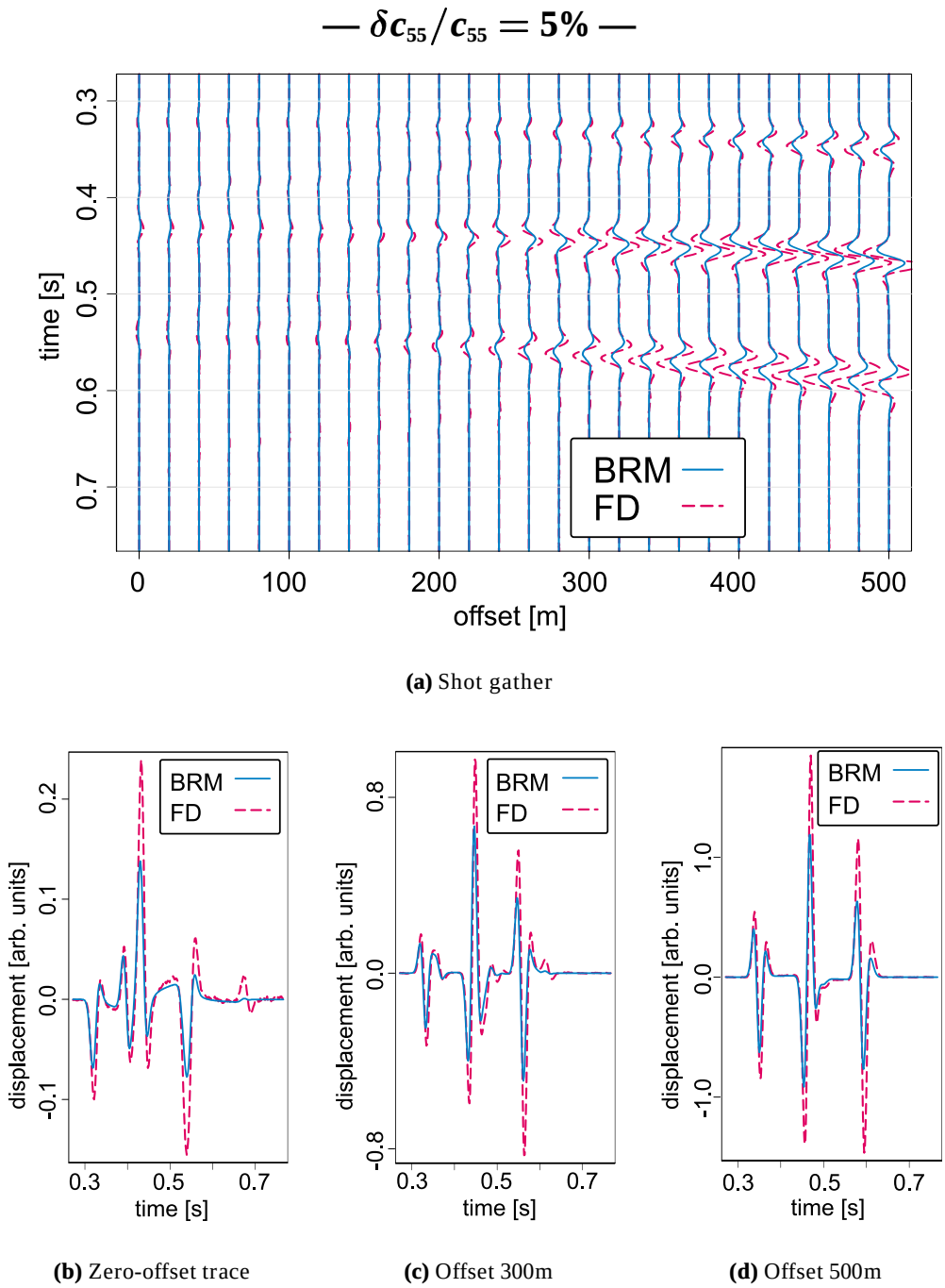

(a) Shot gather

(b) Zero-offset trace

(c) Offset 300m

(d) Offset 500m

Figure 6.14: Change of a shot gather over the earth model shown in Figure 6.3 caused by the reservoir perturbation $\delta c_{55}/c_{55} = 5\%$. The source was located at $x = 100$m.

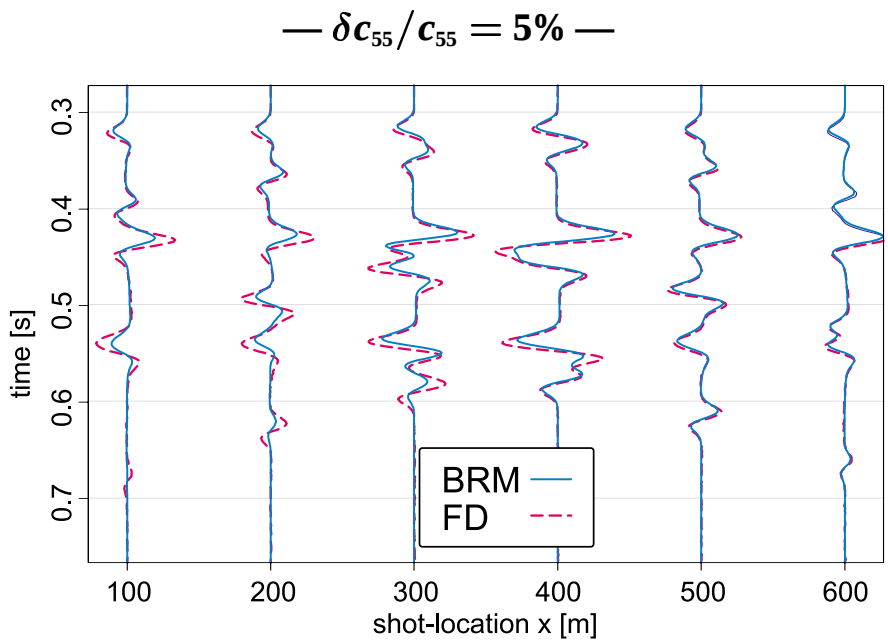

Figure 6.15: Change of zero-offset traces for reservoir perturbation $\delta c_{55}/c_{55} = 5\%$ in the earth model shown in Figure 6.3.

6.3.4 Computing time

For comparison of the efficiency of BRM and FDM, averages of the computation times required by both methods for different modelling tasks have been listed together in Table 6.1. The values are the averages of computing times for several runs, multiplied with the number of CPUs used. The fluctuations are small. The given computation times are real times and thus include all required input/output activity.

Depending on the type of perturbation, the BRM calculations involve a different number of numerical operations and access different amounts of Green's function data. For example, perturbations of c_{13} always needed 20% more time than perturbations of c_{33}. Anisotropic computation of the isotropic perturbation of c_{33} is even more complex. It requires that the contributions of c_{11}, c_{13}, and c_{33} be computed separately. Obviously, there must be considerable synergy effects because the resulting computing time is much less than the sum of the computing times of the constituents. The BRM time for finite offsets is larger than for zero-offset because twice as much Green's function data must be loaded. FDM can simulate a whole shot gather at a time, whereas the time required for BRM is proportional to the number of traces.

6.3.5 Conclusions

This study investigates the applicability of the anisotropic extension of BRM for a simple, homogeneous earth model. As a first step, an isotropic modification of c_{33} in the reservoir was tested to check the consistency with isotropic modelling. In addition, I compare synthetic seismograms obtained with BRM and FDM for transversely isotropic reservoir perturbations.

The agreement of BRM and FDM results is good for perturbations of c_{13} and c_{33}. These are the most important elastic moduli for seismic exploration, because they mainly determine P-wave motion in near-vertical directions. The composition of difference seismograms corresponding to the isotropic limit from their anisotropic constituents works also very well, particularly for P-wave events. However, the different contributions failed to completely cancel out for the S-wave events. Reservoir modifications of c_{11} and c_{55} show a rather weak performance in my test, which explains the behaviour for the isotropic case. However, these moduli give only small contributions.

I have shown that BRM can be extended to anisotropic media. Although anisotropic BRM shows a greater sensitivity to inaccuracies than the isotropic scheme, the results are very good for most of the seismic events of interest.

geometry	perturbed modulus	BRM (avg.) [s]	FDM (avg.) [h]	ratio [%]
common-shot (26 traces)	c_{33} (iso)	290	52	0.15
	c_{33}	160	52	0.085
	c_{13}	220	52	0.12
	c_{11}	160	52	0.085
	c_{55}	160	52	0.085
zero-offset (6 traces)	c_{33}	36	310	0.0032
	c_{13}	48	310	0.0043
	c_{11}	36	310	0.0032
	c_{55}	36	310	0.0032
single trace	c_{33} (iso)	11	52	0.0059
	c_{33}	5.9	52	0.0032
	c_{13}	8.0	52	0.0043
	c_{11}	6.0	52	0.0032
	c_{55}	5.9	52	0.0032

Table 6.1: Comparison of average computation times of BRM (Repeat-Modelling step) and FDM for different recording geometries. The times given are real CPU times including input / output activity (two significant figures). Differences in CPU performance and clock rate on the different machines are not taken into account.

Chapter 7

Conclusions and perspectives

For planning seismic time-lapse experiments, entire seismic surveys have to be simulated for several reservoir configurations.

The novel Born Repeat-Modelling (BRM) technique presented in this thesis combines accurate finite-difference modelling (FDM) in the overburden with a perturbation approach for the reservoir. Thus, BRM computes the change of the seismograms that is caused by production-related changes of the reservoir properties. With numerical examples, I have investigated the applicability of the proposed procedure for all possible types of isotropic reservoir perturbations. A test with the Marmousi model demonstrates the performance of BRM for an extremely complex overburden structure.

I propose an efficient way of extending BRM to the simulation of pressure seismograms, which are recorded in marine seismic surveys. Moreover, BRM is generalised to modelling difference seismograms corresponding to arbitrary anisotropic perturbations of the reservoir properties. Both cases have been examined in numerical tests. In particular, as a test of anisotropic BRM, I have very accurately modelled the seismic effects of different kinds of transversely isotropical reservoir perturbations. To my knowledge, such a detailed numerical time-lapse study with regard to anisotropic alterations of structures slightly below the dominant seismic wavelength has not been published.

In all my investigations, the results of BRM have been compared with corresponding results of finite-difference simulations. The difference seismograms obtained with both techniques are very similar to each other. However, owing to the perturbation approach, the quality of the BRM results decreases with increasing seismic frequency and for large modifications of the reservoir, thus limiting the application of BRM. Nevertheless, when applicable, the accuracy of BRM was close to the accuracy of FDM.

Being specifically developed for time-lapse modelling, BRM avoids redundancies inherent in the standard modelling techniques. Therefore, in all tests a very large part – frequently more than 99% – of the computational effort was saved in comparison with FDM.

For the future, some technical improvements of BRM are desirable. For example, obtaining spatial derivatives of the wave field directly from FDM would allow much finer sampling of the Green's function. Thus, the required computational effort might easily be reduced by another order of magnitude, facilitating the simulation of difference seismograms for much larger earth models and reservoirs.

The impulse to start working on the problem of time-lapse modelling originally came from a company that has supported this research all along. As BRM can meet the demands of accuracy and efficiency in many cases, its application in industry appears to be possible.

Appendix A

Implementation of BRM

A.1 Outline of the algorithm

Driven by the need to minimise requirements of computing time and of computer memory, the implementation of BRM has continually developed during my work. In the final version, my implementation is divided into two progams, `Green` and `RMod` (see Figure A.1):

- `Green` contains all operations that must be done only once for a given earth model.
- `RMod` requires the result of `Green`. It performs all calculations that must be repeated for every desired reservoir configuration.

In order to repeat as little operations as possible the computation of the Fourier transform and of the spatial derivatives of the wave field are done in `Green`. This reduces the computation time of `RMod` at the expense of large Green's function data sets. The procedure is the same in 2-D and 3-D. However, because of pronounced differences in the actual data structures separate programs have been developed for two and three dimensions.

A.2 Generation of Green's functions – `Green`

The input to the program `Green` are all the values of the displacement components inside the reservoir for all source and receiver locations involved. They have to be produced with a finite-difference modelling (FDM) tool. In the ideal case, the

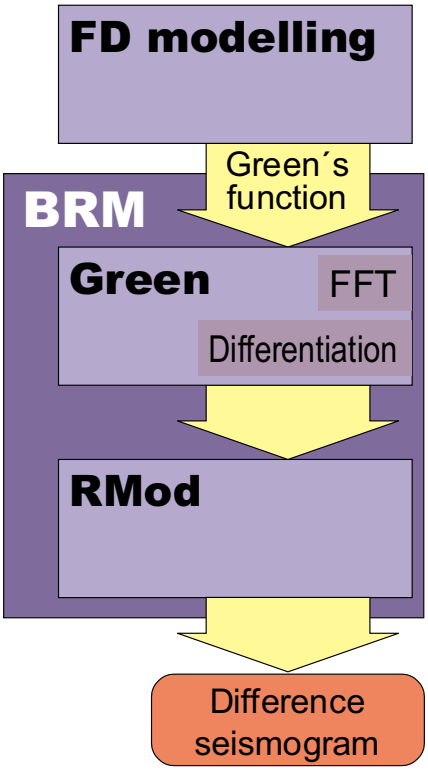

Figure A.1: Flow chart illustrating the implementation of the BRM algorithm

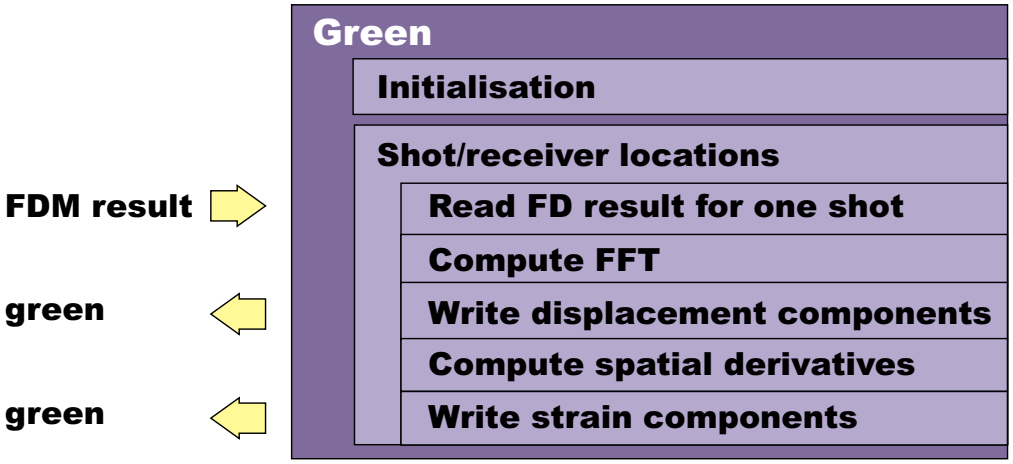

Figure A.2: Diagram of the structure of the program Green

complete input data can be obtained as a by-product of a reference simulation of the respective time-lapse survey carried out with FDM.

Details of the procedure are shown in Figure A.2. For every source and receiver location of interest, Green computes the Fast Fourier Transform (FFT, see, e.g., Press et al. (1992)) of the displacement field with respect to time. Subsequently, the derivatives of all components with respect to every spatial direction is computed using finite-difference operators according to Section 3.2.3.

Thus, Green produces a large data set that contains all components of the displacement and all strain components for all source and receiver locations. For each earth model only one run of Green is necessary.

If the amount of data is too large, the calculations of Green may be carried out in a sequential way (not shown in the figure). Then only one spectral component of the fields is considered at a time. The sequential computation also reduces the computing time because the computation and data input/output are better balanced.

A.3 Repeat-modelling – RMod

The program RMod performs all calculations that have to be repeated when the reservoir model changes. For a given deviation of the density and of the elastic moduli from the original configuration of the resevoir, RMod computes the corresponding difference seismograms. For this, RMod requires the result of Green. In addition, RMod uses information about the survey geometry and the source wavelet used to simulate the Green's function with FDM.

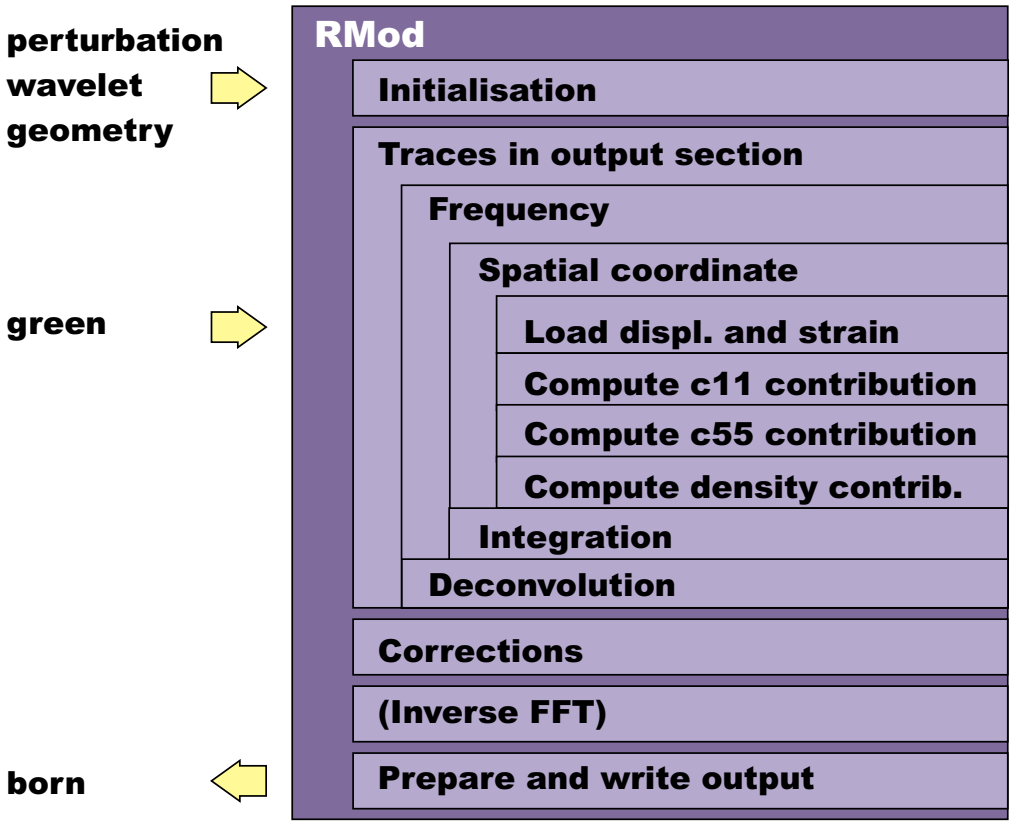

Figure A.3: Diagram of the structure of the program `RMod`

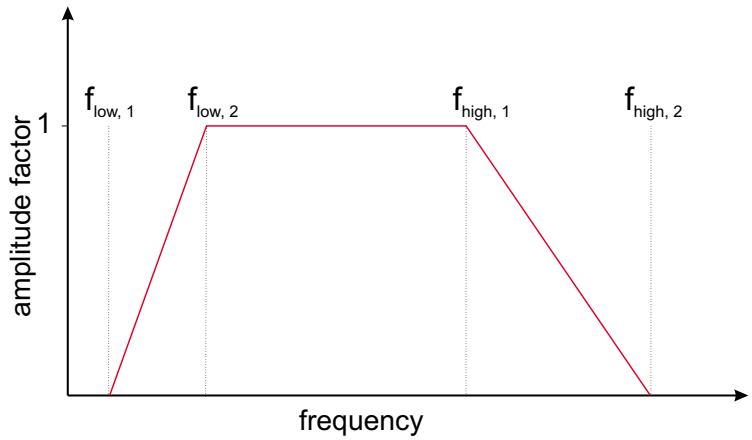

Figure A.4: Trapezoid-shaped filter applied in the Repeat-Modelling step to make deconvolution convergent.

RMod computes each trace separately. Similar to the sequential mode of Green, RMod offers the possibility to consider only a small number of spectral components of the Green's function at a time. The number of spectral components considered at a time is a very critical parameter for perrfomance. It should be chosen as small as possible.

The contributions of the perturbations $\delta\rho$, δc_{11}, and δc_{55} to the difference seismogram are always calculated separately. If more than one of these quantities changes at a time, the total difference trace is obtained by adding the separately calculated contributions.

In Section 4.2.1, I show that there is a symmetry between incident wave field and the Green's function. Therefore, I only use one data set for both purposes and deconvolve the result of integration (according to Equation'4.4) with the source wavelet used to simulate the incident field.

However, because of the limited bandwidth of the source wavelet, there will always divisions by zero at very low and very high frequencies. Pre-whitening was tested, but involved too many spurious effects. Therefore, I only consider spectral components associated with a sufficienly high amplitude. In addition a trapezoid-shaped filter is applied to cut off insignificant spectral components that have been erroneously amplified. As shown in Figure A.4, the shape of this filter is determined by four characteristic frequencies.

References

Aki, K. and Richards, P. G. (1980). *Quantitative Seismology*, volume 1: Theory and Methods. W. H. Freeman and Company, New York.

Al-Fares, M. H. (1995). Mapping impedance changes using a target-oriented approach: A feasibility study for 3-D seismic monitoring. *Journal of Seismic Exploration*, 4:305–314.

Anderson, R. M., Guerin, G., Boulanger, A., Mello, U., and Watson, T. J. (1998). 4-D seismic reservoir simulation in a South Timbalier 295 turbidite reservoir. *The Leading Edge*, 17(10):1416–1418.

Auld, B. A. (1990). *Acoustic Fields and Waves in Solids*, volume 1. Krieger Publishing Company, Malabar, Florida, 2nd edition.

Biondi, B., Mavko, G., Mukerij, T., Ricket, J., Lumley, D., Deutsch, C., Gundesø, R., and Thiele, M. (1998). Reservoir monitoring: A multidisciplinary feasibility study. *The Leading Edge*, 17(10):1404–1414.

Bronstein, I. N. and Semendjajev, K. A. (1981). *Taschenbuch der Mathematik*. Verlag Harry Deutsch, Thun und Frankfurt (Main).

Burkhart, T., Hoover, A. R., and Flemings, P. B. (2000). Time-lapse (4-D) seismic monitoring of a primary production of turbidite reservoirs at South Timbalier Block 295, offshore Lousiana, Gulf of Mexico. *Geophysics*, 65(2):351–367.

Burridge, R., de Hoop, M. V., Miller, D., and Spencer, C. (1998). Multiparameter inversion in anisotropic elastic media. *Geophysical Journal International*, 134:757–777.

Červený, V. (2000). *Seismic Ray Theory*. Cambridge University Press, Cambridge, UK.

Chapman, C. H. and Coates, R. T. (1994). Generalized Born scattering in anisotropic media. *Wave Motion*, 19:309–341.

Clayton, R. and Engquist, B. (1977). Absorbing boundary conditions for acoustic and elastic wave equations. *Bulletin of the Seismological Society of America*, 67(6):1529–1540.

Cohen-Tannoudji, C., Diu, B., and Laloë, F. (1977). *Quantum Mechanics*, volume II. John Wiley & Sons, New York.

Ebrom, D. and Sheriff, R. E. (1991). Anisotropy and reservoir development. In Sheriff (1991b), pages 355–361.

Gjøystdal, H., Lecomte, I., Mjelva, A. E., Maaø, F., Hokstad, K., and Johansen, T. A. (1998). Fast repeated seismic modelling of local complex targets. In *68th Annual International Meeting, Expanded Abstracts*, pages 1452–1455. Society of Exploration Geophysicists.

Gold, N. (1997). *Theoretical and Numerical Description of the Propagation of Elastic Waves in Random Media*. PhD thesis, Karlsruhe University.

Gold, N., Shapiro, S. A., and Burr, E. (1997). Modelling of high contrasts in elastic media using a modified finite difference scheme. In *67th Annual International Meeting, Expanded Abstracts*. Society of Exploration Geophysicists. ST 14.6.

Greaves, R. J. and Fulp, T. J. (1991). Three-dimensional seismic monitoring of an enhanced oil recovery process. In Sheriff (1991b), pages 309–320. Originally published in *Geophysics*, 52:1175-1187.

Groenenboom, J. (1998). *Acoustic Monitoring of Hydraulic Fracture Growth*. PhD thesis, Delft University of Technology, The Netherlands.

Groenenboom, J. and Falk, J. (2000). Scattering by hydraulic fractures: Finite-difference modelling and laboratory data. *Geophysics*, 65(2):612–622.

Groenenboom, J. and van Dam, D. B. (2000). Monitoring hydraulic fracture growth: Laboratory experiments. *Geophysics*, 65(2):603–611.

Gubernatis, J., Domanij, E., and Krumhansl, J. (1977a). Formal aspects of the theory of scattering of ultrasound by flaws in elastic materials. *Journal of Applied Physics*, 48(7):2804–2811.

Gubernatis, J., Domanij, E., Krumhansl, J., and Huberman, M. (1977b). Born approximation in the theory of the scattering of elastic waves by flaws. *Journal of Applied Physics*, 48(7):2812–2819.

Habashy, T. M., Groom, R. W., and Spies, B. R. (1993). Beyond the Born and Rytov approximations: A nonlinear approach to electromagnetic scattering. *Journal of Geophysical Research*, 98(B2):1759–1775.

He, W., Guerin, G., Anderson, R. N., and Mello, U. T. (1998). Time-dependent reservoir characterization of the LF sand in the South Eugene Island 330 field, Gulf of Mexico. *The Leading Edge*, 17(10):1434–1438.

Hertweck, T. (2000). *Practical aspects of the unified approach to seismic imaging*. Diplomarbeit, Karlsruhe University.

Hoffmann, H. J. and Rekdal, T. (1999). Model-based survey planning for modern seismic acquisition technologies. In *61th Annual Meeting, Extended Abstracts*. European Association of Geoscientists and Engineers. Session: 06-03.

Hokstad, K., Lecomte, I., Maaø, F. A., Tuseth, M., Mjelva, E., Gjøystdal, H. E. A., and Sollie, R. (1998). Hybrid modelling of elastic wavefield propagation. In *60th Annual Meeting, Extended Abstracts*. European Association of Geoscientists and Engineers. Session: 05-56.

Holberg, O. (1987). Computational aspects of the choice of operator and sampling interval for numerical differentiation in large-scale simulation of wave phenomena. *Geophysical Prospecting*, 35:629–655.

Huang, X., Meister, L., and Workman, R. (1998). Improving production history matching using time-lapse seismic data. *The Leading Edge*, 17(10):1430–1433.

Hudson, J. A. (1980). *The excitation and propagation of elastic waves*. Cambridge University Press, Cambridge, UK, 1st edition.

Hudson, J. A. and Heritage, J. R. (1981). The use of the Born approximation in seismic scattering problems. *Geophysical Journal of the Royal Astronomical Society*, 66:1981.

Jenkins, S. D., Waite, M. W., and Bee, M. F. (1997). Time-lapse monitoring of the Duri steamflood: A pilot and case study. *The Leading Edge*, 16(9):1267–1273.

Johnston, D. H., Eastwood, J. E., Shyeh, J. J., Vaulthrin, R., Khan, M., and Stanley, L. R. (2000). Using legacy seismic data in an integrated time-lapse study: Lena field, Gulf of Mexico. *The Leading Edge*, 19(3):294–302.

Johnston, D. H., McKenny, R. S., Verbeek, J., and Almond, J. (1998). Time-lapse seismic analysis of Fulmar Field. *The Leading Edge*, 17(10):1420–1428.

Justice, J. H. (1991). Geophysical methods for reservoir surveillance. In Sheriff (1991b), pages 281–284.

Karrenbach, M. (1995). *Elastic tensor wavefields*. PhD thesis, Stanford University.

Keller, J. B. (1969). Accuracy and validity of the Born and Rytov approximations. *Geophysics*, 59(1):1003–1004.

Kelly, K. R., Ward, R. W., Treitel, S., and Alford, R. M. (1976). Synthetic seismograms: A finite-difference approach. *Geophysics*, 41(1):2–27.

Kennet, B. L. N. (1972). Seismic waves in laterally homogeneous media. *Geophysical Journal of the Royal Astronomical Society*, 27:301–325.

Key, S. C., Pederson, S. H., and Smith, B. A. (1998). Adding value to reservoir management with seismic monitoring technologies. *The Leading Edge*, 17(4):515–519.

Kirchner, A. and Shapiro, S. A. (1998). Making the simulation of monitoring experiments more efficient. In *60th Annual Meeting, Extended Abstracts*. European Association of Geoscientists and Engineers. Session: 05-54.

Kirchner, A. and Shapiro, S. A. (1999). Fast repeat-modelling with Born approximation. In *61st Annual Meeting, Extended Abstracts*. European Association of Geoscientists and Engineers. Session: 4011.

Kirchner, A. and Shapiro, S. A. (2000). Fast repeat-modelling of time-lapse seismograms. *Geophysical Prospecting*. Submitted in June 2000.

Kneib, G. and Kerner, C. (1993). Accurate and efficient seismic modeling in random media. *Geophysics*, 58(4):576–588.

Koster, K., Gabriels, P., Hartung, M., Verbeek, J., Deinum, G., and Staples, R. (2000). Time-lapse seismic surveys and their business impact. *The Leading Edge*, 19(3):286–293.

Lazaratos, S. K. and Marion, B. P. (1997). Crosswell seismic imaging of reservoir changes caused by CO_2 injection. *The Leading Edge*, 16(9):1300–1306.

Lecomte, I. (1996). Hybrid modeling with ray tracing and finite difference. In *66th Annual International Meeting, Expanded Abstracts*, pages 699–702. Society of Exploration Geophysicists.

Levander, A. R. (1988). Fourth-order finite-difference P-SV seismograms. *Geophysics*, 53(11):1425–1436.

Lo, L. and Inderwiesen, P. (1994). *Fundamentals of Seismic Tomography*. Society of Exploration Geophysicists, Tulsa, Oklahoma.

Lumley, D. E. (1995). 4-D seismic monitoring of an active steamflood. In *65th Annual International Meeting, Expanded Abstracts*, pages 203–206. Society of Exploration Geophysicists.

Lumley, D. E., Behrens, R. A., and Wang, Z. (1997). Assessing the technical risk of a 4-D seismic project. *The Leading Edge*, 16(9):1287–1291.

Lumley, D. E., Nur, A., Strandenes, S., Dvorkin, J., and Packwood, J. (1994). Seismic monitoring of oil production: A feasibility study. In *64th Annual International Meeting, Expanded Abstracts*. Society of Exploration Geophysicists.

MacBeth, C. and Crampin, S. (1991). Processing of seismic data in the presence of anisotropy. *Geophysics*, 56(9):1320–1330.

Madariaga, R. (1976). Dynamics of an expanding circular fault. *Bulletin of the Seismological Society of America*, 66:639–666.

Matthews, L. (1991). 3-D seismic monitoring of an in-situ thermal process. In Sheriff (1991b), pages 301–308.

Mavko, G., Mukerij, T., and Dvorkin, J. (1998). *The Rock Physics Handbook. Tools for seismic analysis in porous media*. Cambridge University Press, Cambridge, UK.

Meadows, M. A. and Winterstein, D. F. (1994). Seismic detection of a hydraulic fracture from shear-wave VSP data a Lost Hills Field, California. *Geophysics*, 59(1):11–26.

Miles, J. W. (1960). Scattering of elastic waves by small inhomogeneities. *Geophysics*, 25(3):642–648.

Mittet, R. (1994). Implementation of the Kirchhoff integral for elastic waves in staggered-grid modeling schemes. *Geophysics*, 59(12):1894–1901.

Mittet, R. and Arntsen, B. (1998). A 3D elastic hybrid modelling scheme. In *60th Annual Meeting, Extended Abstracts*. European Association of Geoscientists and Engineers. Session: 05-55.

Müller, T. M. and Shapiro, S. A. (2000). Most probable seismic pulses in single realizations of 2-D and 3-D random media. *Geophysical Journal International*. submitted.

Nur, A. (1971). Effects of stress on velocity anisotropy in rocks with cracks. *Journal of Geophysical Research*, 76(8):2022–2034.

Nur, A. and Simmons, G. (1969). Stress-induced velocity anisotropy in rock: An experimental study. *Journal of Geophysical Research*, 74(27):6667–6674.

Oristaglio, M. A. (1985). Accuracy and validity of the Born and Rytov approximations for reflection and refraction at a plane interface. *Journal of the Optical Society of America A*, 2(11):1987–1993.

Packwood, J. L. (1996). Feasibility of hydrocarbon monitoring with increasing rock frame stiffness. In *66th Annual International Meeting, Expanded Abstracts*. Society of Exploration Geophysicists.

Press, W. H., Teukolsky, S. A., Vetterling, W. T., and Flannery, B. P. (1992). *Numerical Recipes in C. The Art of Scientific Computing*. Cambridge University Press, 2nd edition.

Robertson, J. D. (1991). Reservoir management using 3-D seismic data. In Sheriff (1991b), pages 25–35.

Robertsson, J. O. A. and Chapman, C. (1999). An efficient method for calculating finite-difference seismograms after model alterations. In *69th Annual International Meeting, Expanded Abstracts*, pages 1848–1851. Society of Exploration Geophysicists.

Robertsson, J. O. A. and Chapman, C. H. (2000). An efficient method for calculating finite-difference seismograms after model alterations. *Geophysics*, 53(3):907–918.

Robertsson, J. O. A., Ryan-Grigor, S., Sayers, C. M., and Chapman, C. H. (2000). A finite-difference injection approach to modeling of seismic fluid flow monitoring. *Geophysics*, 65(3):896–906.

Robertsson, J. O. A., Sayers, C., Chapman, C., and Ryan-Grigor, S. (1999). A finite-difference injection approach to modeling of seismic fluid flow monitoring. In *69th Annual International Meeting, Expanded Abstracts*, pages 1691–1694. Society of Exploration Geophysicists.

Rytov, S. M., Kravtsov, Y. A., and Tatarskii, V. I. (1989). *Principles of Statistical Radio Physics*, volume 3: Elements of Random Fields. Springer Verlag, Berlin.

Saenger, E. H., Gold, N., and Shapiro, S. A. (2000). Modeling the propagation of elastic waves using a modified finite-difference grid. *Wave Motion*, 31(1):77–92.

Santos, L. T., Schleicher, J., Tygel, M., and Hubral, P. (1998). A new modelling for time-lapse application. In *60th Annual Meeting, Extended Abstracts*. European Association of Geoscientists and Engineers. Session: 05-53.

Sato, H. and Fehler, M. C. (1998). *Seismic Wave Propagation and Scattering in the Heterogeneous Earth*. Springer Verlag, Berlin.

Scales, J. A. (1994). *Theory of Seismic Imaging*. Samizdat Press, Golden, Colorado. Freely available via ftp from `hilbert.mines.colorado.edu`.

Schoenberg, M. and Muir, F. (1989). A calculus for finely layered media. *Geophysics*, 54(5):581–589.

Schön, J. (1983). *Petrophysik*. Akademie-Verlag, Berlin.

Shapiro, S. A. and Hubral, P. (1999). *Elastic Waves in Random Media. Fundamentals of Seismic Stratigraphic Filtering*. Springer Verlag, Berlin.

Sheriff, R. E. (1991a). Basic petrophysics and geophysics. In Sheriff (1991b), pages 37–49.

Sheriff, R. E., editor (1991b). *Reservoir Geophysics*. Society of Exploration Geophysicists, Tulsa, Oklahoma.

Sheriff, R. E. and Geldart, L. P. (1995). *Exploration Seismology*. Cambridge University Press, Cambridge, UK, 2nd edition.

Simm, R., Uden, R. H., Buford, S., Plummer, C., Harrison, P., and Johnson, R. (1997). 4D seismic modelling – Nelson field, central North Sea. In *59th Annual Meeting, Extended Abstracts*. European Association of Geoscientists and Engineers.

Smith, W. D. (1975). The application of finite element analysis to body wave propagation problems. *Geophysical Journal of the Royal Astronomical Society*, 42:747–768.

Story, C., Peng, P., Heubeck, C., Sullivan, C., and Lin, J. D. (2000). Liuhua 11-1 field, South China Sea: A shallow carbonate reservoir developed using ultrahigh-resolution 3-D seismic, inversion, and attribute-based reservoir modelling. *The Leading Edge*, 19(8):834–844.

Talley, D. J., Davis, T. L., Benson, R. D., and Roche, S. L. (1998). Dynamic reservoir characterization of Vacuum Field. *The Leading Edge*, 17(10):1396–1402.

Thomsen, L. (1988). Weak elastic anisotropy. *Geophysics*, 51(10):1954–1966.

Trantanella, C. J., Dudley, D. G., and Nabulsi, K. A. (1995). Beyond the Born approximation in one-dimensional profile reconstruction. *Journal of the Optical Society of America A*, 12(7):1469–1478.

Tsvankin, I. and Grechka, V. (2000). Dip moveout of converted waves and parameter estimation in transversely isotropic media. *Geophysical Prospecting*, 48(2):257–292.

Tygel, M. and Ursin, B. (1997). Reciprocal volume and surface scattering integrals for anisotropic elastic media. *Wave Motion*, 26:31–42.

Vinje, V., Iversen, E., and Gjøystdal, H. (1993). Traveltime and amplitude estimation using wave front construction. *Geophysics*, 58(8):1157–1166.

Virieux, J. (1984). SH-wave propagation in heterogeneous media: Velocity stress finite-difference method. *Geophysics*, 49(11):1933–1957.

Virieux, J. (1986). P-SV wave propagation in heterogeneous media: Velocity-stress finite-difference method. *Geophysics*, 51:889–901.

Waite, M. W. and Sigit, R. (1997). Seismic monitoring of the Duri steamflood: Application to reservoir management. *The Leading Edge*, 16(9).

Wang, Z. (1997). Feasibility of time-lapse seismic reservoir monitoring: The physical basis. *The Leading Edge*, 16(9):1327–1329.

Wang, Z. and Nur, A. (1991). Aspects of rockphysics in seismic reservoir surveillance. In Sheriff (1991b), pages 285–300.

Winterstein, D., Stefani, J., Johnson, S., and Julander, D. (1998). 9-C time-lapse VSP monitoring of steam injection at Cymric oil field. *The Leading Edge*, 17(4):527–536.

Winterstein, D. F. and Meadows, M. A. (1991a). Changes in shear-wave polarization azimuth with depth in Cymric and Railroad Gap oil fields. *Geophysics*, 56(9):1349–1364.

Winterstein, D. F. and Meadows, M. A. (1991b). Shear-wave polarisations and subsurface stress directions at Lost Hills Field. *Geophysics*, 56(9):1331–1348.

Wood, L. C. and Treitel, S. (1975). Seismic signal processing. *Proceedings of the IEEE*, 63(4):649–661.

Wu, R.-S. (1989). The perturbation method in elastic wave scattering. *Pure and Applied Geophysics*, 131(4):605–637.

Yilmaz, O. (1987). *Seismic Data Processing*. Society of Exploration Geophysicists, Tulsa, Oklahoma.

Dank

Die vorliegende Doktorarbeit war nur durch die Hilfe vieler Personen möglich, die mich bei meiner Arbeit am Geophysikalischen Institut der TU Karlsruhe und darüber hinaus tatkräftig unterstützt haben. **Kai-Uwe Vieth**, **Jürgen Mann**, **Prof. Dr. Enders Robinson**, **Thomas Hertweck**, **Sandra Schliedermann**, **Tobias Müller** und **Erik Saenger** haben bereitwillig Teile des Manuskripts gelesen und sehr viele wertvolle Verbesserungsvorschläge gemacht. Dafür bin ich ihnen sehr zu Dank verpflichtet.

Die Beiträge der folgenden Personen möchte ich besonders herausheben:

Professor Dr. Peter Hubral. Durch die Anstellung am Geophysikalischen Institut ermöglichte er mir den Einstieg in das interessante und sehr anwendungsnahe Gebiet der Explorationsseismik. Sein Führungsstil beinhaltet außergewöhnlich viele Gestaltungsmöglichkeiten, sowie die Gelegenheit, selbst Verantwortung für die eigenen Projekte zu übernehmen. Von seiner Erfahrung und seiner Förderung konnte ich in vielerlei Hinsicht sehr profitieren.

Professor Dr. Serge Shapiro. Ihm gilt mein besonderer Dank. Seine offene und freundliche Art, sein Ideenreichtum und sein breit gefächertes Interessensgebiet machen ihn zu einem idealen Betreuer. Auch lange Zeit nach seinem Abschied vom Geophysikalischen Institut hat er meine Arbeit immer konstruktiv begleitet. Trotz seines vollen Terminplans war er stets bereit, meine Ergebnisse kritisch und ausführlich zu diskutieren und schließlich das Korreferat zu übernehmen.

Kai-Uwe Vieth, **Erik Saenger und Tobias Müller** danke ich für die Zeit in unserem gemeinsamen Projekt im SFB 381. Wir waren ein gutes Team, das sich bei geophysikalischen, (computer-)technischen, administrativen, ... Fragen immer engagiert gegenseitig unterstützt hat und so die Abwesenheit eines erfahrenen Post-docs gut ausgleichen konnte. Auch ungeliebte Arbeiten und Fahrten zum Söllerhaus wurden immer gemeinsam zu einem guten Ende gebracht. **Kai-Uwe** danke ich, dass er es mehrere Jahre mit mir in unserem gemeinsamen Arbeitszimmer ausgehalten hat. Er hat alle meine Berichte und Veröffentlichungen bereitwillig und gewissenhaft Korrektur gelesen und unzählige, wertvolle Verbesserungsvorschläge gemacht. **Erik** danke ich für die Pflege unserer Arbeitsumgebung auf der Cray T3E, sowie für seine Unterstützung bei der Nutzung

der FD-Modellierung, die für mein Projekt unverzichtbar war. Durch unsere gemeinsame Vorbereitung auf die Promotion hat er den Abschluss dieser Doktorarbeit sicherlich um einige Wochen beschleunigt.

Dr. Hans-Jürgen Hoffmann (PGS Seres A.S.) danke ich für die gute Zusammenarbeit. Sein Unternehmen unterstützt meine Forschung seit 1998 im Rahmen des *„Overburden Project“*. Auf unseren Projekttreffen – insbesondere während meines zweiwöchigen Aufenthaltes in Oslo (1999) – hat Jürgen meine neuesten Entwicklungen stets konstruktiv diskutiert. Viele seiner Vorschläge habe ich bei meiner Implementation von BRM gerne aufgegriffen.

Jürgen Mann. Mit seiner technischen und fachlichen Kompetenz und seinem Detailwissen über so viele Dinge, die das Leben leichter, besser und billiger machen, hat mich Jürgen immer wieder verblüfft. Ich denke gerne an unsere gemeinsamen Reisen zur EAGE. Ihm und unseren abendlichen Fahrten mit dem Zug verdanke ich unzählige, neue Erkenntnisse über die Feinheiten von C++, PostScript, Perl, hochspekulativen Geldanlagen, des CRS-Stack, der deutschen Bahn, etc., ja sogar meinen derzeitigen Wohnort, Vaihingen an der Enz.

Sandra Schliedermann. Sandra danke ich für ihre Unterstützung während der gesamten Vorbereitungszeit für meine Doktorarbeit. Sie hatte immer Verständnis, wenn ich dienstlich auf Reisen war oder spät abends noch am Computer arbeitete. Insbesondere in der Endphase hat mir Sandra den Rücken freigehalten, so dass ich mich voll auf die Arbeit an meiner Dissertation konzentrieren konnte.

Claudia Payne. Sie ist die Seele unserer Arbeitsgruppe, die (offenbar als einzige) immer den Überblick über die praktischen Fragen des Institutsbetriebes behalten und unzählige Schlachten des Papierkrieges für uns geschlagen hat. Ich danke ihr für die gute Zusammenarbeit bei der Gestaltung und Pflege der WIT home page, sowie bei der Verwaltung der Finanzen des SFB 381.

Dr. Norbert Gold danke ich, dass er mich damals (auf Vorschlag von **Dieter Walther**, dem ich dafür auch herzlich danke) als seinen Nachfolger beim SFB 381 angeworben hat. Auf freundschaftliche Weise hat er mir den *absolut* besten Start in meiner neuen Umgebung verschafft. Mit seiner coolen und sicheren Art, mit seinen Aufgaben und seinen Projektpartnern umzugehen, ist er ein unerreichtes Vorbild für mich.

Heiko Priller, **Erik Ewig** und **Christoph Jäger**. Als Hiwis im SFB 381 haben sie uns viele zeitraubende Arbeiten abgenommen. Viele Illustrationen in dieser Arbeit hat **Erik Ewig** für mich erstellt und mir so in der heißen Phase viel Zeit gespart.

Petra Knopf, Peter Dausch und Thomas Nadolny. Ich danke ihnen, dass sie trotz des manchmal mangelhaften Service des Rechenzentrums für die Verfügbarkeit der Computersysteme des GPI gesorgt haben. Petra und Peter haben mich bei der Beschaffung vieler neuer Geräte gut beraten und unterstützt. Bei der Einführung von Linux hat uns Peter zu viel Unabhängigkeit und Flexibilität verholfen und uns so die Arbeit wesentlich erleichtert.

Lebenslauf

Persönliche Daten

Name:	Andreas Kirchner
Geburtsdatum:	25.12.1970
Geburtsort:	Heilbronn
Nationalität:	Deutsch

Schulausbildung

1977 – 1981	Grundschule Heilbronn-Biberach
1981 – 1990	Hohenstaufen-Gymnasium Bad Wimpfen
09.05.1990	Abitur

Hochschulausbildung

1991 – 1997	Studium der Physik an der Universität Karlsruhe.
25.06.1997	Diplom
seit 1997	Doktorand an der Fakultät für Physik der Universität Karlsruhe.